OBSERVATIONAL ANALYSIS AND NUMERICAL SIMULATION OF METEOROLOGICAL PHENOMENA LEADING TO SEVERE RADIOLOGICAL IMPACT

By

RAKESH P. T.

PHYS 02 2014 04 011

Indira Gandhi Centre for Atomic Research, Kalpakkam, India.

A thesis submitted to the

Board of Studies in Physical Sciences

In partial fulfillment of requirements

For the Degree of

DOCTOR OF PHILOSOPHY

of

HOMI BHABHA NATIONAL INSTITUTE

August 2020

Homi Bhabha National Institute

Recommendations of the Viva Voce Board

As members of the Viva Voce Committee, we certify that we have read the dissertation prepared by **Rakesh P. T.** entitled **"Observational analysis and numerical simulation of meteorological phenomena leading to severe radiological impact"** and recommend that it may be accepted as fulfilling the thesis requirement for the award of Degree of Doctor of Philosophy.

For Dean, PS _____ Date: 15/03/2021

(Chairman- Dr. R. Baskaran

_____ Date: 15-3-2021

(Guide/Convener- Dr. R. Venkatesan

_____ Date: 2021/03/17

External Examiner - Dr. Thierry Hedde, CEA, France

_____ Date: 10/3/2021

Member 1: Dr. K. Devan

_____ Date: 15/03/2021

Member 2: Dr. M. T. Jose

_____ Date: 15-03-2021

Member 3: Dr. D. K. Mohapatra

Final approval and acceptance of this thesis is contingent upon the candidate's submission of the final copies of the thesis to HBNI.

I hereby certify that, I have read this thesis prepared under my direction and recommend that it may be accepted as fulfilling the thesis requirement

Date: 15-3-2021

Place: Kalpakkam

(Guide)

Homi Bhabha National Institute

Recommendations of the Viva Voce Board

As members of the Viva Voce Committee, we certify that we have read the dissertation prepared by **Rakesh P. T.** entitled **"Observational analysis and numerical simulation of meteorological phenomena leading to severe radiological impact"** and recommend that it may be accepted as fulfilling the thesis requirement for the award of Degree of Doctor of Philosophy.

For R. Raj Dean, PS ______ Date: 15/03/2021

(Chairman- Dr. R. Baskaran

______ Date: 15-3-2021

(Guide/Convener- Dr. R. Venkatesan

______ Date: 2021/03/17

External Examiner - Dr. Thierry Hedde, CEA, France

______ Date: 10/3/2021

Member 1: Dr. K. Devan

______ Date: 15/03/2021

Member 2: Dr. M. T. Jose

______ Date: 15-03-2021

Member 3: Dr. D. K. Mohapatra

Final approval and acceptance of this thesis is contingent upon the candidate's submission of the final copies of the thesis to HBNI.

I hereby certify that, I have read this thesis prepared under my direction and recommend that it may be accepted as fulfilling the thesis requirement

Date: 15-3-2021

Place: Kalpakkam

(Guide)

DECLARATION

I, hereby declare that the investigation presented in the thesis has been carried out by me. The work is original and has not been submitted earlier as a whole or in part for a degree / diploma at this or any other Institution / University

Rakesh P. T.

STATEMENT BY AUTHOR

This dissertation has been submitted in partial fulfillment of requirements for an advanced degree at Homi Bhabha National Institute (HBNI) and is deposited in the Library to be made available to borrowers under rules of the HBNI.

Brief quotations from this dissertation are allowable without special permission, provided that accurate acknowledgment of source is made. Requests for permission for extended quotation from or reproduction of this manuscript in whole or in part may be granted by the Competent Authority of HBNI when in his or her judgment the proposed use of the material is in the interests of scholarship. In all other instances, however, permission must be obtained from the author.

Date: 15/3/21

Place: KALPAKKAM

Rakesh P. T.

List of Publications arising from the thesis

Journal

1. "Observation and numerical simulation of submesoscale motions within sea breeze over a tropical coastal site: A case study", Rakesh P. T., Sandeepan, B. S., Venkatesan, R., Baskaran, R., *Atmospheric research,* **2017**, *Vol 198,* 205-215.

2. "Performance evaluation of modified Gaussian and Lagrangian Models under low wind speed: A case study", Rakesh P. T., Venkatesan, R., Srinivas, C. V., Baskaran, R., Venkatraman, B., *Annals of Nuclear Energy,* **2019**, *Vol 133,* 562-567.

3. "Formulation of turbulence diffusion relationships under stable atmospheric conditions and its effect on pollution dispersion", Rakesh P. T., Venkatesan, R., Roubin, P., Srinivas, C. V., Baskaran, R., Venkatraman, B., *Meteorology and Atmospheric Physics,* **2020**, 1-16.

Conferences

1. "Dispersion under low wind speed conditions using Gaussian Plume approach", Rakesh P. T., CV Srinivas, R Baskaran, R Venkatesan, B Venkatraman, *Indian Association for Radiation Protection*, **2018**, *Vol 49 (14)*, pp 31.

2. "Dispersion under meandering wind condition using a coupled particle trajectory model", Rakesh P. T., CV Srinivas, R Baskaran, R Venkatesan, B Venkatraman, *Indian Association for Radiation Protection*, **2018**, *Vol 49 (14)*, pp 32.

3. "Development of a Lagrangian Particle dispersion model for short term dose assessment", Rakesh P. T., CV Srinivas, R Baskaran, R Venkatesan, B Venkatraman, *National Symposium on Radiation Physics*, **2019.**

Rakesh P. T.

TO MY WIFE

Acknowledgments

I want to thank people who have played their part in shaping this thesis. Firstly, I would like to express my gratitude to my thesis advisor Dr. R Venkatesan, for the support, for his patience, motivation, and healthy debates. His guidance helped me in all the time of research and writing of this thesis. I want to thank my doctoral committee members Dr. R Baskaran, Chairman, Dr. K. Devan, Dr. M. T. Jose, and Dr. D. K Mohapatra for their insightful comments and encouragement.

I want to extend my gratitude to Dr. C. V. Srinivas for helpful discussions. I thank Mr. V. Gopalakrishnan for providing the dose rate data uninterruptedly, which helped me validate the model. I also thank Mr. A. Bhagavath Singh for providing meteorological data support without which the study would have been impossible. I also thank officers of MAPS for giving the release data, which supported a few of my studies constituting the thesis.

Special thanks to Dr. B. Venkatraman, Director, SQRMG, and Dr. R. Rajaraman for their support and encouragement.

I thank Mr. Arun Aravind with whom I had a fruitful discussion on my research topic and Mr. Ajay Rawat, with whom I had discussions on various topics in natural science, which helped in many areas of my research. I also thank my friends, Mr. Anuraj, Mr. Sreejith Sasidharan, Mr. Nakul, Mr. Amit Kumar, Smt. Sujatha for motivating me to pursue my research and Mr. Parthasarathy for accompanying me to the site whenever required for data collection and sensor replacement. I am grateful to Mr. Shanu Karmakar for scrutinizing the thesis for typos.

I gratefully acknowledge the Department of Atomic Energy of India and Homi Bhabha National Institute for providing the opportunity to do this study.

It will not be complete without asserting the role of my wife, Smt. Soorya, whose love, support, and encouragement made me overcome all the worst situations with ease and made this dissertation possible.

Contents

Page

List of Figures

List of Tables

Chapter 1

Introduction

This Chapter gives a brief overview of atmospheric dispersion, different methods of estimating turbulent diffusivity, and different diffusion schemes used in models for an accurate estimate of dispersion. The Chapter further elucidates the phenomena that may lead to severe radiological impacts such as submesoscale motions, stable conditions, low wind/calm episodes. Finally, the chapter concludes with the objective of the thesis.

1.1 Brief overview of dispersion

Kalpakkam is a coastal area and houses many nuclear facilities ranging from natural uranium-based Pressurized Heavy Water Reactor (PHWR) to Fast Breeder Reactor (FBR) and research laboratories and plants. To handle any nuclear or radiological emergencies, Indira Gandhi Center for Atomic Research (IGCAR) has developed an Online Nuclear Emergency Response System (ONERS) as a decision support system to assist Kalpakkam emergency management. ONERS uses weather models such as Weather Research Forecast (WRF) coupled with a Lagrangian Particle Disperion Model (LPDM) for radiological forecasts. Generally, Nuclear power plants are sited, designed, constructed, commissioned, and operated as per stringent regulations to ensure the health and safety of the plant personnel and the public. The releases from operating power plants are regulated so that the public should not get any radiological dose more than the stipulated limit by the regulatory body in any year. These calculations are performed using atmospheric dispersion models. Before proceeding to the modeling, let us briefly describe the atmospheric dispersion. Atmospheric dispersion is a combined effect of advection plus molecular and turbulence diffusion. Since the molecular diffusivity of air is too small on the order of 10^{-6} the contribution of molecular diffusion to dispersion can be neglected compared to turbulent diffusion.

The crucial inputs to any dispersion model are wind speed, wind direction, atmospheric stability, and turbulence parameters. Atmospheric stability is defined as the fate of a parcel of air displaced adiabatically in the vertical direction. Based on this, the atmospheric stability is broadly classified as unstable, stable, and neutral conditions. Under unstable conditions, the air parcel is warmer and less dense than the surrounding air leading to vertical movement of the parcel. In neutral conditions, the air parcel under consideration has the same temperature as that of the surrounding air. In stable conditions, the air parcel under consideration is cooler than its surroundings, leading to the downward movement of the parcel. In all these definitions, the reference lapse rate is the adiabatic lapse rate that is $0.98^0 C/100$ m [1]. There are many methods to estimate atmospheric stability. First of this kind is the method proposed by Pasquill [2] and modified by Turner [3]. Pasquill defines six stability classes based on the wind speed, cloudiness, and day and night differences. The classifications of stability are summarized in Table 1.1.

Table 1.1 – The Pasquill classes of stability

	Day			Night	
	Incoming solar radiation			Thinly overcast	
Wind speed at 10 (m)	Strong	Moderate	Light	>4/8 cloud	<3/8 cloud
<2	A	A-B	B	E	F
2-3	A-B	B	C	D	E
3-5	B	B-C	C	D	D
>6	C	D	D	D	D

Other methods include the temperature gradient method, which is applicable in smooth and open terrain [4], the method based on wind direction standard deviation [5], critical Richardson number method [6] and bulk Richardson number method [7]. The stability classification based on different methods is shown in Table 1.2.

Table 1.2 – The stability classification based on different methods [8]

Stability classification	Pasquill categories	σ_θ method	ΔT, temperature change with height ($^oC/100m$)	R_i Gradient Richardson number at 2 m
Extremely unstable	A	25	<-1.9	-0.9
Moderately unstable	B	20	-1.9 to -1.7	-0.5
Slightly unstable	C	15	-1.7 to -1.5	-0.15
Neutral	D	10	-1.5 to -0.5	0
Slightly stable	E	5	-0.5 to 1.5	0.4
Moderately stable	F	2.5	1.5 to 4	0.8
Extremely stable	G	1.7	>4	0.8

The critical Richardson number (Ri) is given by

$$Ri = \left(\frac{g}{\theta}\right) \frac{\left(\frac{d\theta_v}{dz}\right)}{\left(\frac{dU}{dz}\right)^2} \tag{1.1}$$

Similarly, the bulk Richardson number (Ri_B) is given by

$$Ri_B = \left(\frac{g}{T_v}\right) \frac{\triangle\theta_v \triangle z}{\triangle U^2 + \triangle V^2} \tag{1.2}$$

θ_v is the virtual potential temperature, θ is the potential temperature, g is the acceleration due to gravity, U is the mean wind speed, T_v is the virtual temperature, $\triangle U$ and $\triangle V$ are the difference in the along wind and crosswind components between heights separated by $\triangle z$ respectively.

The next step after the determination of stability is to compute the turbulence diffusivity. There are many methods available in the literature to determine the turbulence diffusivity. These methods are briefly described below.

1.2 Methods to estimate the turbulent diffusivity

1.2.1 From experiment

These experiments are conducted to determine the horizontal and vertical standard deviation of a plume as an input to Gaussian type models for dispersion. For a continuous point source of strength Q at the height of h from the ground, the Gaussian plume equation is written for concentration C, assuming a constant wind speed u, is

$$C(x,y,z) = \frac{Q}{2\pi u\sigma_y\sigma_z} exp\left(\frac{-y^2}{2\sigma_y^2}\right)\left[exp - \frac{(z-h)^2}{2\sigma_z^2} + exp - \frac{(z+h)^2}{2\sigma_z^2}\right] \tag{1.3}$$

The parameters σ_y and σ_z are the standard deviations of the distribution C in y and z directions, respectively. The main problem in using the Gaussian plume formula is the specification of standard deviations σ_y and σ_z. The estimation of these standard deviations is mainly from diffusion experiments conducted during the 1950s and 1960s [1]. The most important and highly cited of these experiments is the Project Prairie Grass. These experiments are conducted over a plain terrain at ground level within a downwind distance of 1 km. The Pasquill curves [2] modified by Gifford [9] are an outcome of this experiment. The curve for σ_y and σ_z derived by Pasquill is shown below in Fig. 1.1.

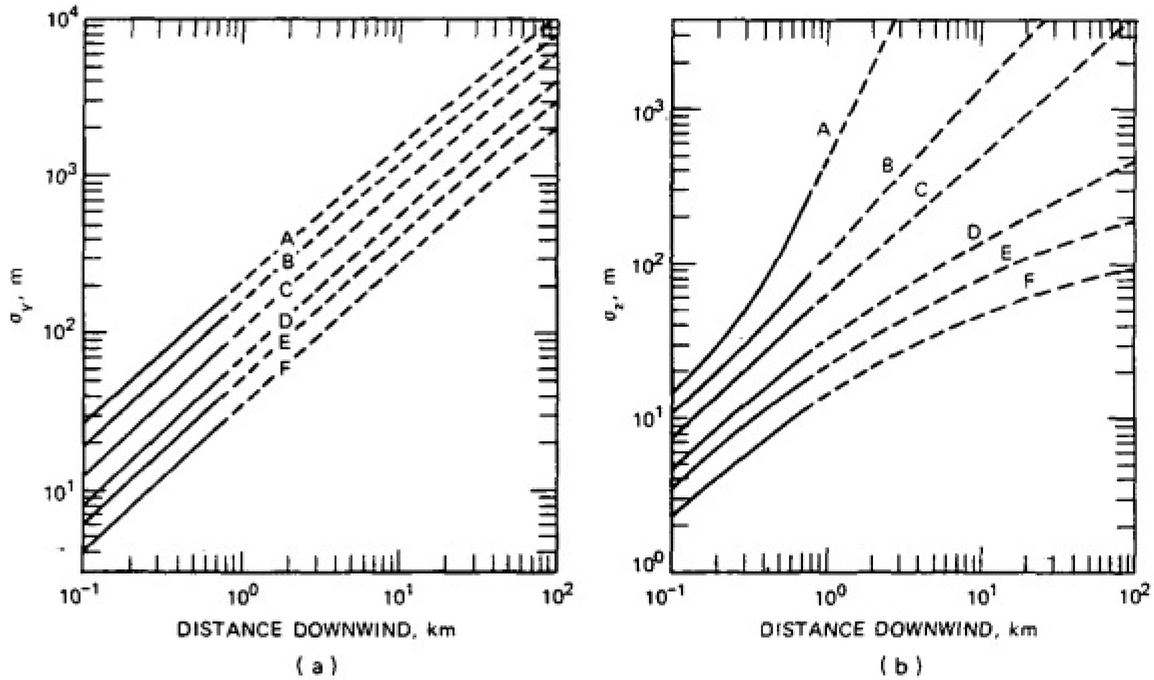

Figure 1.1 – Pasquill curves for σ_y and σ_z. The dotted lines show extrapolation from experiment data

Many authors attempted to derive the formula for the estimation of σ_y and σ_z. Smith [10] suggested power-law formula for the estimation of standard deviations and is given by

$$\sigma_y = ax^b \tag{1.4}$$

$$\sigma_z = cx^d \tag{1.5}$$

x is the downwind distance in meters, and a, b, c and d are empirical parameters. Many authors proposed the values for these empirical constants based on experiments [10, 11]. These coefficients are site-specific. Another method to estimate turbulent diffusion is based on the statistical method and is described in the next section.

1.2.2 Statistical method

This method is based on the principle that diffusion is random, and the trajectory of each particle can be represented by a statistical function. In general, diffusive motions have no memory, and particles will follow "Drunkard‘s path" or "Monte Carlo path." However, these memory-less random walks do not apply to atmospheric motions. In the atmosphere, for example, the turbulence wind velocity component $v'(t)$ is having a non-zero correlation with $v'(t+\Delta t)$. The auto-correlation function is written as

$$R(\triangle t) = \frac{\overline{v'(t)v'(t+\triangle t)}}{\sigma_v^2} \tag{1.6}$$

The overbar indicates the time average and σ_v is the standard deviation of the crosswind component of the wind velocity. When $\triangle t \to 0$, $R(\triangle t) \to 1$ and $\triangle t \to \infty$, $R(\triangle t) \to 0$

Based on Taylor's theorem, the crosswind variance is given by the formula

$$\sigma_y^2 = 2\sigma_v^2 \int_0^t \int_0^{t'} R(t')dt'dt \tag{1.7}$$

As $\triangle t \to 0$, $R(\triangle t) \to 1$

then

$$\sigma_y^2 \approx \sigma_v^2 t^2 \tag{1.8}$$

or $\sigma_y \ \alpha \ t$

As $t \to \infty$, $\int_0^{t'} R(t')dt' = T$

T is called the time scale.

Then

$$\sigma_y^2 \approx 2\sigma_v^2 T t \tag{1.9}$$

or $\sigma_y \ \alpha \ t^{1/2}$

The Eqn. 1.9 imply that as the travel time increases, the rate of diffusion decreases. At initial times the motions are linear since the particles remember its initial velocity. As the travel time increases, the particles will not remember its initial velocity, leading to the Monte Carlo path. If the auto-correlation function is exponential, then the variance using Eqn. 1.7 is given by

$$\sigma_y^2 = 2\sigma_v^2 T^2 \left[\frac{t}{T} - 1 + exp\left(-\frac{t}{T}\right)\right] \tag{1.10}$$

The standard deviation of the wind velocity components can be computed by the similarity method [1] or by σ_θ method [12]. The time scale T can also be estimated by Hanna's method [1]. The third widely used method to estimate turbulent diffusion by advanced dispersion models is the similarity method outlined in the next section.

1.2.3 Similarity method

This method is based on the assumption that the behavior of the atmosphere is similar if parameters such as Z/L are held constant. Here L is the Obukhov length, and Z is the height from the ground. The functional forms for turbulence diffusivity are then written in terms of this stability parameter and other scaling variables such as friction velocity u_*, convective velocity w_*. The details of similarity relations and benefits of using it are discussed in great detail in subsequent chapters. The majority of the dispersion models employ any of the above methods for dispersion computations. For a homogeneous and stationary atmosphere that exists in a short range of a few km in space and for a few tens of minutes in time, a simple Gaussian Plume Model (GPM) is used. On the other hand, the non-homogeneous spatio-temporal variation of the atmospheric flow and dispersion is resolved by numerical models. There are many numerical models available for computing dispersion. One is based on the Eulerian method, and the second method is based on the Lagrangian approach. A brief review of these models is given in the next section.

1.3 Models for dispersion

There are many dispersion models, from simple box models to complex models like Lagrangian particle dispersion models. A brief description of these models is given below.

1.3.1 Box models

Box models are based on conservation of mass. The domain of interest is considered as a box and pollutants emitted into it may undergo physio-chemical processes. The box models require very simplified inputs, and it is easy to use. One advantage of the box model is that it can treat physical and chemical processes that pollutants will undergo. The disadvantage of the box model is that it does not account for the local concentration of the pollutants [13], and therefore it is not suitable for sites where particle dynamics are highly influenced by local changes in the wind field and emissions. One example of the box model is AURORA (VITO, Belgium), a generally used model to treat the inert and reactive gases in the urban environment [13, 14]. Another example of the box-type model is Canyon Plume Box (CPB) (GEOMET) used for urban canyons with height to width ratios between 0.5 and 2 [13].

1.3.2 Gaussian Model

Gaussian model is based on Gaussian plume equation. The Gaussian equation is a solution to Fick's law of diffusion with constant eddy diffusivity K and wind speed, u. The advantage of the model is its relative easiness in computation, simple inputs and well tested for homogeneous terrains for a short range of time and space so that stationarity of wind and turbulence is ensured. One such model based on the Gaussian formulation is The AERO-POLlution model (AEROPOL) (developed in Tartu Observatory, Estonia), a steady-state dispersion model used for the dispersion of inert gases and particles up to a distance of

100 km from the source. This model has modules to treat the influence of buildings and plume rise based on Briggs formula [15], but it is only applicable to flat terrain. The model calculates wet deposition as a function of rainfall rate and dry deposition using the deposition velocity approach. Atmospheric stability is computed based on the Pasquill stability classes, and it is mainly suitable for dispersion under near-neutral conditions and long term averages. Another advanced model is UK Atmospheric Dispersion Modelling System (UK-ADMS), which has modules for different locations like complex terrain, coastal areas, and urban environments, and it can compute wet deposition and radioactive doses [16]. Another widely used model is American Meteorological Society/Environmental Protection Agency Regulatory Model (AERMOD) [17], which again based on the Gaussian plume approach. This model employs similarity laws for predicting the vertical profiles of wind speed, wind direction, and turbulence using single-level measurements of wind speed, wind direction, and temperature [13]. The model is used in plain as well as in complex terrain. In this model, the horizontal and vertical dispersion is assumed Gaussian during stable conditions, and under unstable conditions, a bi-Gaussian probability density function is applied for vertical distribution. Though it is designed for particle dispersion, the model is used mainly for gas dispersion [13]. The model does not have modules for dry and wet deposition of gases, but it treats dry deposition of particles using a simple reflection algorithm. Similarly, there are other Gaussian type models like California Department of Transportation (CALINE3) for highway pollution, Offshore and Coastal Dispersion (OCD) for coastal sites [18], Buoyant Line and Point source (BLP) [19], and Industrial Source Complex (ISC) for industrial sites and Areal Locations of Hazardous Atmospheres (ALOHA) for accidental and heavy gas dispersion [16].

1.3.3 Gaussian puff model

Puff models show similarities between Gaussian and Lagrangian models. Unlike Gaussian plume models, the Gaussian puff model can take time-varying meteorology (wind speed and direction), and therefore it is superior to plume models. It treats pollution as a superposition of several puffs. There are many puff models with applications spanning risk management to environmental protection [20, 21]. A few examples include the Second-order Closure Integrated PUFF (SCIPUFF) model [22], RIsø-Mesoscale-PUFF (RIMPUFF) model [23] which is a part of the Real-time Online Decision Support (RODOS) system [24], Random Puff Transport and Diffusion (RAPTAD) puff model for dispersion over complex terrain [25] with both urban and industrial applications [26, 27]. Another model called CALifornia PUFF (CALPUFF) is an unsteady puff dispersion model [28] for gases and particulates by taking into account of time-varying meteorology based on similarity relations. It can take into account various sources such as point, volume, and area sources with plume rise, stack effects, and building effects using Schulman-Scire [29] or Huber-Snyder methods. The model calculates the dry deposition using resistance methods and wet deposition using the rainfall rate and type. It has been used in multiple studies [30–32]. The disadvantage of the model is that it is not recommended for calculating dispersion for time scales shorter than 1 hr or where dispersion is highly influenced by turbulence, such as in the urban environment [13].

1.3.4 Trajectory models

Trajectory modeling is another versatile method of addressing the non-homogeneity of the atmosphere and applicable to most realistic conditions. These models are built under the Lagrangian framework. It performs the stochastic simulation of a large number of computational particles, and each particle represents the fraction of the emitted pollutants. The trajectory of a particle is computed using the trajectory equation of the form

$$X(t+\triangle t) = X(t) + (\bar{U} + u')\triangle t \tag{1.11}$$

$X(t+\triangle t)$ is the particle position after a time $t+\triangle t$, $\bar{U}$ is the mean wind velocity, and u' is the fluctuating part of the wind velocity vector. The turbulence part of the wind velocity vector is computed using Langevin type stochastic differential equations. The two most popular LPDMs used in radioactive plume dispersion are Numerical Atmospheric-dispersion Modeling Environment (NAME) developed by the UK met office and Hybrid Single Particle Lagrangian Integrated Trajectory (HYSPLIT) [33] model, which is a hybrid particle-puff model which very well used to estimate the consequence of accidents and source identifications [34–36]. Another open-source code and highly sophisticated model is FLEXPART [37]. It can take meteorological inputs such as wind, temperature, boundary layer height, rainfall, etc. from a weather model like the WRF model. This model is well validated and it is used in lot of environmental applications [38–40]. The model can be used to assess the dispersion in short range as well as in long range. A few problems taken up for this thesis uses the FLEXPART model in conjunction with WRF.

Thus, there are many numerical models available as open-source or commercial codes that can be directly used for radiological impact assessment of a nuclear power plant emissions. These models also are capable of describing the complexities associated with the terrain, such as hilly topography, coastal heterogeneity, urban complexity, etc. which are already mentioned. In coastal areas due to land-sea breeze circulations, the Thermal Internal Boundary Layer (TIBL) develops, and it leads to fumigation. It is reported by Venkatesan et al. [41] that fumigation may lead to an increase in the dose values by a factor of two at downwind distances of 4 km to 10 km. They have used the modified Gaussian model [42] for the estimation of ground-level concentrations. In complex hilly terrain, diagnostic models like System for Prediction of Environmental Emergency Dose Information (SPEEDI) [43], NUATMOS, etc. are used for quick assessment of the dispersion and the radiological dose. To summarize, based on the above methods, there are different dispersion models that covers the micro, meso, and large scale ranges of the atmosphere. The currently available weather models are capable of simulating the different scales of motion in the atmosphere. However, certain atmospheric phenomena of site-specific nature call for special attention and specific treatment in turbulent dispersion models or in weather models, rare in literature. The time and space scale of a few of these phenomena fall in between the microscale and mesoscale range. These motions are called the sub-mesoscale motions. The subsequent section describes those phenomena that are crucial in dispersion calculations.

1.4 Site-specific phenomena effecting dispersion

One important phenomenon which is often observed in coastal terrains is called Horizontal Convective Rolls (HCRs) that have an impact on the dispersion of the pollutant [44]. Therefore, theory or parameterization describing the phenomenon of HCR has to be accounted for in the dispersion model or in a weather model that provides inputs to these dispersion models for the realistic estimation of dispersion. A few other phenomena that prevail in coastal and mountainous terrains are calm wind conditions, low wind speed meandering, and dispersion under highly stable conditions.

1.4.1 Horizontal convective rolls (HCRs)

HCRs are counter-rotating vortex rolls which are nearly aligned with mean wind direction in the convective boundary layer (Fig. 1.2).

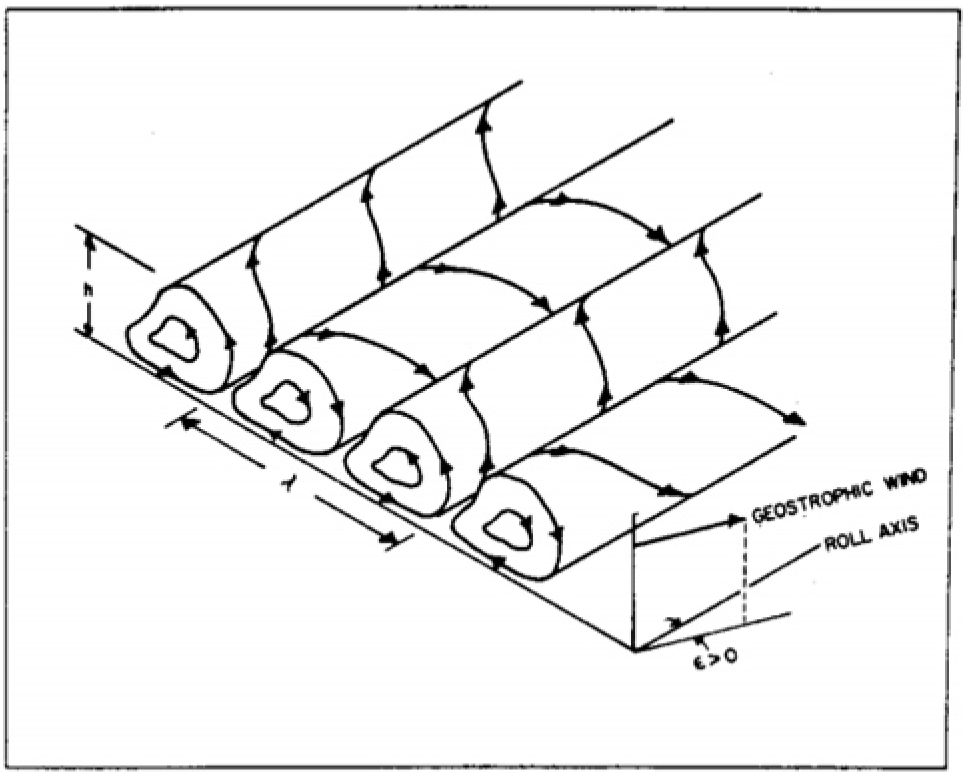

Figure 1.2 – Pictorial representation of coherent roll structures [45]

These structures are often seen in satellite images [46], but their development is poorly understood due to a lack of intense observations. These structures or eddies are responsible for vertical transport of humidity, heat, momentum, and pollutants within the atmospheric boundary layer [44, 47]. Many researchers described the occurrence of these structures theoretically [48, 49], by laboratory experiments [50] and simulated with numerical models. Many authors reported that these structures are formed under moderate heat flux and minimum wind speed, or vertical wind shear [45, 51–53]. Other studies have shown that the presence of these structures effects the surface flux, boundary layer height, and flow characteristics [54]. Understanding these phenomena is riddled with problems because of the presence of other structures having similar behavior. Sandeepan et al. [44] simulated the HCRs which are present before sea breeze hours at a coastal site, Kalpakkam, and showed its effect on pollutant dispersion. The observed convective rolls over Kalpakkam is shown in Fig. 1.3.

Figure 1.3 – MODIS image of convective rolls observed over Kalpakkam on 24th September 2010 [44]

These structures have a vertical scale equal to mixed layer depth [55] and a wide range of horizontal scales [52]. Gravity waves generated from above or below the mixed layer can generate these types of structures and are reported by Balaji and Clark [56]. In the sheared boundary layer at the near-surface, these structures take the form of elongated structures as evident in observations and numerical simulations [55, 57]. These streaks are mostly confined within the surface layer but can extend to the top of the boundary layer [58]. These structures are mostly found under neutral and near-neutral conditions, and it forms when there is sufficient shear present to organize the buoyant thermals rising from the surface. It is reported [59, 60] that near the surface, the shear contributes more to turbulence kinetic energy compared to buoyancy. They also reported that these streaks tend to take similar forms even under conditions where buoyancy dominates over the shearing stress. The period or the time scale of such motions is ≈ 30 min. These structures have a wide range of aspects ratios (wavelength of the convective rolls divided by boundary layer depth). Generally, the aspect ratio of these structures varies from 1.8 to 12.1 [55] with an average aspect ratio of 3.15 ± 0.7 (mean ± standard deviation). The observed value is in close agreement with the predicted value of 2.83 by linear theory [49] within statistical confidence of 99 %. Weckwerth et al. [45] explained 74% of the scatter in the aspect ratio observations of convective rolls over the land area with a linear relationship to Z_i/L, where Z_i is the boundary layer height. These structures, which have an important role in pollutant dispersion, will affect the radiological dose derived from the concentration simulated by dispersion models. The presence of these motions within the sea breeze layer is rarely studied so far because the absence of the cloud during sea breeze hours prevents it from appearing in the satellite and the radar images or due to the insignificance of these motions on the weather. The simulation of these structures within the sea breeze and its impact on dispersion is one of the important problems addressed in this thesis. The simulation of these structures and their effect on radiological doses are discussed in Chapter 2. The highly stable state of the atmosphere is another condition that has a vital role in the dispersion. The issues that need to be dealt with under highly stable conditions is discussed in the following section.

1.4.2 Dispersion under highly stable conditions

Despite much attention over the last several decades, dispersion under highly stable conditions is riddled with problems. This is because under highly stable conditions, the stability and turbulence relationship based on Monin-Obukhov Similarity Theory (MOST) does not represent the turbulence and stability functions realistically due to its sensitivity to the frequently observed phenomena like the gravity waves, meandering motions, radiative divergence, intermittency, etc. [61, 62]. For example, it has been reported that [63] lateral dispersion is enhanced under meandering conditions in comparison to lateral dispersion estimated by turbulence mixing alone. The effect of meandering is pictorially represented in Fig. 1.4. The standard Gaussian plume model with Pasquill dispersion parameters is not sufficient under these circumstances. Vickers and Mahrt [64] found that the timescale of these motions is above the turbulence scale but less than mesoscale and called as submesoscale motions.

These motions originate because of several physical mechanisms and may have originated elsewhere and propagated to the measurement locations. Except for a few well-defined cases, the physical mechanisms responsible for these motions are not very well known or predictable [65]. Etling [66] reported a few causes of meandering motions as gravity waves, horizontal vortices, etc. The meandering motions are defined as either gradual or sudden drift in the wind direction [67]. These meandering motions may result in the multimodal frequency distribution of wind directions. The effect of these motions on plume dispersion and an observation comparison with the Hanford tracer experiment is reported by Sandeepan et al. [68] using a LPDM coupled with a weather model. These motions are predominant under stable to highly stable atmospheric conditions.

Figure 1.4 – Small scale meandering motions associated with wave-like oscillations (source: https://submeso.org/meandering-motions/)

Though MOST is not applicable under these conditions, the local scaling introduced by Nieuwstadt [69] using Cabauw data, showed the existence of z-less stratification and properties of turbulence under highly stable conditions as envisaged by MOST. The hypothesis implies that the dimensionless combinations of variables such as gradients, fluxes, etc. measured at the same height can be expressed as universal functions of the stability parameter (z/λ), where λ is the local Obukhov length. Smedman [70] used data from the Marsta site in Sweden and showed the universality in the scaled turbulence using measurements from two different heights. Dias et al. [71] showed that, apart from second-order moments, third-order moments also followed the z-less stratification under highly stable conditions. Sorbjan [72] developed local similarity functions based on dimensional analysis and similarity approach. Each of these methods has merit over MOST when applied to a stably stratified boundary layer but fails when the surface layer became strongly stable. Sorbjan [73] further explored alternative forms of similarity scales and examined the resulting similarity laws in the stably stratified boundary layer. In contrast to the 'flux-based' MOST approach, the 'gradient-based' similarity relations worked well when the stable atmospheric layer was divided into four regimes using the Richardson number. It was observed that the generality of any scaling laws under extremely stable conditions was problematic. In the case of stable conditions, many studies [69, 74, 75] have shown that the increase in the values of the stability functions with respect to stability parameter is less than that predicted by the Businger-Dyer formula [76, 77] especially for $Z/L > 1$. The deviation is due to sampling problems at high stability conditions and intermittency and non-turbulent motions occurring during highly stable conditions [78].

Apart from atmospheric boundary layer models, another vast area of application of similarity relationships, as mentioned at the beginning of this Chapter, is in air pollution dispersion models. In air pollution models the turbulent statistics of the wind components are used in the simulation of pollutant trajectories [79, 80]. Functional relationships of turbulent intensities based on MOST are widely used in dispersion models to parameterize the diffusion. A few studies are available in the literature that addresses the behavior of normalized standard deviations of wind velocity fluctuations, especially horizontal components under highly stable conditions. Mahrt [81] reported that under highly stable conditions, the decoupling of turbulence at higher levels with that at the surface and meandering motions led to the breakdown of the similarity theory. Pahlow et al. [82], based on the MOST, showed that except normalized standard deviations of temperature, normalized standard deviations of wind velocity fluctuations did not follow the similarity theory and the concept of z-less stratification under highly stable conditions. Many researchers [73, 81, 83] pointed out that self-correlation played a crucial role in highly stable conditions in predicting the success of similarity theory. Given the issues described above, the thesis discusses the application of MOST for the stable atmospheric condition under local framework. New turbulence intensity relationships are proposed for stable conditions and tested for pollutant dispersion and are discussed in great detail in Chapter 3.

1.4.3 Calm conditions/low wind speeds

Calm conditions and low wind speed have very profound effects on the pollutant concentration Dilution Factors (DFs) [84]. The calm can be defined as the state in which the wind speed is less than the threshold of the measuring instrument. However, in atmospheric dispersion modeling, the calm condition is defined as the wind speed below 0.5 m/s [85]. Similarly, Low Wind Speed (LWS) means any speed lower than 2 m/s. Pasquill [86] recognized that for $u < 2$ m/s the plume is unlikely to have any definable travel [87, 88]. Wilson et al. [89] considered the limiting wind speed as 2 m/s for his experiments under low wind speed conditions. Low wind speed occurs at many sites, and have a greater impact on pollution episodes. Under low wind speed, Pasquill [2] reported that diffusion is highly irregular and indefinite. Later, many diffusion experiments conducted at low wind speed supported Pasquill‘s conclusion and found that the standard deviation of the plume dispersion corresponds to any atmospheric stability. Etling [66] reported that under low wind speed at night times, the plume can meander in wider angles and will results in multi peaks in concentration. Moreover, it is reported from experiments and theoretical predictions that under the meandering conditions, the average concentration of the pollutants is less by factor 2-6 compared to straight plume situation [90, 91].

In the Gaussian plume models, the pollutant concentration tends to go exceptionally high under low wind speeds because the wind speed appears in the denominator of the equation for concentration. As the wind speed decreases, the complexity of the boundary layer increases, and therefore the dispersion study under weak wind conditions [92] is crucial. Conventionally, under moderate to strong winds, diffusion in the along wind direction is neglected compared to advection. However, under low wind speed, the scale of diffusion is comparable to advection. Arya [93] has shown that along wind diffusion is important under low wind speed less than 1.5 m/s. In the past, different modeling approaches have been adopted to deal with low and calm winds [94]. Many researchers have attempted modifications in terms of the dispersion parameters. Sagendorf and Dickson [95] used schemes like split-sigma and segmented plume approaches to deal with dispersion under nighttime low wind speed conditions. Zannetti [96] has introduced a concept of U_{min}, to artificially dilute the plume for computation of dispersion parameters in low winds. An inter-comparison study of different semi-empirical schemes with low wind speed diffusion data is reported by Cirillo and Poli [12].

In another study, Sharan et al. [97] proposed, "short-term averaging" approach in the absence of wind data. Demuth et al. [98] have proposed an analytical model for calm wind situations under finite mixing length. They have employed the model by Berlyand and Kurenbin [99] with diffusivity coefficients varying in space under unstable conditions and introduced a reflection at the top of the boundary layer. On the other hand, under stable conditions, they have used a model with constant diffusivity coefficients. Yokoyama et al. [100] expressed dispersion parameters as a linear function of time to compute concentration from a point source but requires persistence of calm conditions for a sufficiently long time. Yamamoto et al. [101] have simulated the crosswind concentration profiles under low and variable wind conditions by calculating the trajectories of the virtual particles emitted from a ground-level source. These trajectories are computed using observations of wind speed and direction obtained from the tower. They also developed a non-Gaussian model for low and variable wind conditions by assuming that the lateral concentration profiles are proportional to the angular distribution of the wind direction and inversely proportional to the product of wind speed and distance from the source. Similarly, Okamoto and Shiozawa [102] have proposed a trajectory plume model under calm and weak wind conditions. They assumed the diffusion rate as a linear function of time and used time integration of three-dimensional puff models. Various aspects of atmospheric diffusion in low winds have been reviewed by Yadav et al. [103]. Sharan et al. [94] developed Gaussian models that can treat calm episodes and the simulated concentrations are compared with field experiments. Mainly these modeling practices use Gaussian plume models, which do not account for heterogeneity and turbulence in space and time and use mainly the empirical relations for diffusion under low/calm wind speed. Recently, the LPDM received much attention compared to other Eulerian and Gaussian model since it can treat any wind conditions. Under low wind speed conditions, dispersion is mainly governed by meandering. Consequently, the more the wind speed decreases, the more the standard deviation of the wind direction increases, making it more difficult to define a mean plume direction. Even when the stability (stable conditions) reduces the vertical dispersion, and the instantaneous plume may be thin, meandering disperses the plume over a rather wide angular sector.

By analyzing tracer experiment data, Sagendorf and Dickson [95] and Wilson et al. [89] found that over flat terrain and under LWS conditions, horizontal diffusion was enhanced because of the meander. Thus, the resulting ground level concentration is generally lower than that predicted by standard Gaussian plume models. We recall, in particular, that in these models, stationary conditions are assumed. Thus concentrations approach infinity as the wind speed tends to zero. As a consequence, different types of models are necessary [104]. In particular, Oettl et al. [105] proposed a Lagrangian stochastic model in which the time step is chosen randomly from a uniform distribution. In their study, a negative auto-correlation parameter is used for the horizontal wind components. The negative correlation parameter is chosen based on the computed Eulerian Auto-correlation Function (EAF), from one year of sonic anemometer observations in Graz, Austria. They found that under meandering condition, the auto-correlation exhibits a negative lobe (Fig. 1.5) instead of the usual exponential.

The negative lobe in the auto-correlation function is also reported by many in the past

[91, 106–108]. For example, Hanna [91] reported from a study that the auto-correlation function of the longitudinal wind component experiencing a large negative lobe, reaching a minimum of -0.65 and a secondary maximum of 0.40. It is observed that the transverse correlation attains negative values for some spatial lag r (or time lag s). The negative lobe in auto-correlation function is possible under the condition that across a plane perpendicular to the y-direction, there should be no net mass flux. Therefore, a backflow is necessary somewhere in the plane to maintain a zero net mass flux [109]. Thus the negative lobe in the EAF of transverse wind component implies a backflow with eddies of wide ranges of sizes of r. When eddy sizes are very small, return flow takes place over a limited range of eddy size r, and as a consequence, large negative values for the transverse correlation appear [110]. Further, a few authors also have suggested the use of modified auto-correlation function in Lagrangian and Gaussian models to address the dispersion under low wind speed conditions [111–114]. They suggested that meandering under low wind speed leads to auto-correlation with a negative lobe, and hence the conventional exponential function for auto-correlation is not valid.

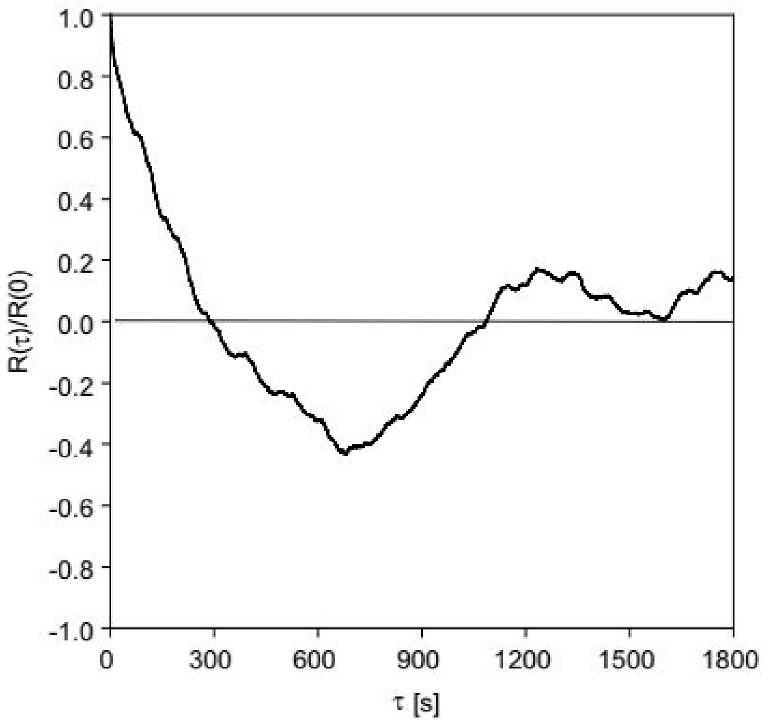

Figure 1.5 – The negative auto-correlation function reported by Anfossi et al. [87]

Carvalho et al. [88] used a semi-analytical Lagrangian particle model to study dispersion under low wind speed conditions by iterative solution of a stochastic integral equation. In their study, they used a modified auto-correlation function suggested by Frenkiel [106]. Anfossi et al., [115] proposed a 2D Langevin type equation in the Lagrangian model to address low wind speed dispersion and compared with experimental data. The method needs inputs of some hybrid parameters, meandering oscillation frequency, and time scale of fully developed turbulence. Stefanello et al. [116] developed an analytical Lagrangian model to treat dispersion under low wind speed using a modified auto-correlation function. Their comparison of simulated concentration with observation showed some promising results.

The thesis discusses the modeling approaches under low wind speeds using the modified Gaussian and Lagrangian model and comparing them with experimental data. Further, the thesis addresses the development of an LPDM, which can be used under calm and low wind speed conditions. Moreover, the effect of low/calm wind speed on dispersion and the resultant radiological dose will be discussed and is found in great detail in Chapter 4 and Chapter 5.

1.5 Importance of these phenomena in nuclear parlance

After the nuclear disasters at the Chernobyl and Fukushima, the importance of nuclear emergency preparedness gained momentum. Numerical modeling of atmospheric dispersion is a crucial tool for such programs to predict the radiological impact to the public. Most nuclear plants in the world are located either in complex hilly terrains or at coastal sites. As already mentioned, various meteorological phenomena occur at these sites like fumigation in coastal sites due to sea breeze circulation, channeling of the flow within the valley, the decoupling of the valley flows from the pressure gradient flow from the valley ridge and dividing streamlines due to obstacles by the hills, etc. Hence, the meteorological parameters such as wind speed, wind direction, temperature, and diffusion parameters undergo complex temporal and spatial changes. A few of these changes falls either in microscale or mesoscale range. To some extent, the methodologies to model these motions are already developed for plume dispersion. However, we have discussed certain conditions like HCR, highly stable conditions and the low/calm wind, which occur at many sites during transient meteorological conditions. As already mentioned, sophisticated models are required to simulate such motions. Study of these motions like convective rolls and dispersion under stable, low/calm wind speed conditions is required to compute the annual dose for a nuclear power plant under normal operation and dose due to accidental releases to have a realistic estimate of public dose. Apart from modeling, meteorological instrumentation plays a pivotal role in assessing and characterizing these motions. There are instruments such as tether balloons, radiosondes, Sonic Detection And Ranging (SODAR) for measuring vertical profiles of wind speed, wind direction and temperature and sonic anemometers for turbulence measurements which can operate in higher sampling frequency so that we can compute fluxes of heat and momentum which determines the dynamics of the atmosphere.

1.6 The objective of the thesis

The objective of the thesis is to analyze the effect of horizontal convective rolls, highly stable and low/calm wind speed conditions on dispersion of pollutants, especially the radioactive pollutants using meteorological observations and numerical modeling. The thesis addresses the following issues.

1. The simulation of HCRs within sea breeze layer using the well known weather model, WRF model and subsequent dispersion simulation of radionuclide with particle trajectory model, FLEXPART.

2. Derivation of turbulence diffusion relationships under stable conditions and incorporation in the FLEXPART model and comparison of simulated dose rate with measurements.

3. Simulation of dispersion under low wind speed meandering conditions using a modified Gaussian model and Lagrangian model with coupled Langevin equation and comparison with experiment.

4. Development of a LPDM and study of the effect of calm wind speed conditions on the radiological impact.

1.7 Thesis arrangement

In **Chapter 1**, an introduction of atmospheric dispersion and different models, methods of determining the stability of the atmosphere for estimation of dispersion are discussed. Further, a review of past research conducted on atmospheric phenomena affecting dispersion is briefed.

In **Chapter 2**, observational analysis and numerical simulation of HCRs within sea breeze layer over Kalpakkam are discussed with the conditions of occurrence of such motions. The data collected for a few sea breeze days in a year from SODAR observations are used in the study for statistically meaningful results. The time-height plot of turbulence kinetic energy estimated using SODAR data shows the presence of HCR with a period of $\approx$ 30 min. The observations are further supported by FFT and wavelet analysis of sonic anemometer data collected at 10 m above ground level. The simulation of HCRs using the high-resolution WRF model and the configuration of the model are discussed. Further, comparison of simulated turbulence kinetic energy with that estimated using SODAR observations are also described. Effect of such motions on the dispersion of radioactivity using a LPDM, FLEXPART, is also discussed.

In **Chapter 3**, long term data collected using sonic anemometers over complex terrain, Cadarache, France and coastal site, Kalpakkam is analyzed to derive turbulence relationships under stable atmospheric conditions. The data collected at both the sites are subjected to multi-resolution decomposition [117] to avoid the flux sampling errors arising out of short averaging time [118]. The Chapter elaborates on the need for multi-resolution decomposition for formulating turbulence diffusion relationships under stable conditions. Further, the theoretical study of dispersion after incorporating these turbulence relationships into the FLEXPART model is discussed using input from the WRF model over the Cadarache site. Moreover, modification of the FLEXPART model to use observational data from the meteorological tower is also discussed. The data of gamma dose collected over kalpakkam site measured using Autonomous Gamma Dose Loggers (AGDL) is compared with the simulated gamma dose rate using modified FLEXPART.

In **Chapter 4**, simulation of radiological dose under low wind speed meandering conditions using a modified Gaussian model and modified Langevin equation [115] is discussed. The modified dispersion parameters are computed using tower observations. Further, the behavior of auto-correlation function under low wind speed conditions is also analyzed. An observational comparison of simulated results with tracer experiment data collected from the Hanford nuclear site under low wind speed conditions is presented. The study shows that under low wind speed meandering conditions, pollutants are dispersed more in the horizontal direction and leads to a reduction in the peak centerline concentrations. Also, it is noted that the radioactivity spreads over a larger area under meandering conditions. The study is useful for regulatory calculations and the design of nuclear power plant stacks for normal releases.

In **Chapter 5**, a LPDM is developed for the computation of dispersion. The model is built in a Lagrangian framework. The model is used especially for short-range dispersion calculations. The Chapter discusses the development of the model, different methods of estimating diffusion velocities such as from sonic anemometer data, similarity theory, and from PG stability curves. Simulation of dispersion and resultant radiological impact under calm/intermittent calm is discussed. Data collected over a year at Kalpakkam using sonic anemometer under calm episodes is used for this purpose. The study shows that under calm conditions, dispersion parameters based on PG stability classes do not provide conservative estimates.

The conclusion of the study and future scope of the work in enunciated in **Chapter 6.**

The list of instruments used in the study constituting the thesis is given in Annexure-1

Chapter 2

Simulation of Horizontal rolls and its effect on dispersion

This Chapter gives an overview of HCRs, which are termed as submesoscale motions. The Chapter discusses the observational evidence of HCRs and the analysis using SODAR and sonic anemometer on the formation of HCRs during sea breeze hours, the conditions of existence of such phenomena, and the numerical simulation of these structures using the high-resolution WRF model[1]*. Further, the Chapter describes the effect of these motions on the dispersion of radioactivity.*

2.1 Studies on horizontal convective rolls

Due to horizontal heterogeneity, coastal sites experience mesoscale sea breeze wind circulations, vortices, and gravity waves. In the past, many researchers studied the structure of sea-land breeze and sea breeze fronts [119–122]. In the recent past, due to advancements in numerical modeling and observation techniques, the studies were focused on the turbulence structure at the interface between the land and sea breezes. For example, spectral

[1]*Rakesh, P.T., Sandeepan, B.S., Venkatesan, R. and Baskaran, R., 2017. Observation and numerical simulation of submesoscale motions within sea breeze over a tropical coastal site: A case study. Atmospheric Research, 198, pp.205-215.*

characteristics of the boundary layer and sea breeze fronts over Thumba on the western coast of South India, has been studied by Prakash et al. [123], [124]. During the passage of the sea breeze front, they have observed the existence of a six-minute wave. A few researchers in the past have also pointed out the existence of coherent structures within the sea breeze layer [119, 125, 126]. Based on the time and space scales of these structures, they are classified as submesoscale motions. Submesoscale motions are generally defined as those small scale motions having periodicities more than the boundary layer turbulence scale and less than the scale resolved by meso timescale [81]. Typically, submesoscale motion falls in the spatial scale of a few hundreds of meters and timescale of a couple of tens of minutes. Cloud structures like cells, streets, and brush-like pattern are some of the visual manifestations of these structures [46].

From the weather point of view, these structures have minimal influence but could impact the atmospheric dispersion of pollutants [44, 127]. Many authors in the past studied submesoscale motions. There are many reasons reported for the occurrence of such motions [66]. A few of the causes of submeso motions are gravity waves and vortices with a horizontal or vertical axis. Using Mesosphere-Stratosphere-Troposphere (MST) radar at Gadanki, India. Satyanarayana et al. [128] observed theses roll structures before a thunderstorm activity. Hartmann et al., [129] have attempted to simulate the roll structures using two-dimensional models based on the observed homogeneity in the direction of the mean wind. Roll and cell structures are also simulated using large eddy and high-resolution modeling techniques [59, 130]. Cloud street structures using high-resolution three dimensional model have been studied [131, 132] and conditions for the occurrence of such structures with respect to stability parameter, Z_i/L has been put forward. Wavelet transforms show that these coherent structures exhibit universal properties independent of the terrain features, frequency of occurrence, duration and time separation of the coherent structures and their relative contribution to the total fluxes such as momentum and heat under any stability conditions [133].

This Chapter elucidates the study of roll structures within the sea breeze in a tropical coastal environment, Kalpakkam using the SODAR and sonic anemometer data. The observed waves are subsequently simulated using an operational mesoscale weather model, WRF, in high spatial resolution to understand the condition under which they occur. Furthermore, the effect of these motions on dispersion predictions is also discussed. Section 2.2 discusses the site, data, and the configuration of the numerical model, WRF. Section 2.3 describes the results from SODAR observations, Fast Fourier Transform (FFT), and wavelet analysis using a tower, sonic anemometer data, and the results of numerical simulations. Section 2.4 and 2.5 discuss the configuration and results of simulation with FLEXPART-WRF. The conclusion of the study is given in section 2.6.

2.2 Site description and model configuration

Kalpakkam is located on the eastern coast of the Southern Indian peninsula at 12.57444^o N latitude and 80.17417 ^{o}E longitude, 80 km south of Chennai. The terrain is plain and gently sloping about l0 m above Mean Sea Level (MSL). The coastline is linear and runs along the SSW-NNE direction. The sitemap and measurement locations are shown in Fig. 2.1. In Kalpakkam, around 80% time of the year, sea – land breeze wind circulation occurs. At Kalpakkam site, wind speed (NRG 40C), wind direction (NRG 200P), air temperature (Rotronics), and relative humidity sensors (Rotronics) are installed at five levels, i.e., at 2 m, 8 m, 16 m, 32 m and 50 m above ground level (AGL) on a tall meteorological tower (12.56397^0 N, 80.1274^0 E). The data are archived every 10 min. Fast response measurements are made using an ultrasonic anemometer (R.M. Young Ltd) installed on a 10 m mast (12.583891^0 N, 80.17347^0 E) with a sampling rate of 10 Hz. The vertical profiles of wind and turbulence parameters are measured using a phased array Doppler SODAR (Make: Society for Applied Microwave Electronics Engineering & Research (SAMEER)) (12.583891^0 N, 80.17347^0 E). The SODAR and the tower are installed at about 1 km, 5 km respectively away from the coast. The details of the sensors used in this study, its make etc. is given in Annexure-1. A water body shown on the western side of the SODAR is a shallow backwater that remains dry in summer months. The operating frequency of the SODAR is 1800 Hz, with a pulse width of 180 ms. The output consists of three Cartesian components of the wind, and their respective standard deviations averaged over 15 min at height intervals of 20 m up to a vertical range of about 500 m. Fig. 2.2 shows hourly wind velocity averaged over each month of the year 2009. The wind speed and direction data is taken from 8 m level measurement from the 50 m tower. For example, the hourly mean wind velocity at the 0^{th} hour of each day for 31 days is averaged in January and is shown as a vector in the lower-left corner in the figure.

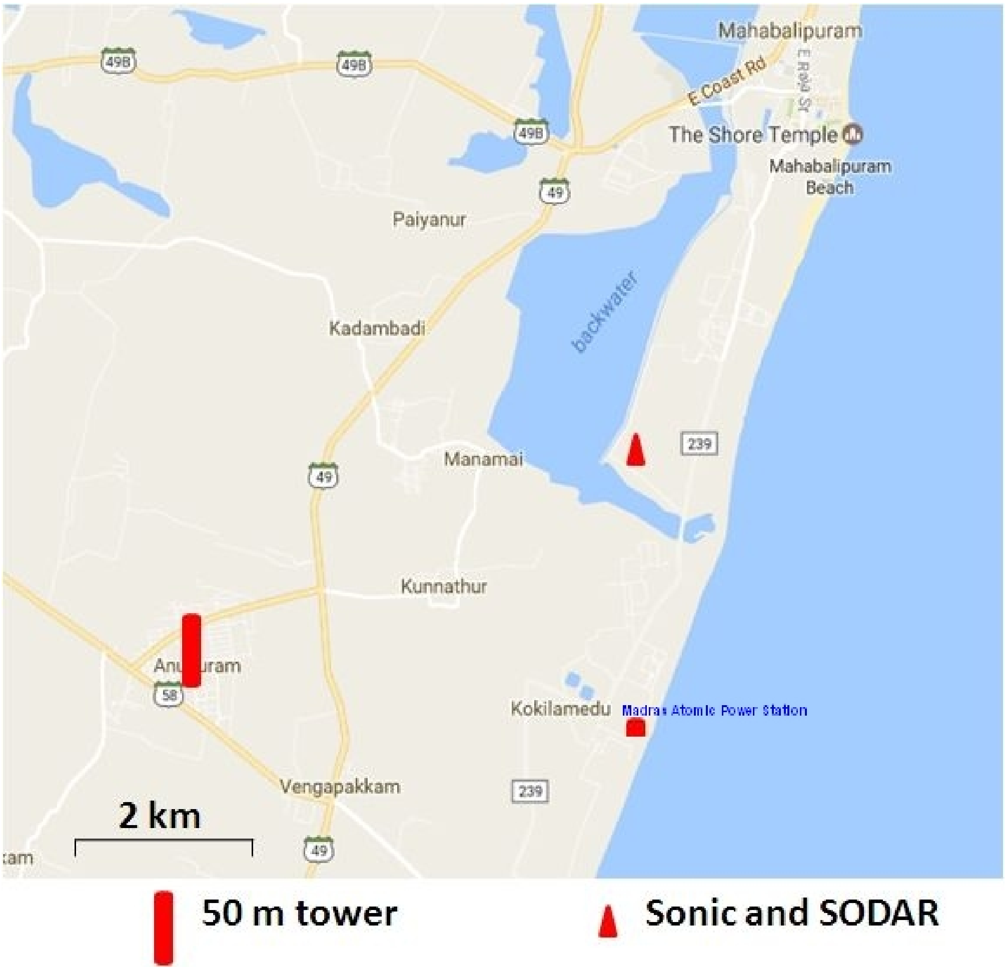

Figure 2.1 – Sitemap with the location of the tower, SODAR, sonic anemometer, etc. (Courtesy: Google Maps)

The arrows stacked one above the other corresponds to the progressive hours of the day, as indicated in the *y*-axis. As the time of the day progresses in January, the weak wind from the NE direction backs into a feeble land breeze from the NW at about 0400 Indian Standard Time (IST) (Greewich Mean Time (GMT)+0530). Sea breeze sets at 1000 IST, which persists up to midnight. The nearest grid point surface wind data for the monthly mean from the National Center for Environmental Prediction (NCEP) during 2009 are shown at the top of Fig. 2.2 as black arrows (synoptic wind). This data indicates the prevailing large-scale wind velocity, which is sampled and refitted to a grid of resolution 1^{o}. The arrow of the large-scale wind shows an onshore flow during six months, i.e., November, December, January, February, March, April and offshore during the other six months. In June, synoptic wind becomes active and it coincides with the onset of Southwest monsoon and continues in the westerly direction until October. With the beginning of the winter, in November, wind direction shifts to the Northeast. Other arrows in the figure below this synoptic wind arrow show the monthly averaged local wind for each hour of the day from the tower data.

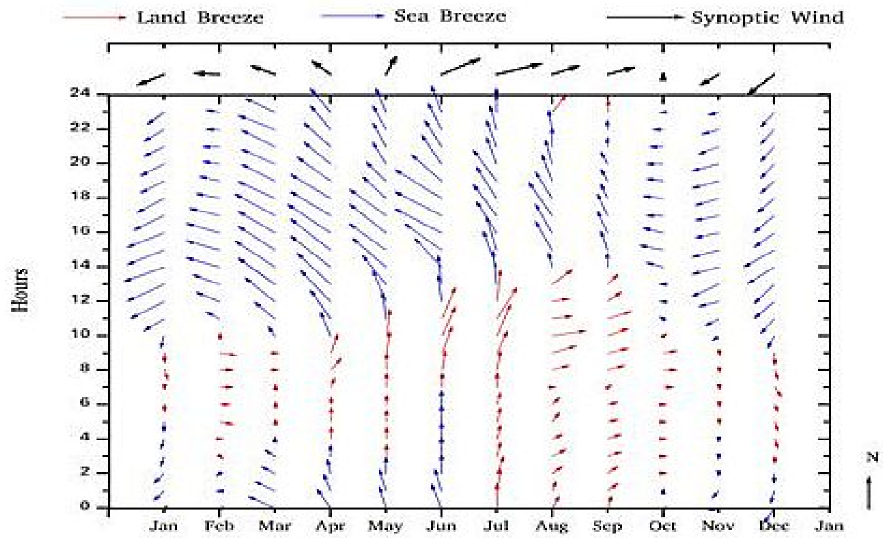

Figure 2.2 – Mean diurnal variation of the monthly averaged hourly wind (in m/s) at 8m AGL at Kalpakkam for 2009. The black arrow represents the synoptic wind from NCEP

The large-scale wind data, along with the tower data for the same period, helps to understand the diurnal wind pattern at the given site. The hourly profile of wind velocity clearly shows the onset of local land breeze in the morning hours up to 1000 IST and sea breeze in the afternoon hours. The onset of the sea breeze occurs approximately at 1000 IST during winter months due to weak and aiding large-scale wind and at around 1400 IST, during the summer Southwest monsoon months with the relatively strong opposing large scale wind.

To simulate the sea breeze wind and turbulence structure in detail, a high-resolution mesoscale model WRF is utilized for the present study. The WRF model is a Numerical Weather Prediction (NWP) model that solves the compressible non-hydrostatic Euler equations casted in flux form on a mass-based terrain-following vertical coordinate system. It solves prognostic equations for variables such as the horizontal and vertical wind components, various microphysical quantities, and the perturbation potential temperature, geopotential, and surface pressure of dry air. It is a fully compressible, non-hydrostatic model. The model uses the Runge–Kutta 3rd order time integration scheme and the 2nd to 6th order advection schemes in both horizontal and vertical directions. A complete description of the WRF modeling system is available in Skamarock et al. [134]. The present study employs WRF in high-resolution, in a nested configuration of five domains with a grid size ratio of 1:3:3:3:3.

Table 2.1 – The domain dimensions and the number of grid cells for each domain

Domain No.	Grid size	Number of cells in the x-direction	Number of cells in the y-direction
1	27 km	60	60
2	9 km	67	67
3	3 km	82	82
4	1 km	151	151
5	0.333 km	91	91

The grid resolution of the master domain is 27 km and that of the innermost domain is 0.333 km. The domain dimensions and the number of grid cells for each domain are shown in Table 2.1. The domain setup for WRF simulation is shown in Fig. 2.3.

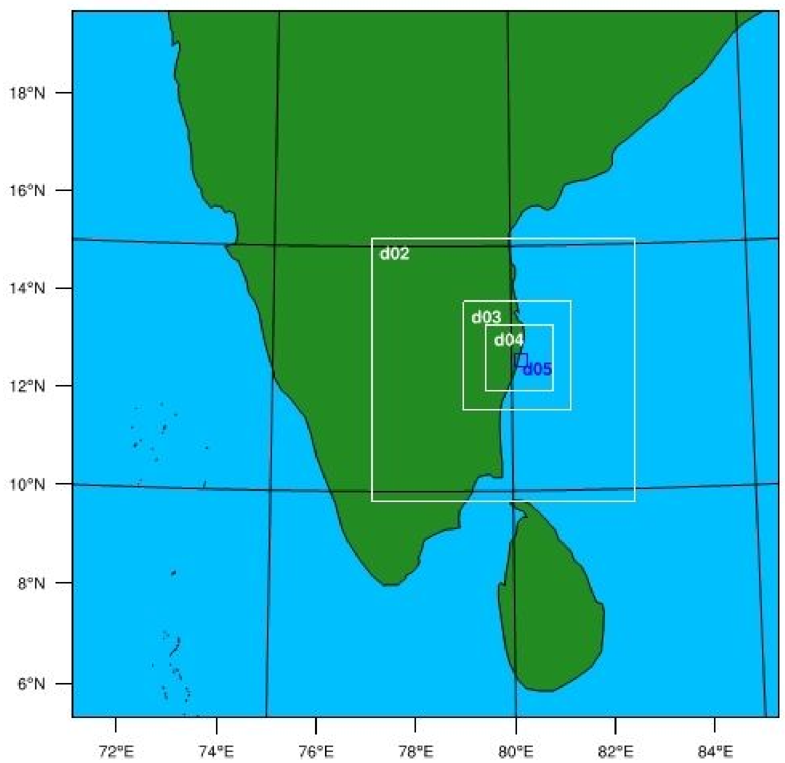

Figure 2.3 – The domain configuration for WRF simulation

The model uses the terrain from the United States Geological Survey (USGS) in 30-sec spatial resolution for the innermost domain and land use class employs Moderate Resolution Imaging Spectroradiometer (MODIS) data, which has a spatial resolution of 30 sec. The Mellor-Yamada-Janjic (MYJ) scheme [135] is used as the boundary layer parameterization scheme in this case. The other physical parameterization schemes used in all model domains are Janjic Eta Monin–Obukhov surface layer scheme, Dudhia shortwave radiation, Rapid Radiative Transfer Model (RRTM) longwave radiation, WRF Single-Moment 6-Class (WSM6) microphysics, and the Noah land surface scheme. Cumulus scheme Grell is used only in the mother domain of 27 km. Each domain has 40 vertical layers with the model top at 50 hPa. Out of 40 vertical levels, 20 levels are within the first one km, with the first model layer approximately 20 m above ground level. NCEP-Global Forecast System (GFS) final (FNL) operational global analyses are used for initial conditions and boundary conditions.

2.3 Results and discussion

For the analysis, meteorological data collected over fifteen days using SODAR in the summer months of April 2011 is used. The Turbulence Kinetic Energy (TKE) is derived using the wind velocity standard deviations provided by SODAR. Analysis of TKE shows the presence of waves with a period of $\approx$ 30 min in the data. The time-height plot of wind velocity and TKE from SODAR observations shows the presence of such motions (waves with a period of $\approx$ 30 min) during sea breeze hours. Such motions can be detected from data using the spectral method. Spectral analysis of sonic anemometer data shows the presence of such small scale motions. Out of 15 days, two typical days (27 and 28 April 2011), where fast response sonic anemometer is available at Kalpakkam, are considered for detailed analysis.

2.3.1 Meso & submeso motions revealed by SODAR

The SODAR echogram usually shows a qualitative picture of the thermal stratification of the Atmospheric Boundary Layer (ABL). Latha and Murthy [136] described the technical specification of the SODAR with a few observations under convective thunderstorm conditions. To demonstrate the presence of submesoscale motions, TKE, e estimated from SODAR data is plotted as a function of time. The TKE is computed from the standard deviation of wind components as follows.

$$e = \frac{1}{2}\left(\sigma_u^2 + \sigma_v^2 + \sigma_w^2\right) \tag{2.1}$$

where, σ_i $(i = u, v, w)$ is the standard deviation of the wind velocity components. Fig. 2.4a to Fig. 2.4f show 15 min averaged time-height wind profile (in arrows, head pointing to the direction of flow) and TKE (in color shades) for a few days in summer viz-a-viz 06$^{\text{th}}$, 11$^{\text{th}}$, 17$^{\text{th}}$, 21$^{\text{st}}$, 27$^{\text{th}}$ and 28$^{\text{th}}$ April 2011. The figure shows the diurnal cycle of the mesoscale sea breeze circulation. Only data with good signal to noise ratio is considered for analysis. The time-height plot indicates the sea breeze onset at around 0900 IST on all the days. The surface-level winds are onshore at night, West/Southwest direction in the morning and East-Southeast or southeast (sea breeze) from 0900 IST lasting up to late in the night. Within the sea breeze mesoscale system, there are bands of high and low intensities of TKE periodically appearing at the interval of $\approx$ 30 min. These organized up and downdrafts are an indicator of large eddies or circulations having approximately $\approx$ 30 min periodicity. Moreover, it is observed that the intensity of such oscillations increases with height. The maximum intensity is noticed between 50-150 m. SODAR data analysis shows similar TKE intensity patterns for many more days in summer months (March to May) and a few clear sky days in winter months.

Lemone [47], Miao and Chen [132] and many other researchers reported that these types of periodic oscillations are quite frequent in the slightly convective boundary layer over ocean and land surfaces. It is observed as alternate spells of wind speed and temperature fluctuations of periodicity around 30 min, and it is more clearly noticed in the time series of TKE obtained by measurement from tall towers [47] and wind profilers [132]. It is described as a large coherent eddies extending to the top of the boundary layer and responsible for large momentum and scalar flux transfer [45, 137].

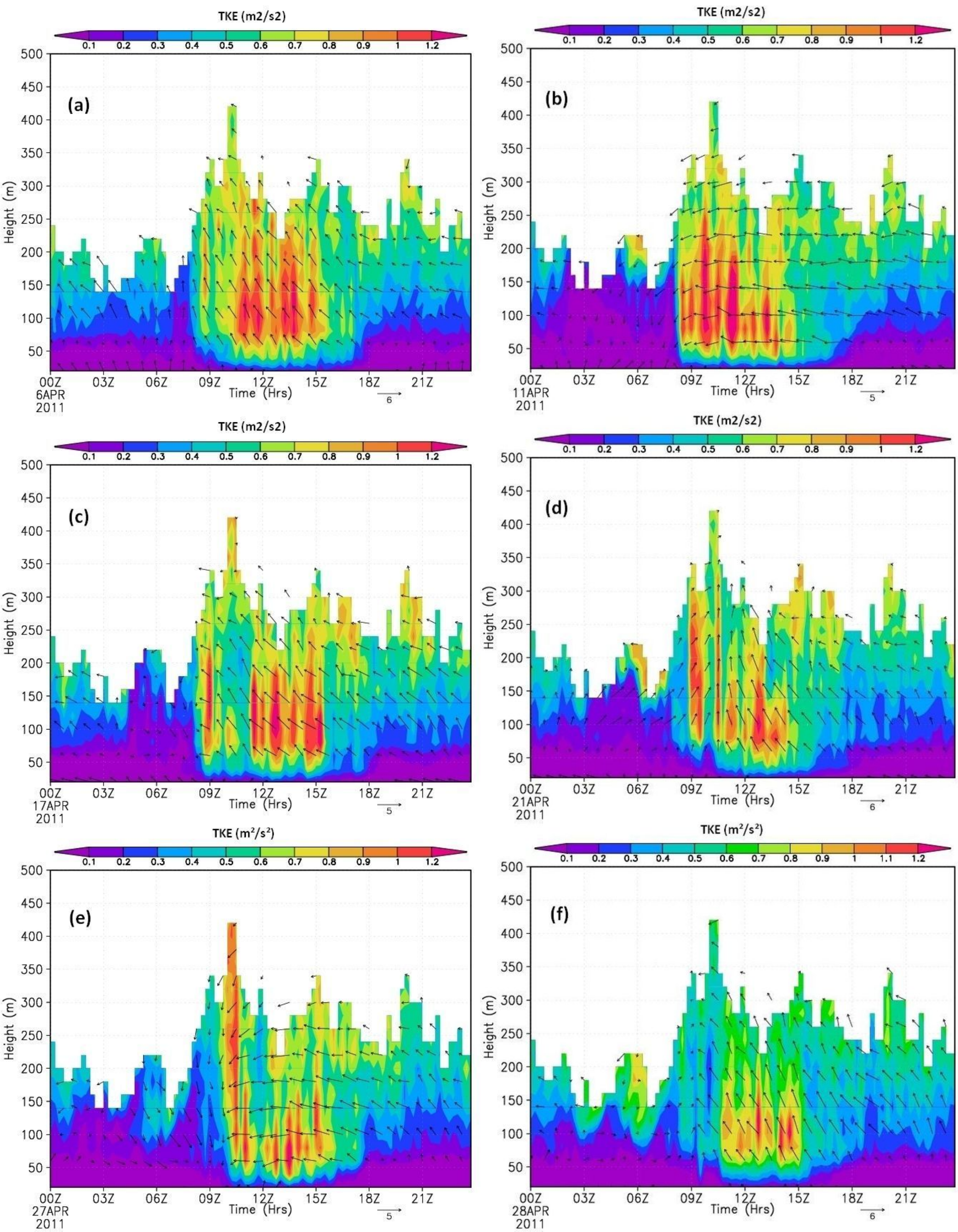

Figure 2.4 – Time-height plot of horizontal wind vector (arrows) and TKE (color shades) on (a) 06rd April 2011, (b) 11th April 2011, (c) 17th April 2011 (d) 21th April 2011, (e) 27th April 2011 and (f) 28th April 2011

The small wavelength of the HCR within the internal boundary layer and lack of clouds above this layer make this phenomenon undetected by naked eye observation. Usually, such Quasi-stationary and organized large eddy structures are common features in the ABL. Structures like two-dimensional cloud streets or three-dimensional cloud cells are among the visual manifestations of the underlying ABL organization. The measurements using wind profiler and tall towers have shown the presence of HCRs in ABL during which 20-30 min periodic waves are present. High-resolution satellite pictures show the presence of these structures. Sandeepan et al. [44] reported the presence of convective rolls over this study region Kalpakkam. At coastal areas like Kalpakkam, the regions where the sea breeze is advanced show no clouds. Dual-Doppler lidar measurements showed the presence of HCRs in the sea breeze [138, 139]. Observed wavelengths of HCRs were of the order of 450 to 500 m. Mitsumoto and Ueda [140], using laboratory-scale simulations, predicted the existence of HCRs in the sea breeze layer. Below the height of laterally drifting HCRs, TKE is enhanced where convergence occurs and reduced at the divergent regions. This is the possible explanation for high-low bands in TKE observed by SODAR (Fig. 2.4a to Fig. 2.4f).

2.3.2 FFT analysis of long term data of Kalpakkam

The spectral characteristics of wind fluctuations have been studied in the past to get an insight into the wide range of scales of the atmospheric motions [141, 142]. Many researchers have shown that [143, 144] the atmospheric motion prefers specific frequencies with gaps in between rather than spreading uniformly to entire frequencies. Many of these studies reported above use measurement from 100 m levels where the speed is relatively higher than the measurement at 8 m levels. Therefore the influence of the ground surface is likely to be low [145]. Also, since the spectral studies reported by these researchers are for flat homogeneous terrain, they are likely to be different for a coastal site. Thus the submeso motion of the periodicity $\approx$ 30 min is not noticed. The wind speed and temperature data for the Kalpakkam site are analyzed to identify such motions using the FFT technique. Four years of data from the cup anemometer mounted at 8m height on a 50 m tall meteorological tower is used for this purpose. The spectrum is shown in Fig. 2.5. The figure shows strong diurnal, semi-diurnal oscillation, and the yearly synoptic-scale peak at the low-frequency end, which is not very strong in the mesoscale range. However, the 2 m level air temperature spectrum from the tower (Fig. 2.6) shows similar characteristics of Fig. 2.5, but the amplitude of yearly oscillation has substantial strength.

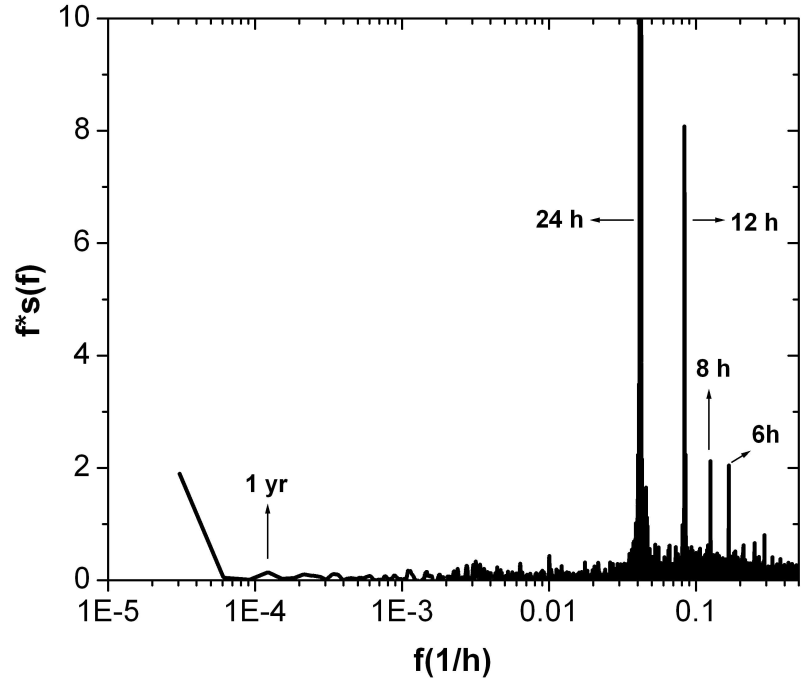

Figure 2.5 – Spectrum of four years hourly wind data (at 8 m AGL) from the tower (y-axis denotes frequency weighted power)

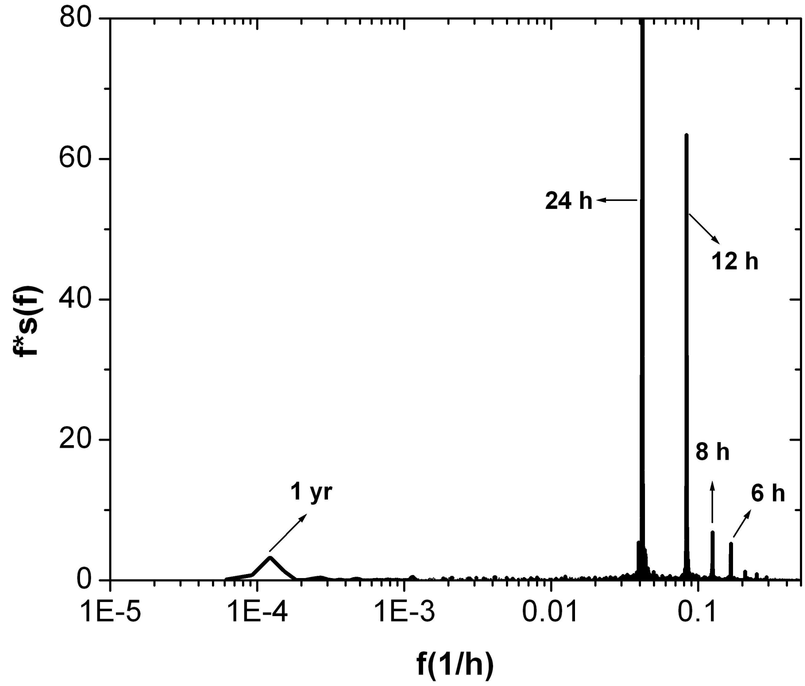

Figure 2.6 – The spectrum of four years hourly temperature data (at 2 m AGL) from the tower (y-axis denotes frequency weighted power)

This is because the air temperature represents solar insolation, which follows regular cycles in the large-scale and represents the local convective eddies in microscale. The thermal energy is more in the large-scale temperature waves. However, in the case of wind, the mesoscale cycles and the turbulence scales show more energy.

2.3.3 Analysis of sonic anemometer data over Kalpakkam

The analysis described in the previous sections used data from a slow response anemometer mounted on the meteorological tower. It is to be noted boundary layer turbulent information at the tail end is absent in the spectrum. For a more detailed analysis, the fast response ultrasonic anemometer data available on 27th and 28th April 2011 are subjected to FFT. The data is quality checked before analysis by visual inspection and double rotation. The FFT spectrum for 27th and 28th April 2011 is shown in Fig. 2.7a and Fig. 2.7b respectively. The figures indicate a peak at 20-30 min (low energy) and 2-10 min in the horizontal component of the wind. The peak due to the convective eddies at $\approx$ 2-10 min is reported by many authors [124, 146]. Moreover, the peak at $\approx$ 2 h is also reported by Fielder and Panofsky [143]. They indicated that such peaks arise due to fluctuation in the averages (less than a minute) caused by microscale gusts and lulls. However, the vertical component of the wind velocity does not show such a peak within these frequency ranges (not shown). Bradley [147] and by Panofsky et al. [148] reported similar multiple periodic waves over other non-coastal, hilly complex terrain conditions in the transverse and longitudinal component of the wind.

Another study by Li et al. [149] over a large valley on the Loess Plateau in China in near-neutral conditions showed that the spectrum of the horizontal components coincided with those obtained from any other site at the high-frequency range. However, for low frequencies, the spectrum is affected by local inhomogeneities leading to a double-peak pattern, one representing the synoptic waves with $>$1h period and the second peak in $<$10-minute range that falls under the well-defined category of boundary layer turbulence scale. In the case of Kalpakkam, a third peak is observed between these usual peaks over a homogeneous terrain. This peak observed at approximately 20-30 min is different from the turbulent scale as well as the hourly mesoscale due to the sea breeze. These submesoscale motions of periods above 10 min and below 1h must be due to different physical phenomena like organized HCRs during daytime convective conditions or within the sea breeze layer, which exists in this region.

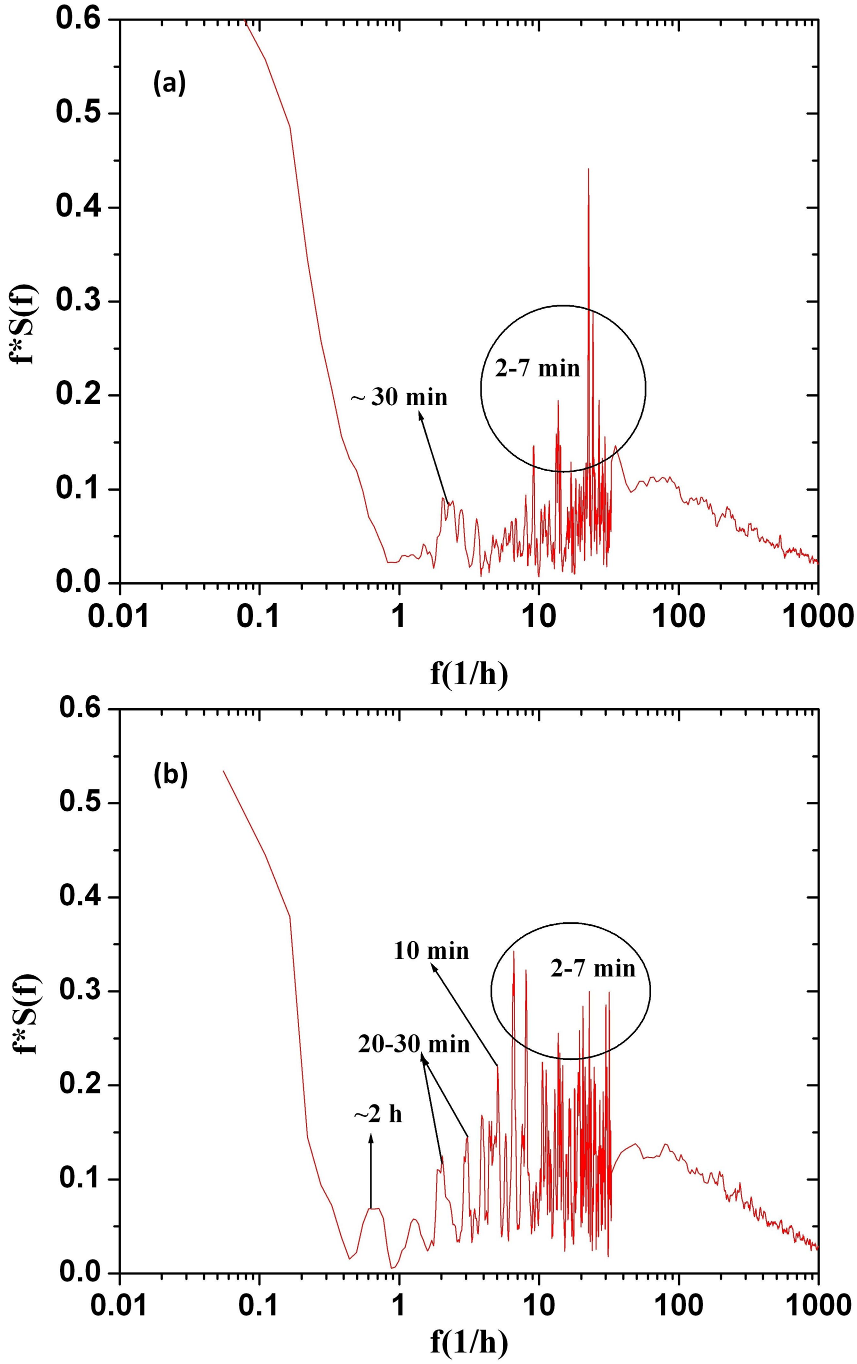

Figure 2.7 – Horizontal velocity spectrum for (a) 27 April 2011 (b) 27 April 2011 (y-axis denotes frequency weighted power)

Generally, the FFT operates in frequency space, and therefore, the time information will be lacking in FFT analysis. One of the techniques by which the time information is retrieved is by using wavelet analysis. Therefore, for further study, wavelet analysis is used. A brief description of the wavelet technique and subsequent study are given in the next section.

2.3.4 Wavelet technique

The wavelet transform technique is mainly used to analyze non-stationary time series that contain many different frequencies [150]. In many aspects, wavelet analysis is a technique very similar to the FFT. However, while the FFT scans for a frequency component present throughout the entire signal (single window), wavelet analysis uses a short and long window for high and low frequencies, respectively. Wavelet analysis is done by projecting the signal on to a set of wavelets or otherwise called basis functions. This basis function is obtained from a mother wavelet by translation and dilation method. There are many wavelet mother functions available viz-a-viz Paul, Harr, Morlet, DOG, etc. Morlet is one of the most widely used continuous wavelets in geophysics, consisting of a plane wave, modified by a Gaussian envelope [151, 152]. The advantage of using Morlet wavelet is its complex nature that enables the detection of both time-dependent amplitude and phase for different frequencies present in a time series [153].

Morelet is defined by

$$\psi(t) = exp(i\omega_{\psi}t)exp\left(\frac{-t^2}{2}\right) \tag{2.2}$$

ω_{ψ} is the empirical constant that makes the wavelet admissible. The study uses the wavelet algorithm from Torrence and Gilbert [154]. Fig. 2.8 and Fig. 2.9 show the wavelet power spectrum using this algorithm for 27 and 28 April 2011, respectively. Fig. 2.8b shows that a relatively strong power is concentrated within a period $\approx$ 30 min that lasted from 0200 IST up to 0400 IST on 27 April 2011. A feeble land and sea breeze oscillation persist during this period, as seen in Fig. 2.8a. Such motions die out after 0400 IST when the land breeze sets (the power band at 20-30 min disappears). The sea breeze onset is indicated by the change in the sign of the u-component of the wind velocity (Fig. 2.8a). After 0700 IST, the wave motion reappears with its full intensity and reaches a maximum at 0900 IST where sea breeze sets in, and the wave motions continue throughout the sea breeze hours. Fig. 2.10a and Fig. 2.10b show the corresponding global wavelet spectrum for 27 and 28 April 2011, respectively. The power spectra show a peak at $\approx$ 32 min. The figure also shows waves of 10 min period intermittently appearing during the daytime convective conditions. Similar is the case with data on 28 April as seen from Fig. 2.9a and Fig. 2.9b.

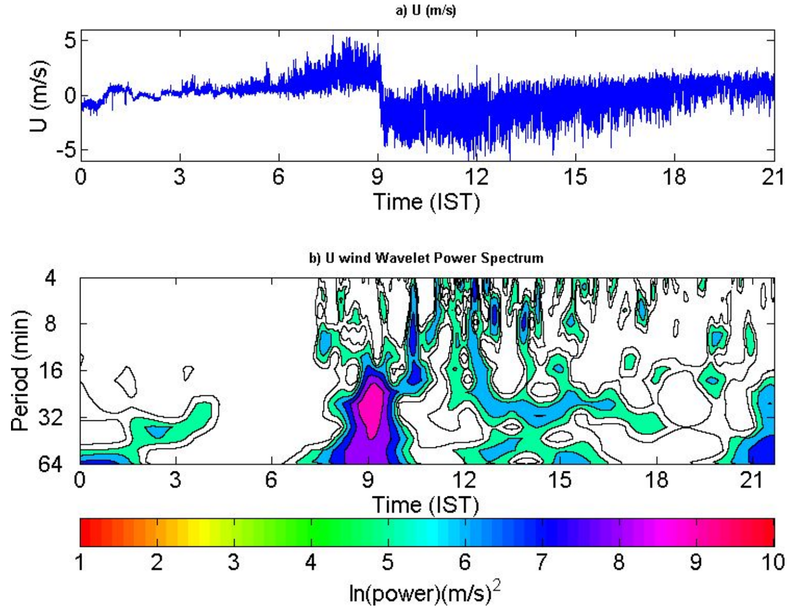

Figure 2.8 – (a) The u-component of wind velocity (in m/s) on 27 April 2011 and (b) its wavelet transform

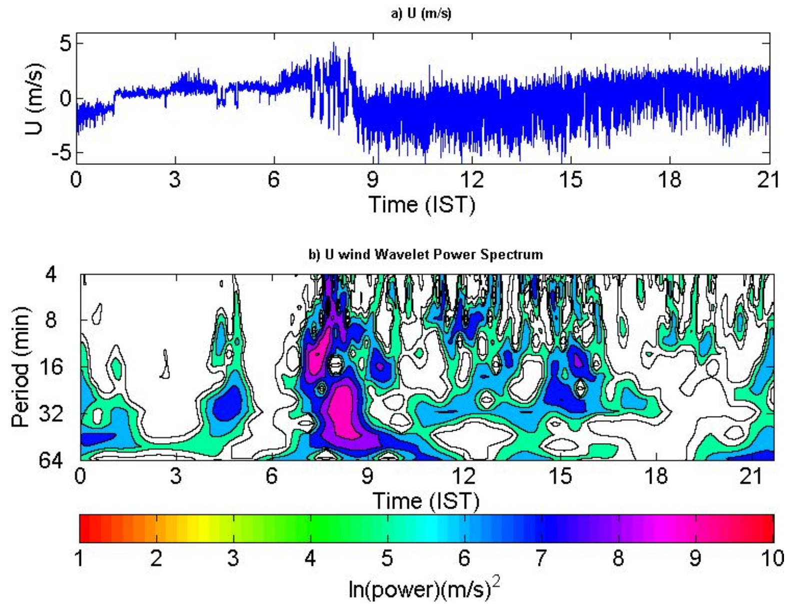

Figure 2.9 – (a) The u-component of the wind velocity (in m/s) on 28 April 2011 and (b) its wavelet transform

Here too, at the time of onset of the sea breeze, the 20-30 min wave appears strongly and is present throughout the sea breeze hours. Moreover, waves of the period 10 min also appear during the convective time of the day. The global wavelet spectrum shown in Fig. 2.10 also indicates a peak of around $\approx$ 30 min. Other peaks of 10 min and less periodicity are also evident from the figure.

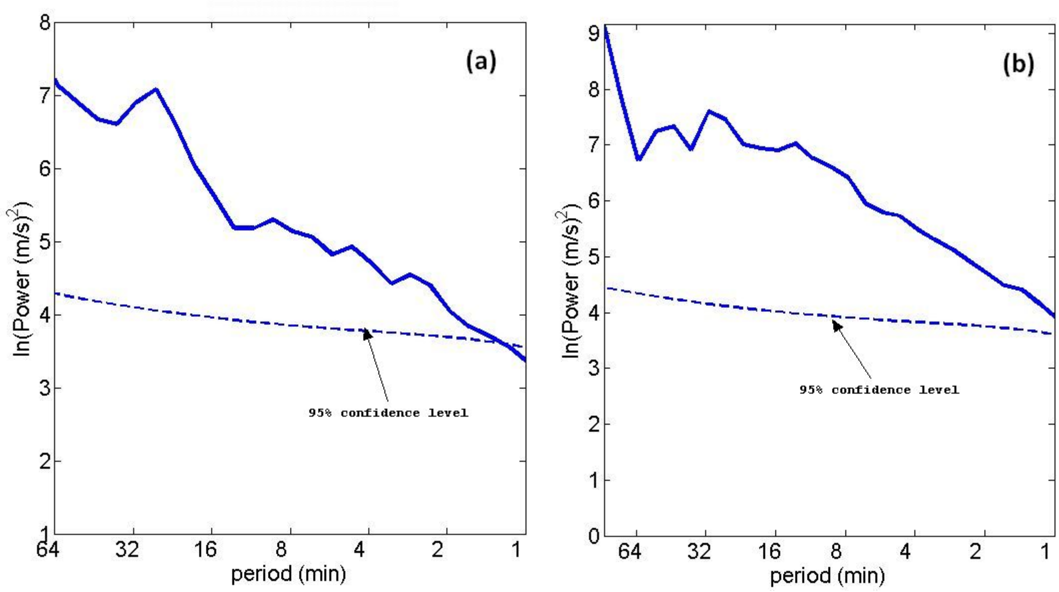

Figure 2.10 – (a) The global wavelet spectrum on 27 April 2011 (b) the same on 28 April 2011

The dotted line in Fig. 2.10 signifies the significance level. Based on Torrence and Compo [154], a confidence level of 95% is taken for the assessment of wavelet coefficients. The significance level is determined by assuming red noise as the background spectrum. The significance level is estimated by choosing a lag of -1 auto-correlation of the time series. In a nutshell, the analysis indicates that submesoscale waves of period 20-30 min are present throughout sea breeze hours with varying intensity. However, the 10 min waves are present only during the daytime convective condition. The wave of 20-30 min, which occurs during the sea breeze hours, is attributed to HCRs whose presence is also shown by SODAR. Further, to study the structure and conditions of occurrence of HCR, numerical simulation using WRF is conducted and is discussed in the next section.

2.3.5 Results of WRF simulation

The WRF model is initialized at 0530 IST (0000 GMT) on 26 April 2011, and simulation is continued for 72 hrs. Fig. 2.11 shows the comparison of simulated and observed wind direction for 48 hours, starting from 27 April 2011 at 0000 IST. The Fig. 2.11 shows that the simulated wind direction (every 10 min) is in close agreement with observation.

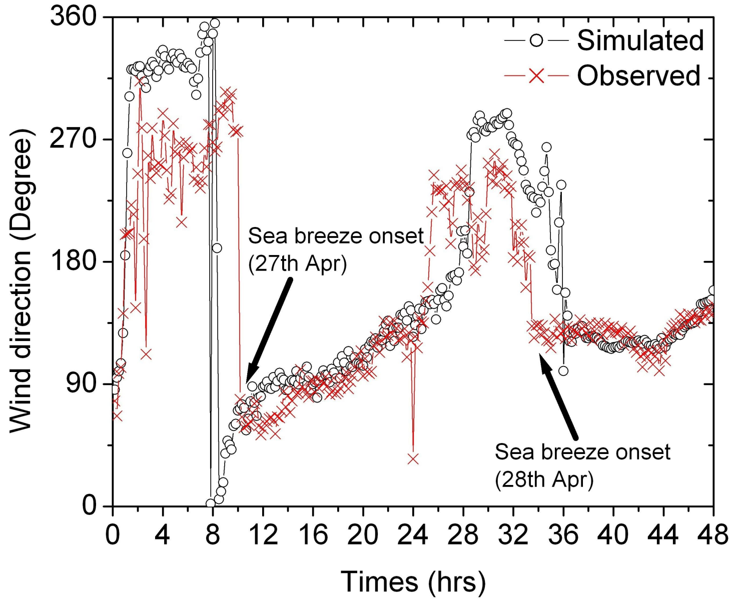

Figure 2.11 – Observed and simulated (using 333.333 m resolution) wind direction at 10 m AGL

It is observed from the figure that the model predicted the onset of sea breeze roughly one hour before the actual onset on 27 April and one hour later on 28 April. This difference may be due to the boundary layer parametrization used in the model because the choice of Planetary Boundary Layer (PBL) scheme in WRF has an impact on sea breeze simulation [155]. Further, Fig. 2.12 shows the comparison of estimated (using sonic anemometer) and simulated sensible heat flux on both days.

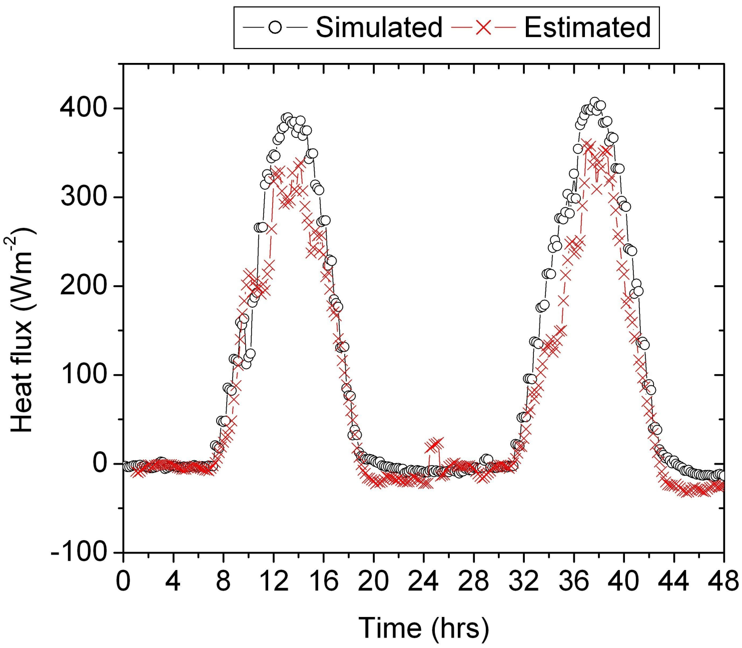

Figure 2.12 – The estimated and simulated sensible heat flux (in Wm^{-2}) on 27 and 28 April 2011

The figure indicates that the simulated heat flux is in good agreement with observation. The sensible heat flux is estimated from the sonic anemometer data using the eddy covariance method. Using this method, the sensible heat flux is estimated using $\overline{w'T'}$. The vertical turbulent flux, $\overline{w'T'}$ is estimated using an averaging time of 30 min. The simulation shows that before the onset of the sea breeze, convection is manifested in the form of cells. One such case is shown in Fig. 2.13.

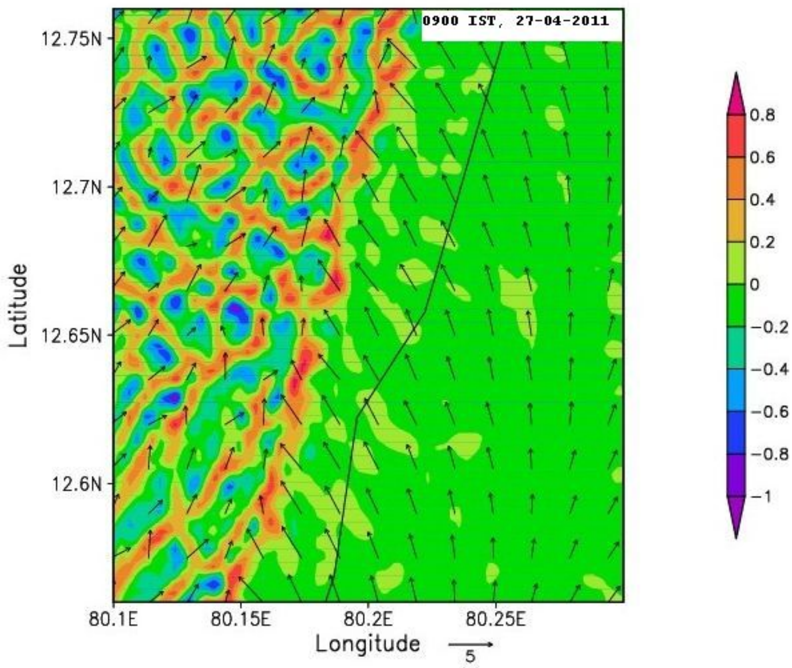

Figure 2.13 – Convective cells before the sea breeze onset. The color shades show the vertical wind velocity. The arrows denote the horizontal wind vectors at 10 m AGL

After the onset of the sea breeze, these structures organize into rolls and align themselves along the wind vector within the PBL. It is also found that the low-resolution domains (1 km and 3 km in this case) are not successful in simulating the observed submesoscale waves. This is because of the averaging out of these observed waves of the period 20-30 min by the low-resolution grid (Fig. 2.14). But these waves of 20-30 min period can be simulated using high-resolution grids. Fig. 2.15 and Fig. 2.16 show the simulated time-height plot of TKE from WRF simulation similar to the SODAR figures (Fig. 2.4e and Fig. 2.4f) on 27 and 28 April 2011. There is a good qualitative agreement between the simulated values and the SODAR data (see Fig. 2.4). The HCRs in the form of TKE bands are simulated similar to the observed ones. Many authors in the past reported the condition of the occurrence of HCR. Deardorff [156] used the Obukhov length L to predict the onset of coherent rolls. Later, Grossman [51] in terms of stability parameter Z_i/L, (where Z_i is the boundary layer height) characterized different types of convection. He reported that for $-Z_i/L > 5$, convection manifests in the form of rolls, whereas 3D convective cells exist for $-Z_i/L < 25$ and mixed type of organized convection occurs within this range [44].

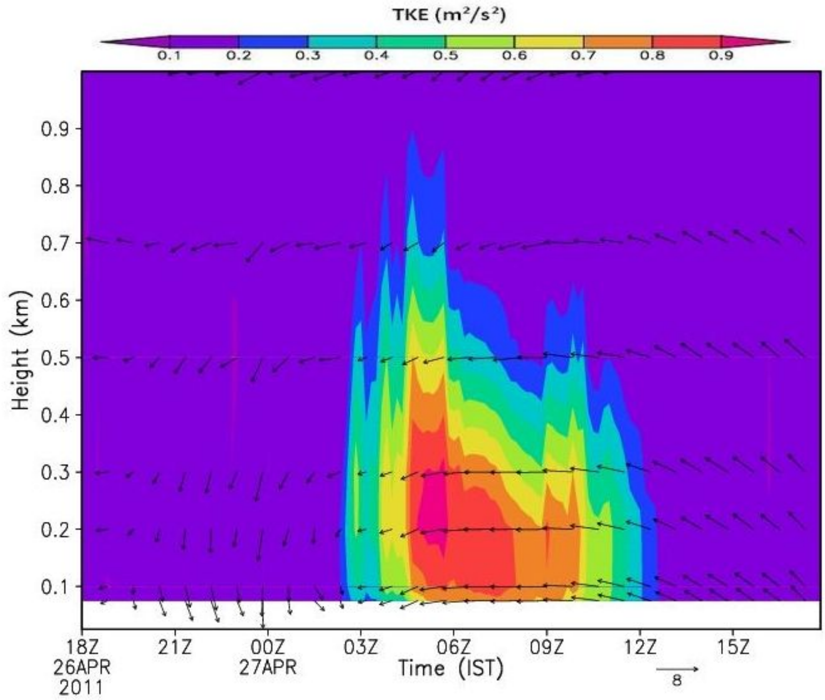

Figure 2.14 – Time-height plot of TKE with wind vectors (in m/s) on 27 April 2011 with 1 km resolution grid in the WRF model at SODAR location. The arrows denote the horizontal wind vectors.

Roll clouds have been studied in high-resolution three-dimensional models ([131], [132]). Their study also showed agreement with the condition $-Z_i/L < 25$ for the formation of rolls. However, the existence of rolls during pre-sea breeze conditions for $-Z_i/L > 50$ is also reported [44, 157]. However, in our simulation, the existence of the rolls for stability parameter $6 \leq Z_i/L \leq 20$ is noticed within the sea breeze. Weckworth et al. [45] reported the conditions of occurrence of these structures by analyzing the wind speed, stability parameters, and heat fluxes. Our study shows that, on both the days, during the sea breeze hours, the wind speed is above 4 m/s, the estimated heat flux is below 350 W/m^2. The estimated stability parameter is $10 \leq Z_i/L \leq 25$ on both the days during sea breeze hours. Therefore, the requirement of minimum wind speed and heat flux for the occurrence of

HCRs is satisfied, as reported by Weckworth et al. [45].

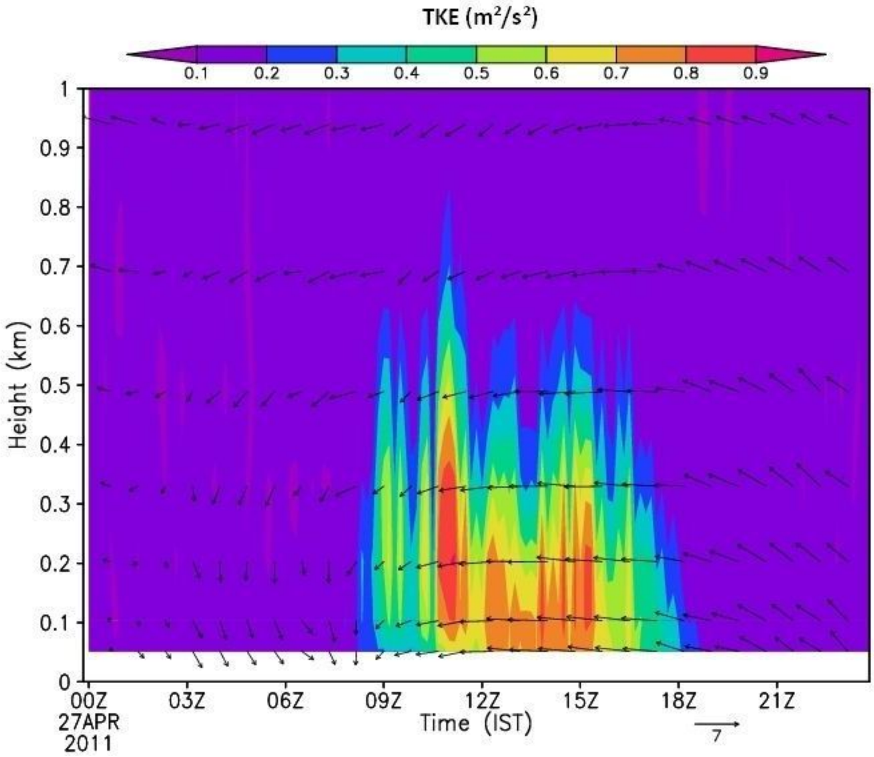

Figure 2.15 – Time-height plot of TKE with wind vectors (in m/s) on 27 April 2011 with 333.333 resolution grid in the WRF model at SODAR location. The arrows denote the horizontal wind vectors.

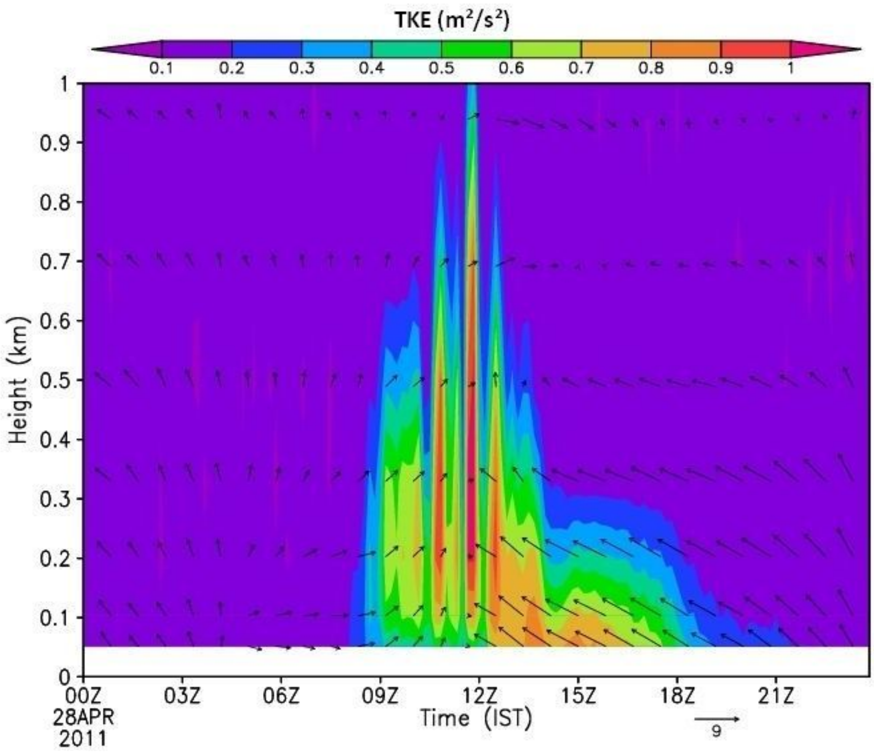

Figure 2.16 – Time-height plot of TKE with wind vectors (in m/s) on 28 April 2011 with 333.333 resolution grid in the WRF model at SODAR location. The arrows denote the horizontal wind vectors.

It is further noticed that the estimated range of stability parameters is in agreement with the simulated values mentioned above. Within the sea breeze layer, to have this range of stability parameters, there are two competing factors. One is the boundary layer height, which manifests into a TIBL under the sea breeze, and the other is the Obukhov length, L. Studies conducted at this site show that the height of TIBL is around 150 m near the coast during the sea breeze hours [158]. The study also reported the variation of stability parameter and boundary layer height at different times of the day. It is found that though there is a sudden decrease in the value of boundary layer height due to the sea breeze, the value of L does not decrease to the same extent. These changes resulted in the reduction of $-Z_i/L$ values by a factor of 3 to 4 from the otherwise normal boundary layer. Fig. 2.17a&b shows the simulated spatial structure of simulated HCRs at the height of 100m after the onset of the sea breeze on 27 and 28 April 2011 respectively.

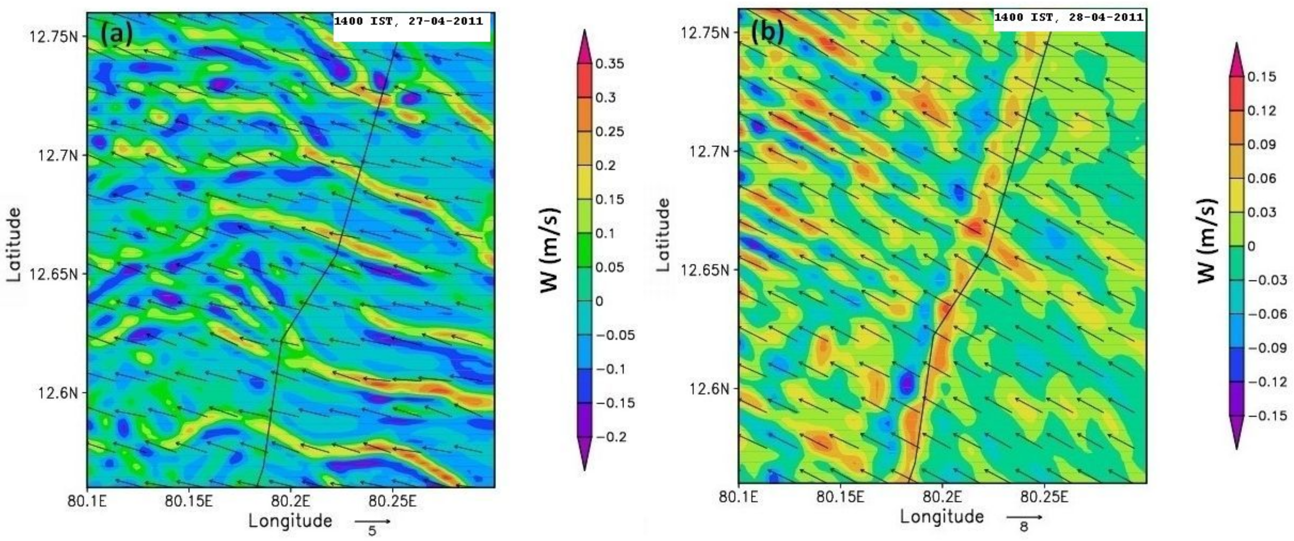

Figure 2.17 – Simulated vertical velocity superimposed over the wind vector above 100 m AGL at (a) 1400 IST on 27 April and (b) 1400 IST on 28 April

The simulated heat flux is less than 350 W/m^2 in the region where the rolls are distinct (Fig. 2.17a). The simulated wind speed at this level (100 m) is 6 m/s. Similarly, the distinct roll structures are formed on 28 April 2011 (Fig. 2.17b) for the simulated heat flux less than 380 W/m^2 with the average wind speed of 10 m/s at 100 m level. Thus the condition of existence of rolls in terms of $-Z_i/L$ [51, 159], minimum wind speed and heat flux (within 400 W/m^2) [45, 160] are satisfied on both the days. Since HCRs have periods below the mesoscale time scale, these motions can be classified as submesoscale.

2.3.6 Results of simulation with FLEXPART

FLEXPART-WRF is an LPDM for simulation of transport and diffusion of pollutants in the atmosphere. It is a LPDM that uses the meteorological fields predicted by the weather prediction model WRF. In FLEXPART, large amounts of particles are released, and the trajectory of each particle is calculated to simulate particle transport and dispersion. The position of the particle at $X(t+\triangle t)$ after a time $t+\triangle t$ is given by

$$X(t+\triangle t) = X(t) + \left[\bar{u}(t) + u'(t)\right]\triangle t \tag{2.3}$$

Where $\bar{u}(t)$ is the mean, and $u'(t)$ is the fluctuating part of the wind velocity. The turbulent part of the wind velocity $u'(t)$ is obtained from the Langevin equation as

$$du' = -\left(\frac{u'}{\tau_L}\right)dt + \sigma_u\left(\frac{2}{\tau_L}\right)^{1/2}\zeta(t)dt \tag{2.4}$$

Where τ_L is the Lagrangian time scale, and ζ(t) is the Gaussian random number with zero mean and variance unity. σ_u is the standard deviation in the along wind direction. A similar relationship applies to the transverse component of the wind. In the case of vertical wind component, in order to take into account the density stratification and well-mixed criterion, density and drift correction terms are added to the equation. Thus the Eqn. 2.4 written for w' in FLEXPART is given below.

$$dw' = -w'.\frac{dt}{\tau_{Lw}} + \frac{\partial\sigma_w^2}{\partial z}dt + \frac{\sigma_w^2}{\rho}.\frac{\partial\rho}{\partial z}dt + \left(\frac{2}{\tau_{Lw}}\right)^{1/2}\sigma_w.dW \tag{2.5}$$

Where ρ is the air density, and dW is the incremental components of the Weiner process with mean zero and variance dt. The second and third terms in Eqn. 2.5 are the drift and density corrections respectively. This model has been widely used to investigate particle transport paths and mechanisms [158, 161, 162]. For the current study, the averaging time chosen for the model is 60 min, and 1,000,000 particles were released for the simulation period. The time step is kept within the Lagrangian time scale for the detailed description of turbulence. The average standard deviation of the wind velocity vector is computed using the model default Hanna scheme [1]. Wind fields and other variables are supplied to FLEXPART from WRF at every 10 min interval to reduce the temporal interpolation errors.

The FLEXPART model is initialized at 1800 GMT on 26 April 2011, and simulation is continued till 0000 GMT on 29 April 2011. The wind inputs are supplied to FLEXPART from 333.333 m resolution and 1 km resolution grids in successive simulations. The normalized dose rate using inputs from both the resolutions for 24 hrs is compared at 5 km away from the release point (Fig. 2.18).

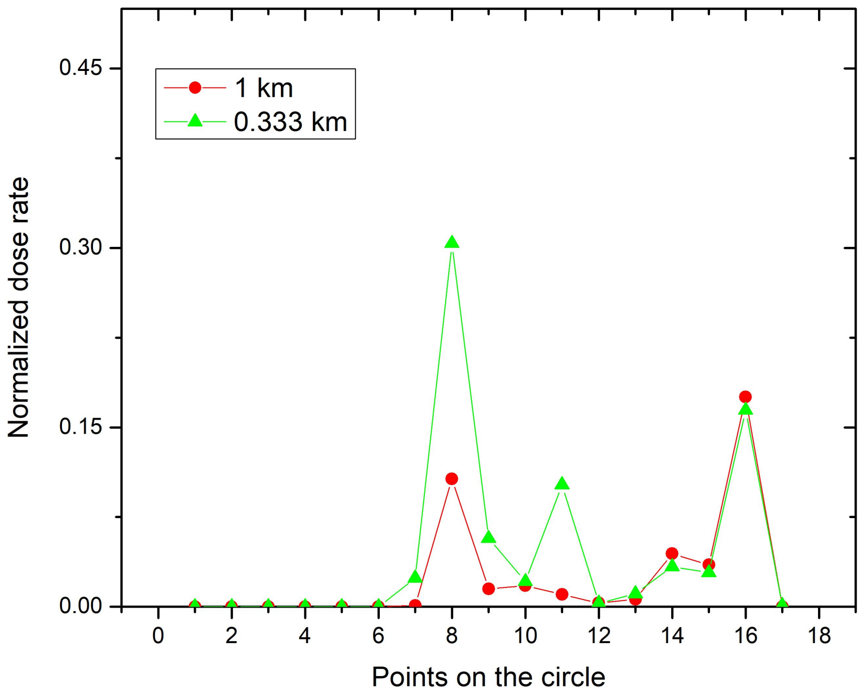

Figure 2.18 – The normalized dose rate at points located at 5 km radius about the release point

This approach covers all the sectors. It is seen from the figure that the inputs from the low-resolution domain will underestimate the radiological dose in a few sectors. This because, as already mentioned, rolls can be simulated only by high-resolution simulations. The horizontal rolls have convergence and divergence areas as already mentioned. The high vertical velocity in convergent areas lift the pollutants upwards in those areas, and the negative vertical velocity in divergent areas will bring down the pollutants, leading to more dose. Moreover, [44] reported possible trapping of the plume within the HCR, thereby restricting the dispersion within the rolls. These trapping of the plume within the HCRs can results in higher concentration/dose in these areas.

2.4 Summary

This Chapter discussed the observational analysis and numerical simulation HCRs within the sea breeze layer over the Kalpakkam site. The time-height profile of wind velocity and TKE from SODAR showed organized waves with a period less than the mesoscale and more than the boundary layer turbulence scale. Spectral analysis was carried out using the traditional FFT technique and modern Wavelet transform technique over the tower-based long-term data and the high sampling frequency data of wind using a sonic anemometer. Apart from regular diurnal, semi-diurnal, and high-frequency turbulence peaks, a significant presence of submesoscale motions in 20-30 min is revealed in the spectra. Such wave occurs mostly during the daytime sea breeze period. WRF could simulate these submesoscale motions in a high spatial resolution configuration. The time-height plot of the simulated wind velocity and TKE showed good agreement with the SODAR data. Moreover, the condition of occurrence of these submesoscale motions in terms of the ranges of wind speed, stability parameter, and heat flux, as reported by others, is also satisfied. This study assumes importance in the context of pollutant dispersion near coastal areas where these motions are often present and will influence the dispersion of pollutants with high concentration or dose at divergent areas.

Chapter 3

Dispersion under stable conditions

This chapter gives an overview of dispersion under stable atmospheric conditions. The Chapter discusses the parametrization of turbulence diffusivity under stable conditions, on the use of local similarity theory instead of MO theory, and benefit of using multi-resolution decomposition technique for the formulation of similarity relationship. Finally, the simulated dose rate using FLEXPART is compared using measurements using Autonomous Gamma Dose Loggers.

3.1 A brief on MO theory

The MOST [76, 163] is a widely used method to obtain surface layer turbulent fluxes in the atmosphere as a function of the non-dimensional stability parameter. Many boundary layer models employ it for obtaining the mean meteorological variables in the lower turbulent layer [164–166]. According to MOST, the turbulent fluxes of wind, temperature, and moisture in the surface layer are related to the vertical gradients of their mean quantities by an eddy diffusivity coefficient [167]. However, the application of MOST to stable atmosphere is not successful as it does not represent the turbulence and stability functions realistically due to the sensitivity to frequently observed submesoscale phenomena like gravity waves, meandering motions, radiative divergence, intermittency, etc. [61, 62]. Nieuwstadt [69] introduced the local scaling based on dry, second-order closure equations using Cabauw data, which showed the existence of z-less stratification and properties of turbulence under highly stable conditions. The hypothesis states that dimensionless combinations of variables such as gradients, fluxes, etc. measured at the same height can be expressed as universal functions of the stability parameter (z/Λ), where Λ is the local Obukhov length. Before proceeding to the objective of the Chapter, a brief discussion on local similarity theory based on turbulence statistics is presented in the next section.

3.2 Local scaling

The local scaling hypothesis states that the dimensionless combinations of all turbulence quantities measured/computed at the same measuring heights, z can be expressed as universal functions of stability parameter, $\zeta = z/\Lambda$. The general form of the relationship is given by Pahlow et al. [82] for a flat terrain based on dimensional analysis as

$$\frac{\sigma_i}{u_*} = A + B\left(\frac{z}{\Lambda}\right)^C \tag{3.1}$$

Where, $i = u, v, w$ and A, B and C are empirical constants. The theory and the functional relations hold good for neutral, and slightly stable regimes of the atmosphere as tested by many researchers [77, 168]. However, investigation under the highly stable regime was not promising. The curve fit of sonic anemometer data for normalized turbulence variables [70, 82, 169–171] showed that the curve of σ_i/u_* is almost constant up to $\zeta = 1$. The curve turns upwards and steeply rises, for high ζ values. This upward shift in the curve indicates that the normalized turbulence quantities continue to increase and leads to more scatter under highly stable conditions. This trend is partly due to the intermittency of turbulence that occurs during highly stable conditions [172, 173]. Additionally, the observations are sensitive to meandering [61], gravity wave motions, drainage flows, and surface heterogeneity. De Franceschi et al. [174] reported a list of turbulence relationships proposed by various authors. In the z-less regime, when Λ is very small, the turbulence in the surface layer is decoupled from the surface, as mentioned earlier. However, functional Eqn. 3.1 is still valid, if locally measured scaling parameters (at the same height, where wind and temperature are measured) are used [69]. However, when ζ becomes very large, even this local scaling seems to break down, giving way to buoyant oscillations due to gravity waves. Caughey [175] reported such oscillations in the wind frequency spectrum as waves with periods varying from a few minutes to an hour. Mahrt et al. [61] reported that reducing the averaging time eliminates the influence of non-turbulent motions such as gravity waves, etc. particularly under very stable conditions. However, the reduction in averaging time can introduce flux-sampling errors. To circumvent this problem, Howell and Sun [117] introduced the Multi-Resolution Decomposition (MRD) of the high-frequency data, to filter out non-turbulent submesoscale motions from the sonic anemometer data set, without compromising with errors in flux estimation. The Chapter handles two objectives. One is to establish turbulence diffusion relationships, with new coefficients, for the functional form given in Eqn. 3.1, for the normalized standard deviations of wind velocity components, and test their applicability under stable to highly stable conditions. Fast response sonic anemometer data collected from two different sites, i.e., a hilly site Cadarache, France in the mid-latitudes, and a flat tropical coastal site Kalpakkam, India, is used for this study. The second objective is to study the dispersion of pollutants by incorporating these turbulence diffusion relationships in a Lagrangian Particle Dispersion Model, FLEXPART-WRF [37]. As a case study, the gamma dose rate measured over the site Kalpakkam is used for comparison against the simulated dose rate using FLEXPART, with the new and the default (Hanna's) turbulence diffusion relationships. [1]

3.3 Methodology

3.3.1 Multi-resolution decomposition

This method was put forward by Howell and Mahrt [176]. This is a method for calculating fluxes based on the relation between scale dependence of fluxes and associated flux sampling errors from time series data. According to this method, if the data record has 2^I points, then the data record can be divided into two sub-records with 2^{I-1} points each. These sub-records can be divided further until a sub-record contains individual datum [177].

[1] Rakesh, P.T., Venkatesan, R., Roubin, P., Srinivas, C.V., Baskaran, R. and Venkatraman, B., 2020. Formulation of turbulence diffusion relationships under stable atmospheric conditions and its effect on pollution dispersion. Meteorology and Atmospheric Physics, pp.1-16.

The covariance like vertical heat flux having a cut off scale of 2^i, starting from $(n-1)2^i$ to $n2^i-1$ is the average of the product of deviations, in the case, the vertical heat flux, w' and θ' from their associated means, averaged over 2^i points. The equation is given by

$$\overline{w'\theta'_n}\left(2^i\right) = \frac{1}{2^i}\sum_{j=(n-1)2^i}^{n2^i-1}\left[w_j - \overline{w_n}\right]\left[\theta_j - \overline{\theta_n}\left(2^i\right)\right] \tag{3.2}$$

The associated means are as follows

$$\bar{C}_n\left(2^i\right) = \frac{1}{2^i}\sum_{j=(n-1)2^m}^{n2^i-1} C_j \tag{3.3}$$

Where C is any variable. A data record having 2^I points will have 2^{I-i} sub-records for the estimation of fluxes. Each sub-record has a cut off scale of 2^i points. For example, the vertical heat flux having a cut off scale 2^i over the whole data record is computed by

$$F_\theta\left(2^i\right) = \frac{1}{2^{I-i}}\sum_{n=1}^{2^{I-i}}\overline{w'\theta'_n}\left(2^i\right) \tag{3.4}$$

The corresponding variance over the whole set of data points is given by

$$\sigma^2_{F\theta}\left(2^i\right) = \frac{1}{2^{I-i}}\sum_{n=1}^{2^{I-i}}\left[\overline{w'\theta'_n}\left(2^i\right) - F_\theta\left(2^i\right)\right]^2 \tag{3.5}$$

Assuming that 2^{I-i} values of fluxes having cut off scale of 2^i over the 2^I data points, are random and following Student's t distribution, then an estimate of the random flux sampling error over the data record is equal to

$$e_\theta\left(2^i\right) = \frac{t\left(2^{I-i},\alpha\right).\sigma_{F\theta}\left(2^i\right)}{\sqrt{2^{I-i}}} \tag{3.6}$$

Where α is a constant parameter. This parameter is determined such that the probability that the true record averaged heat flux falling within the interval $[F_\theta - e_\theta, F_\theta - e_\theta]$ is $2\alpha - 1$ [117]. Assuming a confidence level of 90%, for a large number of samples (> 30), the Student's t distribution converges to a normal distribution and the value of $t(2^{I-i},\alpha)$ is approximately 1.3 if the confidence level is 90% i.e., $(1-\alpha)$ from the t table.

3.3.2 Model configuration

This study employs a LPDM, FLEXPART-WRF that uses Hanna's semi-empirical parameterization for relating the turbulent statistics with boundary layer scaling parameters for simulation of pollutant trajectories. FLEXPART model uses the WRF model predicted meteorological data for simulating the pollutant dispersion.

3.3.2.1 Configuration of WRF and FLEXPART

The description of the WRF model is already given in Chapter 2. The present study uses WRF in a nested configuration of five domains over Cadarache region with a grid size ratio of 1:3:3:3:3 (Fig. 3.1).

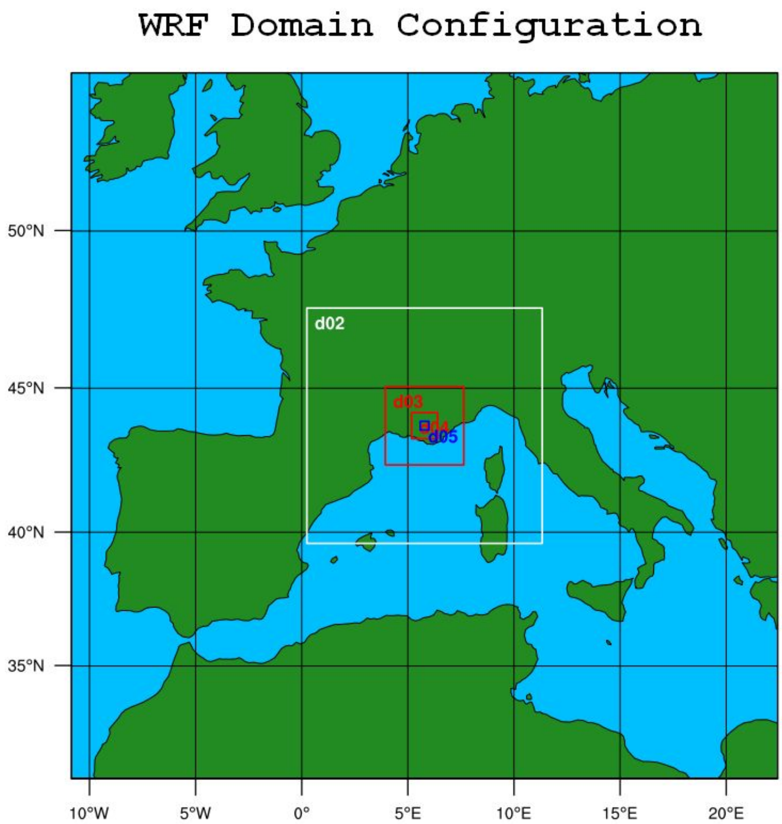

Figure 3.1 – WRF simulation domain

The grid resolution of the master domain is 27 km, and that of the innermost domain is 0.333 km. Every domain has 100X100 grid cells. The WRF model uses terrain data from USGS, and land use from MODIS. The model employs the MYJ scheme [135] for boundary layer diffusion and Janjic Eta Monin–Obukhov for surface layer scheme. The model uses the Dudhia scheme for shortwave radiation, and rapid radiative transfer model (RRTM) for longwave radiation. WRF Single-Moment 6-Class (WSM6) microphysics and the NOAH land surface scheme are other configurations used in the model. For the cumulus option, the model uses the Grell scheme, for the 27 km domain. Each domain has 65 vertical layers, with the model top at 50 hPa. Configuration of the vertical levels is such that twenty levels are within the first 100 m, with the first model layer approximately 3 m above ground level. The model takes data from the NCEP GFS final (FNL) operational global analyses, for the initial and boundary conditions. FLEXPART-WRF is an LPDM for simulation of transport and diffusion of pollutants in the atmosphere. The theory employed in the model is already described in Chapter 2. The current study uses model averaging time of 60 min for the computation of concentration. One million pseudo particles are released for the whole simulation period for dispersion calculations. The time step of computation is small, and it is within the Lagrangian time scale for the detailed description of turbulence. By default, the model employs the Hanna scheme [1] for the computation of the average standard deviation of the wind velocity vector. The WRF model supplies inputs such as wind fields and other variables to FLEXPART every 5 min interval to reduce the temporal interpolation errors.

3.4 Site description and measurements

Fast response sonic anemometer data over flat terrain and complex terrain have been collected for a considerable period of a few days when the atmospheric condition is mostly stable. The study uses data from two sites with different terrain characteristics. One is a flat tropical station, Kalpakkam (12.57444^0 N, 80.17417^{0}E), situated in southern India, and the second is a hilly terrain, Cadarache (43.70^0 N, 5.73333^{0}E) in southeastern France. The meteorological sensors, its make etc. used in this study is given in Annexure-1.

3.4.1 Kalpakkam dataset (Case-I)

The Kalpakkam site is a coastal station and the site details are given in Chapter 2. Fast response measurements use a sonic anemometer (R.M Young make) mounted at the height of 10 m on a meteorological tower, situated about 1 km away from the coast. The tower (12.56397^0 N, 80.1274^0 E) is located on a terrain with an unobstructed fetch of 300-400 m in all directions, with no buildings and obstacles around. The data-sampling rate is 10 Hz. The present analysis uses data collected for ten stable nights during November 2013. The Sonic anemometer was operational during the period 12th November-22nd November 2013, and data is archived every 30 min. The analysis uses data collected after the sunset with positive ζ. During this period, the wind direction is predominantly northeast over this site. The site also has a 50 m meteorological tower with five levels of measurement of meteorological parameters such as wind speed, wind direction, humidity, and temperature. Fig. 3.2 shows the site map. The data are collected during clear sky days, free from synoptic disturbances.

Figure 3.2 – The site map of Kalpakkam. The red disc shows the location of the meteorological tower and sonic anemometer. The balloon with a star shows the locations of environmental radiation monitors.

3.4.2 Cadarache dataset (Case-II)

The Cadarache site in the French Alpine foothills is topographically complex, with hills and valleys of various sizes. The area around Cadarache is heterogeneous in land use, with some agricultural fields on the Durance riverbanks, forest or bush on the hills, and a 1.3

km^2 lake situated northwesterly from the site. The Durance Valley (DV) is 5 to 8 km wide, with an average depth of 200 m. The portion of the DV that lies between Sisteron and the Clue de Mirabeau is 67 km in length, with a mean slope angle of 0.2° along the valley axis ([178]). The valley is oriented about 30° North (Fig. 3.3a). At the Clue de Mirabeau, the valley width varies from 5 km to 200 m. The Cadarache Valley (CV) is along the SE-NW direction. The width of the valley is 6 km long, and the width is about 1 to 2 km, with a slope angle of 1.2° along the valley. Northeast of Cadarache is the Southern Alps, located around 70 km with a height of at least 1500 m m.s.l and up to 3000 m at a distance of 140 km.

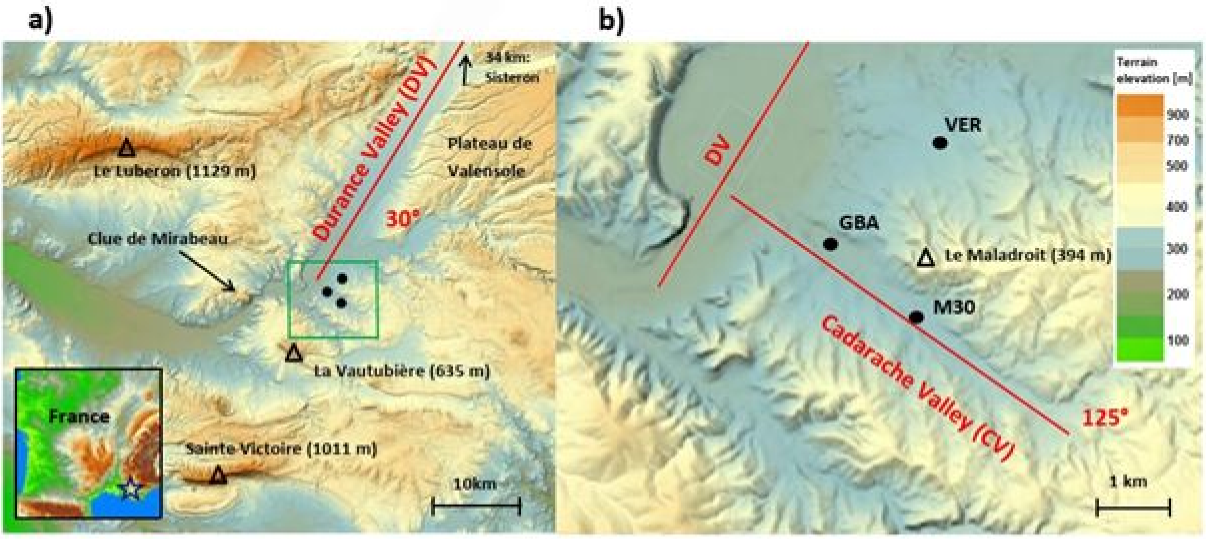

Figure 3.3 – a) provides study area in lower left frame, b) is the enlargement of the green rectangle in a). The red lines show the Durance (DV) and the Cadarache (CV) valleys, respectively. Black dots indicate the measurement locations. Courtesy: The Royal Meteorological Society (Duine et al., [178], Quarterly Journal of Royal Meteorological Society)

Two east-west orientated mountain ridges viz-a-viz the Luberon, and the Sainte Victoire are at a moderate distance from the site. Both have maximum heights of 1000-1100 m. The measurement location is a flat area with bushes in the south, and a few distant low buildings (1 or 2 storeys) in the north and northwest sector. The fetch is 400m along the small Cadarache valley axis and about 200 m crosswise the valley. The measuring mast is installed right in the middle of this open prairie. The nearest buildings are 120 m away from the measurement location. Like Mistral or summer sea breeze, the winds from north and northwest are generally associated with neutral to unstable conditions. Therefore, the analysis does not include the data recorded during the north and northwesterly winds. Data collected during an Intensive Observation Period (IOP) of the KAtabatic winds and Stability over Cadarache for the Dispersion of Effluents (KASCADE) experiment [178] is used. Concerning the purpose of the field measurement campaign, the most favorable weather conditions occur when clear skies are present, and when the influence of synoptic systems on the local wind field is weak. As it is very likely to have these conditions during the winter months in the region, it was decided to follow a negative warning concept, i.e., when low-pressure systems are in the vicinity or Mistral will occur; the planned IOP's will not be conducted. The study uses the data from sonic anemometer (R.M. Young make) collected at 10 m above ground level, for a few stable nights, with clear sky in February 2013 (10 February to 20 February), free from synoptic disturbance. The sampling rate is 10 Hz. The site also has a sonic anemometer mounted at the height of 2 m above ground level. The Stable Boundary Layer (SBL) height varies between 13-27 m during this period. The SBL height is estimated using the formulations listed in Zilitinkevich [179].

The location of the sonic anemometer is shown as M30 (43.68550^{o}N, 5.76169^{o}E) in Fig. 3.3b. The data covers a wide range of stable atmospheric conditions, including highly stable conditions with a ζ value of 10. The raw data is archived every 30 min. Each night contains varying hours of stable conditions. Further, Tether Sonde (TS) observations available during the period February 17 to February 19, 2013, were used for vertical profile comparison of simulated wind speed and wind direction, using WRF. The maximum height of TS achieved was 250 m above ground level during this period. The location of the TS is close to M30, 100 m up valley.

3.4.3 Data analysis

The data used for the study are quality checked. Visual inspection of the data is performed to check the presence of spikes by plotting the time series data. The data is de-trended, and the coordinate system is aligned with respect to the streamline direction by double rotation and tilt correction. Under the highly stable condition, to avoid the inadvertent capture of non-turbulent motions in the calculation of standard deviation of wind velocity components [61, 70, 81], the averaging time is chosen based on the multi-resolution decomposing method. The analysis considers only data points that comply with the Taylor hypothesis. Many researchers [180, 181] suggested that the Taylor hypothesis is valid when the turbulence intensity is smaller than the mean wind speed. This condition is satisfied by computing the turbulence intensity, σ_u/U and applying the criterion that the data with $\sigma_u/U < 0.5$ is rejected [82].

The various scaling parameters required for the computation of turbulence intensity in the framework of the local similarity theory are given below. The local Obukhov length is given by

$$\Lambda = \frac{-\tau^{3/2}T}{g\kappa\overline{w'T'}} \tag{3.7}$$

The expression for the shear stress (τ) is given by

$$\tau = \rho[\overline{u'w'}^2 + \overline{v'w'}^2] \tag{3.8}$$

where ρ is the air density, g is the acceleration due to gravity and T is the temperature. The prime quantities refer to the turbulence fluctuations about the mean. κ is the von Kàrmàn constant accepted as 0.4.

The normalized wind velocity standard deviations $\frac{\sigma_i}{u_*}$ where i refers to u, v, w and the stability parameter (z/Λ) (where z is the measurement height) are computed using the scaling variables u_* and Λ. Eqn 3.1 shows the profile relation for normalized components of wind velocity standard deviations for the stable condition based on the local similarity theory. The data are fitted using the method of Least Squares.

3.5 Results

3.5.1 Multi-resolution decomposition of Kalpakkam data

This analysis uses sonic anemometer data from ten stable nights. Fig. 3.4 shows the MRD spectrum following the algorithm, suggested by Howell and Sun [117] for heat and momentum flux. Here, ΔF is the change in flux of heat or momentum between adjacent cut-off scales, F is the flux of heat or momentum, and Δe is the flux error. The flux error, Δe is calculated by assuming that the heat flux, with different cut-off scale, follows Student's t-distribution. Fig. 3.4a as well as Fig. 3.4b indicates that above the cut-off scale of ≈ 15 min, the flux sampling error (Δe) is more than the change in fluxes (ΔF) between successive cut-off scales.

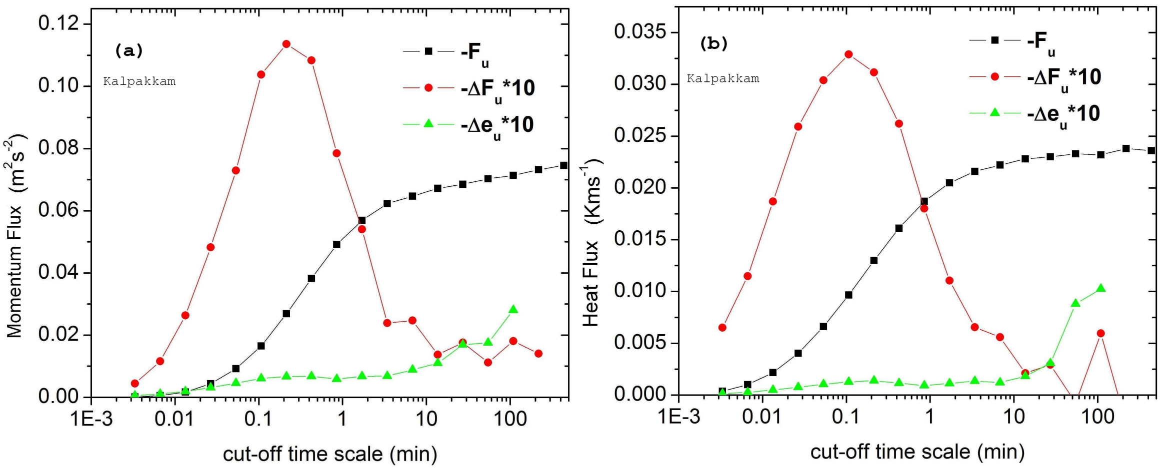

Figure 3.4 – The multi-resolution decomposition plot for (a) momentum (b) heat

In this case, it implies that choosing a time record length, spanning more than 15 min, will introduce errors in the flux estimates. Using this result as guidance and taking in to account the variations in the cut-off scale for different sub-records, 15 min is chosen as the time scale for each sub-record, for the estimation of fluxes. The cut-off scale is the record length of the data, that can be used for flux estimate with confidence, without any flux sampling errors. Further, the fluxes for each sub-record are estimated by finding the cut-off scale within each sub-record and averaging the fluxes for these sub-records. The cut-off scale, within each sub-record, is estimated at the point where $\Delta e < \Delta F$ in the flux-error curve, similar to Fig. 3.4. Different sub-records show different cut-off scale. The minimum cut-off scale was found to be ≈ 1 min for flux computation. The fluxes thus estimated, are used for the computation of the local Obukhov length, Λ and subsequently for estimation of shear stress. The shear stress and the Obukhov length are further used for estimating scaled standard deviations as a function of ζ. Fig. 3.5 shows the normalized standard deviation of horizontal and vertical components of the wind velocity, calculated with and without

MRD. The figure indicates that the scatter in the data of normalized turbulence components for stable conditions is less with the MRD over the one without MRD. Basu et al. [182] also obtained similar results. The figure also indicates that relationships without filtering show an increasing trend for $\zeta \approx 0.5$. Pahlow et al. [82] and Mahrt et al. [61] reported the constancy in the value of the horizontal wind component up to $\zeta \leq 1$.

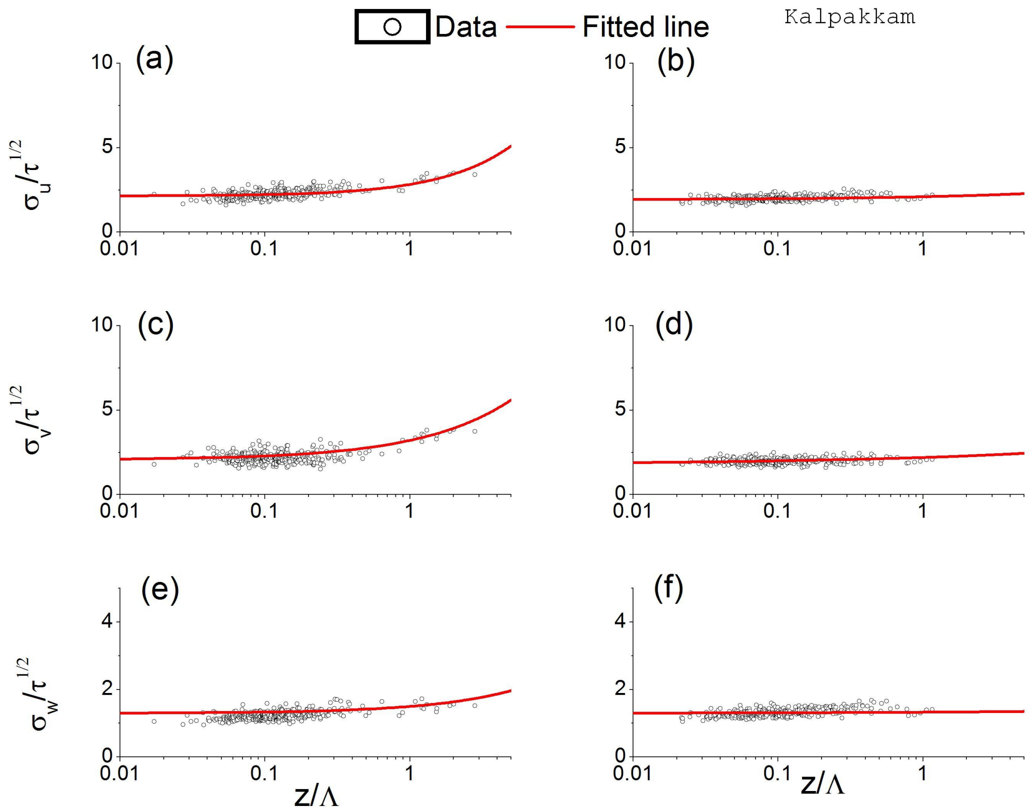

Figure 3.5 – The Normalized standard deviation of horizontal and vertical wind components without (left panel) and with (right panel) multi-resolution decomposition

Smedman [70] and Babic et al. [183] reported the constancy up to $\zeta < 0.5$. Similarly, De Franceschi et al. [174] reported the constancy up to $\zeta \approx 1$ after applying the appropriate filter. Many researchers [70, 82, 169, 170] reported the increase in the value of σ_i/u_* , for high ζ. A few studies in the tropical and coastal areas [80, 184, 185] also show an increase in the value of normalized turbulence quantities, under stable conditions. However, this increase in the value of σ_i/u_* is not conspicuous, after filtering out the non-turbulent motions from the data set, in this case by MRD. The figure indicates that the rise in the value of normalized turbulence quantities, with the MRD, is lesser at the highly stable regime than that estimated without MRD. Further, the figure shows that the number of data points is meager in near-neutral and neutral conditions. The lower number of data at near-neutral conditions is because, at Kalpakkam, the occurrences of near-neutral and neutral stability conditions are not frequent.

Extrapolation of the fitted curve (Fig. 3.5b, Fig. 3.5d, Fig. 3.5f) of normalized standard deviation against ζ, to neutral conditions, shows a value of 1.8±0.03, 1.9±0.06 and 1.1±0.04 for the empirical constant A, for normalized horizontal (u and v components) and vertical standard deviations respectively, with 95 % confidence level. Pahlow et al. [82] reported the constant A as 2.3, 2, and 1.1, respectively, for $u, v,$and w components of the normalized wind velocity standard deviations. Similarly, Smedman [70] reported the constant A as 2.3, 1.7, respectively, for u and v-velocity standard deviations. Further, Panofsky and Dutton [186] reported this value as 2.4 and 1.9, respectively, for u and v-velocity standard deviations. De Franceschi et al. [174] reported this value for along-valley wind as 1.92±0.02 and 1.71±0.02, for u-component and v-component of the standard deviations and 1.32±0.01, for w-component of the standard deviation. Similarly, for cross valley winds, they reported these values to be 1.90±0.09, 1.89±0.08 and 1.38±0.05, for u, v, and w component of the standard deviations. Babic et al. [183] reported these values for different heights over industrial town Kutina in Croatia, under wintertime nocturnal conditions. Our estimates of the constant B for horizontal and vertical components of turbulence are 0.4, 0.2, and 0.4, respectively, with a 95 % confidence level. The value of C is 0.3, for all the components. The increase in the value of normalized turbulence, for high ζ is not observed in this case, due to the filtering of non-turbulent motions. The constancy of the values of σ_i/u_* , at the stable regime, indicates that the relationships derived for the Kalpakkam site, follow local similarity theory, under stable atmospheric conditions. The next section discusses the results of a similar analysis carried out for the Cadarache data.

3.5.2 Results from Cadarache dataset

Similar multi-resolution decomposition to the Cadarache data shows the cut-off time scale as 10 min instead of 15 min as the case of the Kalpakkam site (Fig. 3.6). Analysis of different data records for the Cadarache region shows a minimum cut-off scale of $\approx$ 1 min, similar to Kalpakkam. Fig. 3.7 shows the normalized standard deviations, with and without multi-resolution decomposition.

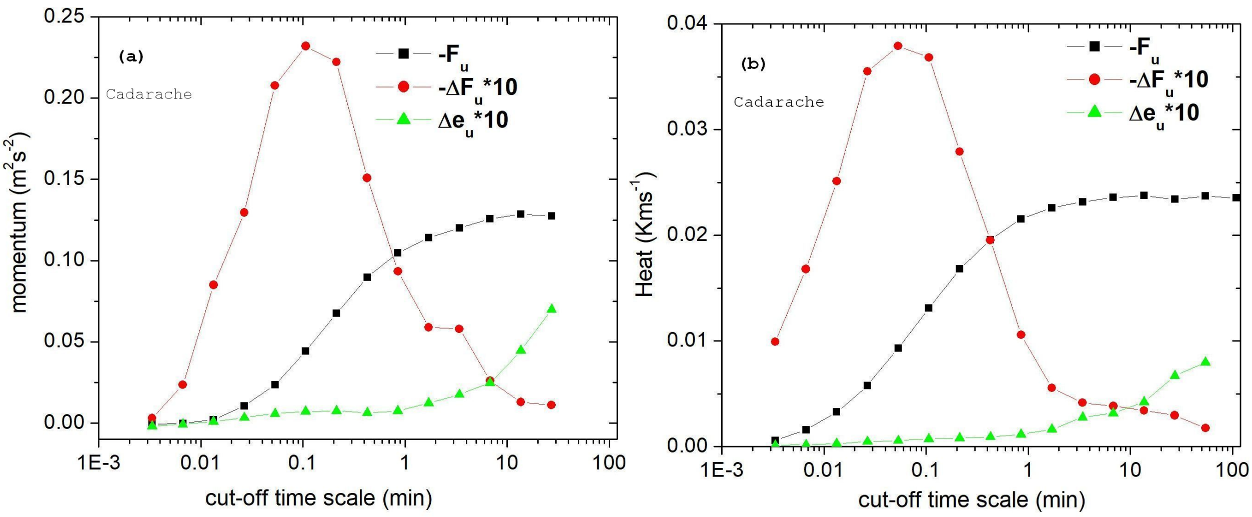

Figure 3.6 – The multi-resolution decomposition plot for (a) momentum and (b) heat

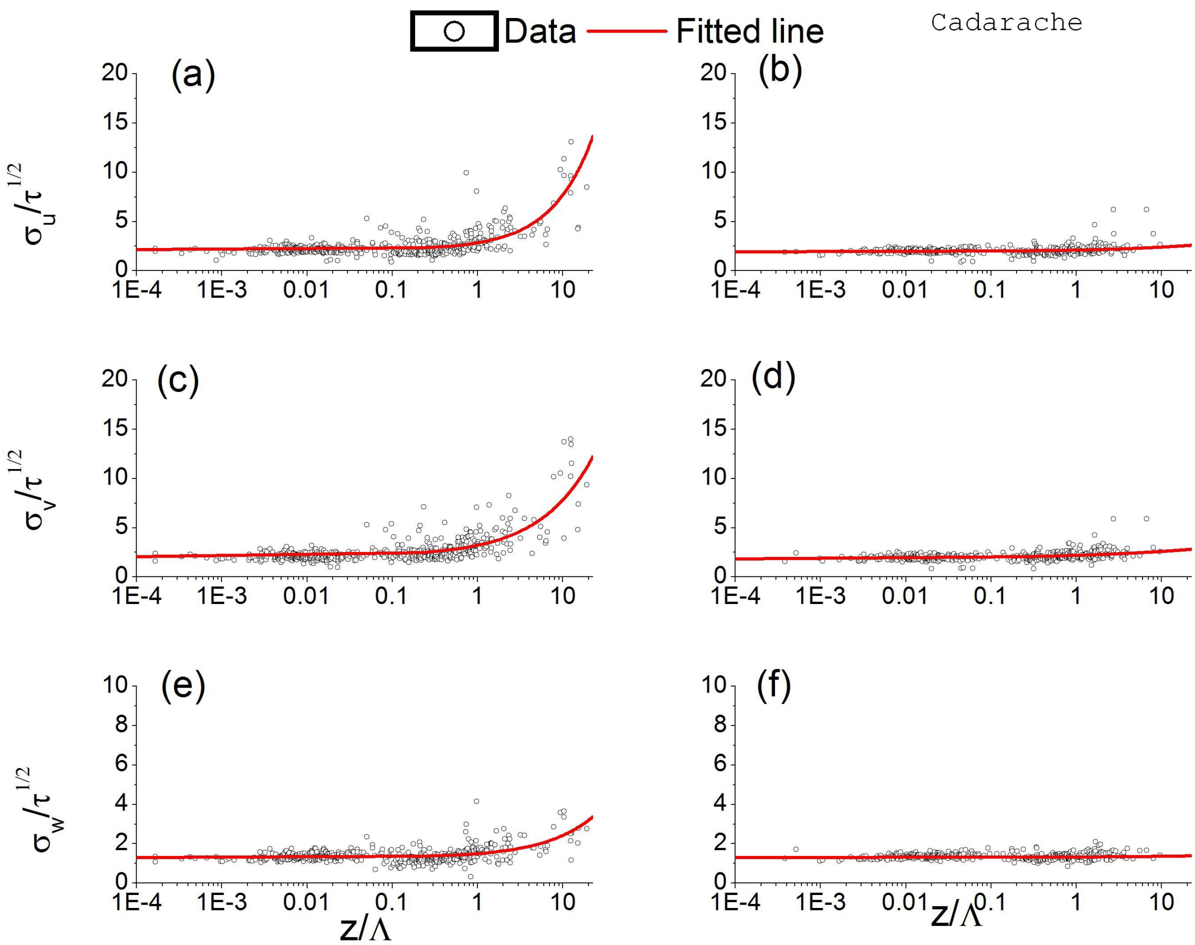

Figure 3.7 – The Normalized standard deviation of horizontal and vertical wind without (left panel) and with (right panel) multi-resolution decomposition

The Fig. 3.7 indicates that without MRD, more scatter is observed in the value of the normalized components, and shows an upward trend in the curve for $\zeta > 1$ (Fig. 3.7a, Fig. 3.7c, Fig. 3.7e). The rise in the curve (left panel), for higher values of ζ, shows the influence of the non-turbulent motions, on the normalized standard deviations of wind velocity. The figure also conveys that the slope of the curve in the left panel is higher than the slope noticed in the case of Kalpakkam data. On the other hand, the values of normalized standard deviations did not show such scatter and upward trend after filtering of the non-turbulent motions. The extrapolation of the fitted curve of values of normalized standard deviations (Fig. 3.7b, Fig. 3.7d, Fig. 3.7f) to neutral conditions shows a value of 1.9±0.07, 1.8±0.06 and 1.3±0.02 for the constant A for horizontal and vertical components respectively, with 95 % confidence level, which is closer (less than 10 %) to the values obtained for the Kalpakkam dataset, except for the vertical component (less than 20%). Many researchers [61, 82, 169, 183] analyzed the w-component of wind velocity standard deviation. In a review of turbulence statistics, Dias et al. [187] reported the value of A from several works and mentioned that it centers around 1.3. Similarly, for the constant B, the curve fit shows a value of 0.2, 0.3, and 0.03, respectively, for horizontal and vertical turbulence intensities, with a 95 % confidence level. The value of C is 0.4 for longitudinal and vertical components, and 0.3 for crosswind components. Table 3.1 summarizes the empirical formulation for normalized wind velocity standard deviations obtained from both sites.

Table 3.1 – Normalized wind velocity standard deviations under stable conditions

Site	U direction	V direction	W direction
Cadarache	$1.9+0.2\left(\frac{z}{L}\right)^{0.4}$	$1.8+0.3\left(\frac{z}{L}\right)^{0.3}$	$1.3+0.03\left(\frac{z}{L}\right)^{0.4}$
Kalpakkam	$1.8+0.4\left(\frac{z}{L}\right)^{0.3}$	$1.9+0.2\left(\frac{z}{L}\right)^{0.3}$	$1.1+0.4\left(\frac{z}{L}\right)^{0.3}$

3.5.3 Results of FLEXPART simulation over Cadarache

The new turbulence diffusion formulations obtained for the Cadarache site is incorporated in the FLEXPART model, to study the effect of new functional relationships on dispersion. As already mentioned, the WRF provides inputs for the FLEXPART model. The WRF is initialized at 1200 GMT on 17 February 2013, during one of the Intensive Obervation Period (IOP) and integration is continued until 1200 GMT on 19 February 2013. The FLEXPART simulation assumes a ground-level release with a release rate of 1 Bq/s. The main inputs to FLEXPART are three components of the wind velocity and the surface layer scaling parameters (u_*, L, mixed layer height). The wind speed and direction simulated by the WRF, are compared with observations at 10 m above ground level, starting from 1200 GMT 17 February 2013 for 48 hours and is shown in Fig. 3.8.

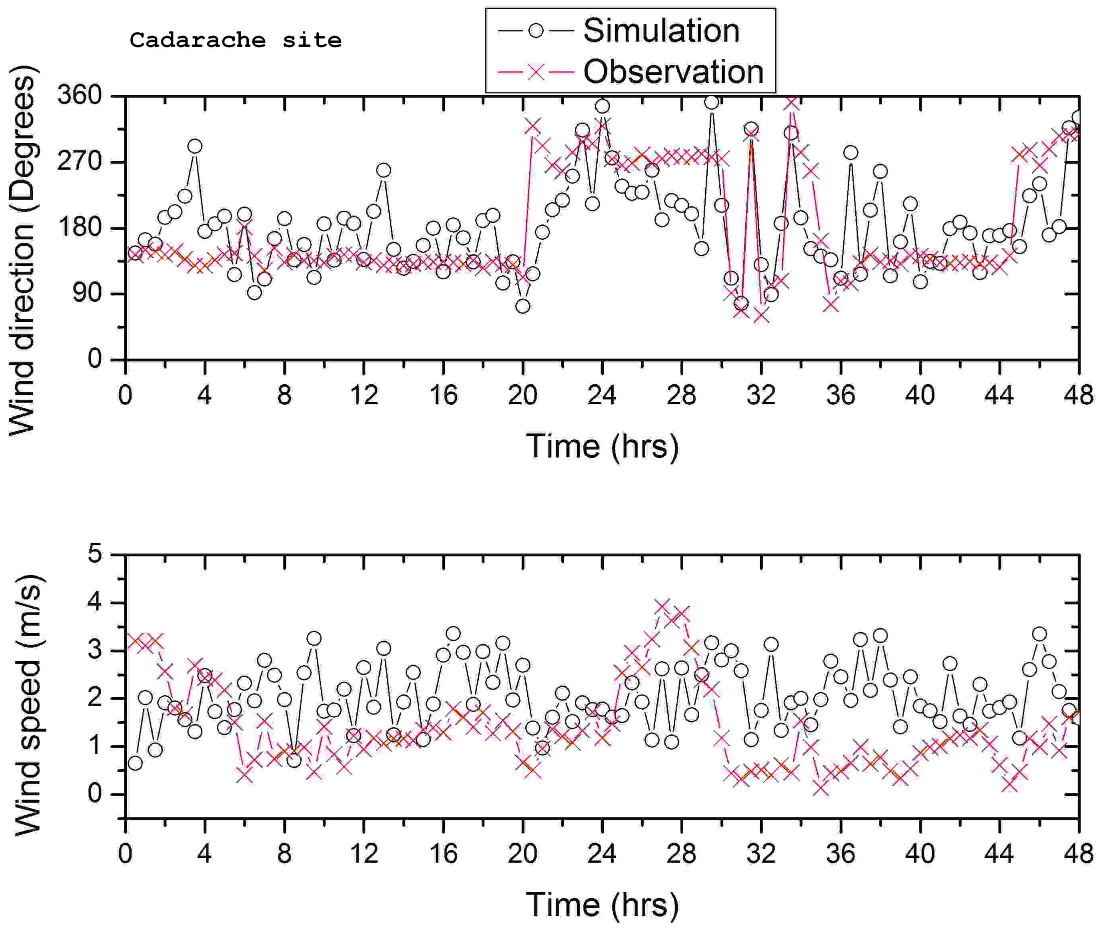

Figure 3.8 – Comparison of simulated wind speed and wind direction at 10 m AGL with observation M30 (43.68550°N, 5.76169°E)

The Root Mean Square Error (RMSE) for wind speed is 1.35 m/s, and for the wind direction, it is 61.5^0. The high value of RMSE is also reported by others as well [188], especially under low wind speed. Moreover, at very low wind speeds, the observed wind directions are not very reliable [189]. Further, Fig. 3.9a, Fig. 3.9b, Fig. 3.9c, Fig. 3.9d show the comparison plot of the simulated vertical profiles of wind speed and wind direction with tether sonde observation, available during the IOP at 1600 GMT on 18 February 2013, 2000 GMT on 18 February 2013, 0800 GMT on 19 February 2013 and 2000 GMT on 19 February 2013, respectively. The simulated vertical profiles at both the times are in good agreement with observation. The estimated RMSE for wind direction and wind speed are 21.71^0, 1.35 m/s, 13.77^0, 0.47 m/s, 42.64^0, 1.02 m/s and 23.82^0, 1.25 for Fig. 3.9a, Fig. 3.9b, Fig. 3.9c, and Fig. 3.9d, respectively. Further, for dispersion simulation, the FLEXPART model is initialized at 1800 GMT on 18 February 2013 and integrated till 1200 GMT on 19 February 2013 so that the simulation covers the stable atmospheric conditions.

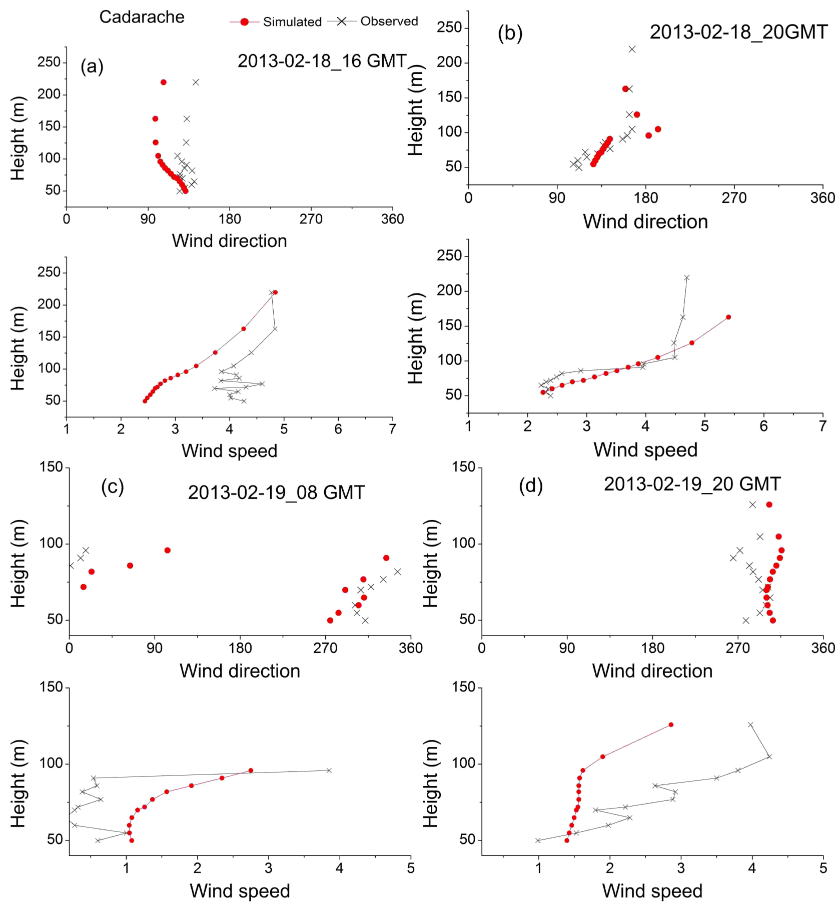

Figure 3.9 – Comparison of the vertical profile of wind speed and wind direction at (a) 1600 GMT on 18th February 2013 (b)at 0700 GMT on 19thFebruary 2013

The study further compares the gamma dose rate simulated by FLEXPART, using the new relationships (Table 3.1) and the model default Hanna‘s method [1]. The model uses the point kernel method [190–192], for gamma dose rate computation. The similarity relationships for normalized wind velocity standard deviations formulated by Hanna, for stable conditions are recalled below.

$$\sigma_u = 2u_* \left(1 - \frac{z}{h}\right) \tag{3.9}$$

$$\sigma_v = 1.3u_* \left(1 - \frac{z}{h}\right) \tag{3.10}$$

$$\sigma_w = \sigma_v \tag{3.11}$$

Here, h is the boundary layer height. Fig. 3.10 shows the color-shaded maps of factor variation in dose rate ($dose_{new\ scheme}/dose_{Hanna}$) at two consecutive hour at night (2300 GMT and 0000 GMT) under highly stable atmospheric conditions.

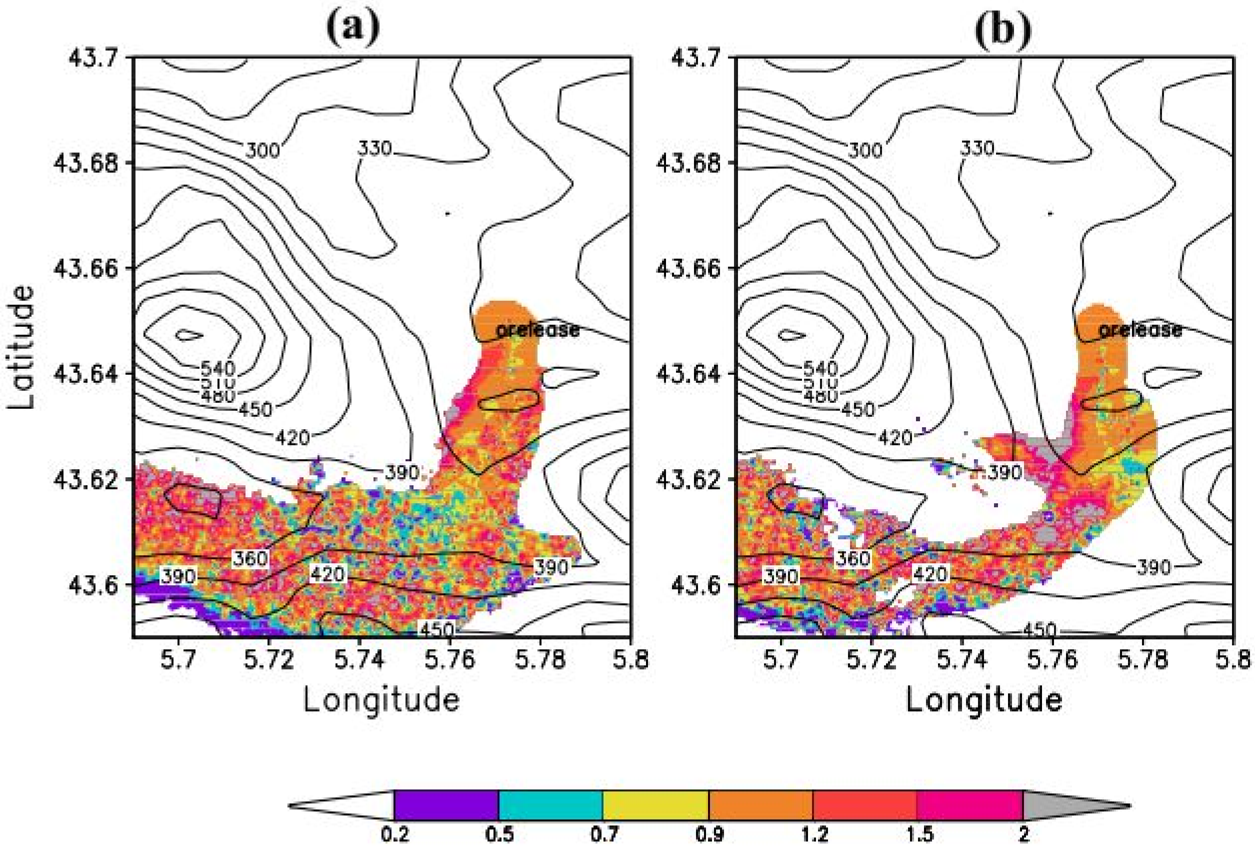

Figure 3.10 – The factor variation ($dose_{new\ scheme}/dose_{Hanna}$) in dose rate at 2300 GMT and 0000 GMT. The contour refers to the topographic height.

The analysis time corresponds to an atmospheric condition with positive values of ζ. The left panel shows the dose rate with the new scheme relative to the default Hanna's scheme at 2300 GMT, and the right panel shows the same, but at 0000 GMT. From the figure, it is evident that the new scheme simulates a higher dose rate relative to the model default scheme. Spatially, the dose rate, with the new scheme, shows a variation between a factor of 1.2-2 relative to Hanna's scheme. Moreover, the figure also shows that the relative dose rate is lower, 0.2-0.5, especially at the lateral boundary of the plume. i.e., the dose rate simulated using Hanna's scheme is higher than the dose rate simulated with the new method. This lower relative dose is because Hanna's scheme simulates higher diffusive velocity, and hence more dispersion and broader plume. On the other hand, the new scheme simulates less dispersion and narrower plume, thereby leading to a lower relative dose rate at the boundary of the plume. Seaman et al. [188] reported that high-resolution simulation using weather models like WRF could simulate submesoscale motions, only to some extent. However, in dispersion calculations, it is required to use the turbulent diffusion relationships free from such motions, for a conservative estimate of dispersion, especially while using high-resolution weather models like WRF. Otherwise, it leads to the accounting of such motions twice in dispersion estimates, thereby underestimating the pollutant concentration. This problem is especially crucial in radioactivity dispersion since the regulatory limits for nuclear power plant releases are fixed based on the simulated dose calculations using these types of dispersion models coupled with weather models. For the validation of the above dispersion calculations, no experimental tracer concentration data are available at this site, Cadarache. However, at Kalpakkam, the plume gamma dose rate is monitored using a network of AGDL around the Madras Atomic Power Station (MAPS). The plant (MAPS) releases trace quantities of radioactive Argon gas under normal operating conditions, from a 100 m stack. The dose rate data collected using AGDLs used further for comparison with the simulated plume dose rate, and the next section discusses these results.

3.5.4 Modification of FLEXPART for short-range dispersion

For short-range dispersion applications, the FLEXPART is modified to directly use the observed meteorological data from a local 50 m meteorological tower in place of the WRF forecast meteorological fields. The meteorological data is averaged over 1 hr and supplied to FLEXPART. In FLEXPART, the turbulence parameters such as wind velocity standard deviation and Lagrangian time scales are computed by the similarity method as already mentioned. The crucial inputs needed to compute these parameters by similarity method are the mixing height (h), the friction velocity (u_*), heat flux, Obukhov length (L) the convective velocity scale (w_*), the Coriolis parameter (f). In this study, these variables are computed using the profile method [193] by taking wind speed and temperature data at two levels (2 m and 50 m) from the tower. The flux-profile relationships for wind and temperature expressed as a function of non-dimensional stability function z/L [76] are solved to obtain friction velocity and temperature scale (θ_*). Initially assuming a Large value for L and minimum values for u_* and θ_*, new value for L is calculated, and the procedure is iteratively repeated until the difference between successive values converges to a minimum. The procedure gives heat, momentum fluxes, etc. This is the default method used in FLEXPART for largescale air pollution transport applications using global meteorological model data. The same is adopted here using local tower observations for better representation of local meteorological conditions. Since the modified version of the model is used for short-range of 20 km, the wind field is assumed to be horizontally uniform. Wind velocity data is interpolated to the particle position at every time step in the model. Above 50 m height, the wind is extrapolated to the reference height using the power-law velocity profile as there is no measurement available above 50m. The exponent is chosen depending on the values of the stability parameter. The mixed layer height [194] is estimated by following the relation,

$$h = \frac{\kappa u_* L}{f} \tag{3.12}$$

f is the Coriolis parameter and κ is the von Kàrmàn constant. For unstable conditions, during the daytime,the mixed layer height is capped at 500 m if computed values exceed this value based on observational studies at Kalpakkam [195]. During unstable conditions, the convective velocity required for the computation of Lagrangian time scale and wind velocity standard deviation is computed by

$$w_* = \left[\frac{\overline{w'\theta'}gh}{\theta_* C_p} \right]^{1/3} \tag{3.13}$$

C_p is the specific heat at constant pressure for air and θ_* is the temperature scale. The next section discusses the simulation of plume gamma dose with modified FLEXPART and comparison with observed gamma dose using AGDL.

3.5.5 Comparison of simulated dose over Kalpakkam with AGDL

The site Kalpakkam has a network of AGDLs mounted at 1 m above ground level in each wind direction sector of 22.5^o width. The detectors are arranged in a two-ring fashion, one ring of 500 m radius from the release point (MAPS), and the other ring of 1500m radius. There are a total of 27 monitors around the release point. Fig. 3.2 shows the pictorial representation of sampler locations. The AGDLs record the gamma dose rate (nGy/h) due to normal operational releases from the reactor, using Geiger Muller counters. The details of the releases and the AGDL network is available in Srinivas et al. [192]. The AGDLs record the gamma dose due to normal releases from the power plant. The background radiation dose at a particular detector location is estimated when the radiation plume is not over that particular detector. The recorded dose rate by the detector is the total dose rate due to the natural background and the argon releases from the reactor. The actual dose due to releases from the power plant is obtained by subtracting the background at AGDL location, from the total dose rate registered in the AGDL.

The current study uses the gamma dose rate data collected during November 2016. During this period, the wind direction is predominantly northeast, and the impact of the radioactive plume is over the land. Further, during the nighttime, the atmospheric stability ranges from Pasquill class “E” to “F” over this region. The present analysis uses 65 hours of data of gamma dose rate collected under stable atmospheric conditions. For the simulation of dose rates and further comparison with measured dose rates, the FLEXPART model uses input data from the meteorological tower for dispersion estimates. When the argon plume passes over the detector, the detector shows a spike in the time series data of the dose rate. As the wind is from the northeast, the detectors in the southwest sector show the increase in dose rate. Two detectors of the network captured the radioactive plume for the flow direction during these hours as the rest were away from the primary impacted sector. Fig. 3.11. shows the correlation plot of the observed gamma dose rate against simulated values, with the new and Hanna's method of computing wind velocity standard deviations.

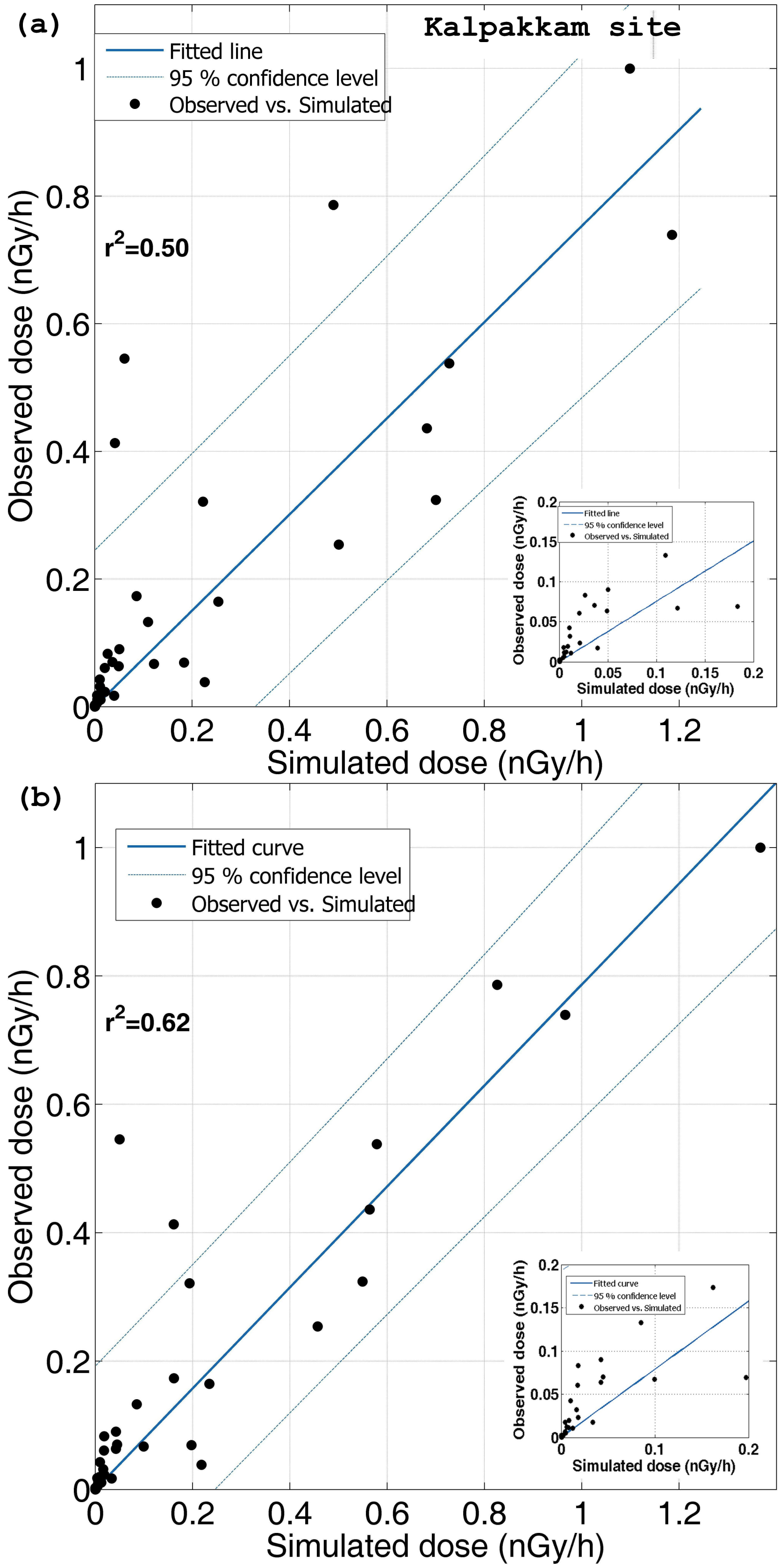

Figure 3.11 – Comparison of observed and simulated gamma dose using (a) Hanna's method (b) new method for turbulence diffusivity under stable atmospheric conditions. The graph in the inset is for the zoomed range of 0-0.2 nGy/h.

Both the observed as well as simulated dose rate values are normalized with the observed maximum dose rate. The figure indicates that the incorporation of the new relationships for turbulent intensities for stable atmospheric conditions in FLEXPART produces better results for the dose rate estimates compared to the model with default Hanna's method. Table 3.2 shows the error statistics such as Fractional Bias (FB), Normalized Mean Square Error (NMSE), Geometric Mean (MG), Factor of two (FAC2) and Geometric Mean Variance (VG). The error matric is computed as follows.

$$FB = 2 \times \left(\frac{\overline{C}_o - \overline{C}_p}{\overline{C}_o - \overline{C}_p} \right) \tag{3.14}$$

$$NMSE = \frac{\overline{(C_o - C_p)^2}}{\overline{C}_o \overline{C}_p} \tag{3.15}$$

$$MG = exp\left(\overline{ln(C_o)} - \overline{ln(C_p)} \right) \tag{3.16}$$

$$VG = exp\overline{[ln(C_o) - ln(C_p)]^2} \tag{3.17}$$

$C_o$and C_p are the observed and predicted values.

Table.3.2 indicates that the new schemes perform better compared to the default scheme. Though the turbulence coefficients in the corresponding relationships are different, the difference is not very evident in the dose estimates because of fewer data in the highly stable regime over Kalpakkam.

Table 3.2 – Error statistics

Error	Hanna scheme	New scheme
FB	-0.06	-0.06
NMSE	1.18	0.77
MG	1.70	1.60
VG	3.40	3.10
FAC2	0.37	0.51
R^2	0.50	0.62

It is challenging to get the data with coincidence of highly stable conditions and the radioactive plume centerline over the detectors, that are rare. For better statistics, it is necessary to analyze dose records under more events of stable conditions. Nevertheless, the present study indicates an improvement in dispersion estimates under highly stable atmospheric conditions.

3.6 Conclusion

The study described in this Chapter shows that under stable conditions, the normalized standard deviation of the wind components follow local similarity theory if non-turbulent motions are filtered. The study also indicates that the values of the empirical coefficients vary within 10 %, in the case of horizontal wind and $\approx 20\%$ in vertical wind velocity standard deviations, for the flat terrain of Kalpakkam and the hilly complex Cadarache terrain, considered for the study. The study used multi-resolution decomposition to filter the non-turbulent motions from the fast response measurements. The simulation with new turbulence diffusion relationships in the FLEXPART model indicates that the simulated gamma dose rates are improved compared to the model default Hanna's method. The results also show that new turbulence relationships predict narrower plume and higher dose rate compared to the Hanna scheme under stable atmospheric conditions. At Kalpakkam site, the measured dose rate data from two detectors could only be used as they matched the requirement of the meteorological condition though it is inadequate for arriving at a statistically robust conclusion. Nevertheless, the study indicates that the new relationships show promising results in simulating the dispersion under highly stable conditions. Moreover, the study also shows that under stable conditions, the radiological dose is more than that expected under similar conditions employing conventional methods.

Chapter 4

Dispersion under low wind speed

This chapter gives an overview of dispersion under low wind speed. The chapter enunciates the use of modified Gaussian and Lagrangian models under low wind speed conditions. Moreover, a comparison of simulated concentration and crosswind plume spread is presented using the open database of the Hanford-67 tracer release experiment[1].

4.1 Introduction

Atmospheric dispersion models are used to assess air quality over industrial complexes and radiological doses in the case of nuclear power plants. These models use several atmospheric parameters as inputs, which play a crucial role in deciding the fate of the released substances. It is shown by Hongwei et al. [84] that calm conditions and low wind speeds have a profound influence on dilution factors. Under low wind speed conditions, the plume meandering will be predominant. As the wind speed decreases, the complexity of the boundary layer increases, which affects the dispersion. Therefore, the dispersion study under weak wind conditions is critical [92] for air pollution/radiological impact assessment. Joeng et al. [196] compared tracer experiment data with the Gaussian plume model results under low wind speed conditions. They reported that the measured concentrations are lower than those simulated by the model. This overestimation by the model may be

[1] *Rakesh, P.T., Venkatesan, R., Srinivas, C.V., Baskaran, R. and Venkatraman, B., 2019. Performance evaluation of modified Gaussian and Lagrangian models under low wind speed: A case study. Annals of Nuclear Energy, 133, pp.562-567.*

due to meandering conditions prevailing under low wind speed, which is not reflected in the model. In the past, different modeling procedures have been adopted to deal with low winds based on K-theory and Gaussian approaches [92, 94, 197] and Lagrangian particle models [105, 115, 197]. Oettl et al. [105] proposed a Lagrangian stochastic model useful under low wind speed, in which the time step is chosen randomly from a uniform distribution [104]. In their study, a negative auto-correlation parameter is used for the horizontal wind components. The negative correlation parameter is chosen based on the computed Eulerian auto-correlation functions (EAF), from one year of sonic anemometer observations in Graz, Austria. The result of the study was that the auto-correlation exhibits a negative lobe (as shown in Chapter 1) rather than exponential. It is attributed to the meander, which is absent in the vertical wind component. The negative lobe in the auto-correlation function is also reported by many in the past [87, 105, 106, 108, 198]. A brief review of the past research conducted under low wind speed is given in Chapter 1. In this study the Gaussian model with modified dispersion parameters [87] and a coupled Langevin equation based LPDM [115] together with standard Gaussian and Lagrangian model is used to compute the crosswind spread under low wind speed conditions. These models take into account the aspects mentioned above of the auto-correlation function. The results are compared with data available from the Hanford diffusion experiment [199].

4.2 Theory

Two modeling approaches are employed in this study, and they are (i) Gaussian plume model and (ii) LPDM.

4.2.1 Gaussian Model

In order to use the Gaussian model under low wind speed, modification suggested by Frenkiel [106] on the dispersion parameter is employed. The theory is briefly discussed below. In general, in atmospheric dispersion models, the auto-correlation of the horizontal wind component exhibits an exponential fall [200]. It is written as

$$R(\tau) = exp\left(\frac{-\tau}{T}\right) \tag{4.1}$$

$R(\tau)$ is the auto-correlation coefficient, τ is the lag, and T is the Lagrangian time scale. Based on the above assumption, the crosswind variance using Eqn. 1.7 can be written as

$$\sigma_y^2(t) = 2\overline{v'^2}\left[tT - T^2\left(1 - exp\left(\frac{-\tau}{T}\right)\right)\right] \tag{4.2}$$

Where $\sigma_y^2(t)$ is the crosswind variance of the plume, v' is the fluctuation of the wind velocity vector in the y-direction, and t is the travel time. As already mentioned in the introduction, the exponential fall of the auto-correlation function is not a good assumption under low wind speed. In order to represent the auto-correlation under low wind speeds following two expressions are considered.

$$R(\tau) = exp\left(-\frac{\tau}{T_m}\right)\left(cos\left(\frac{\tau}{T_n}\right) - \frac{T_n}{T_m}sin\left(\frac{\tau}{T_n}\right)\right) \tag{4.3}$$

Proposed by Csanady [198] and

$$R(\tau) = exp\left(-\frac{\tau}{(m^2+1)T_3}\right)cos\left(\frac{m\tau}{(m^2+1)T_3}\right) \tag{4.4}$$

Suggested by Frenkiel [106] and Murgatroyd [107]. T_m and T_n represent the time scales for fully developed turbulence and the oscillatory component, respectively and m, a non-dimensional quantity that controls the meandering oscillation frequency. T_3 is the time scale for a fully developed turbulence. One example data set that shows a negative lobe under low wind speed is shown in the Fig. 4.1. Please note that under higher wind speed conditions, the exponential nature of the auto-correlation is still valid.

Eqn. 4.4 can be rewritten as

$$R(\tau) = exp(-p\tau)cos(-q\tau) \tag{4.5}$$

With

$$p = \frac{1}{(m^2+1)T_3} \tag{4.6}$$

and

$$q = \frac{m}{(m^2+1)T_3} \tag{4.7}$$

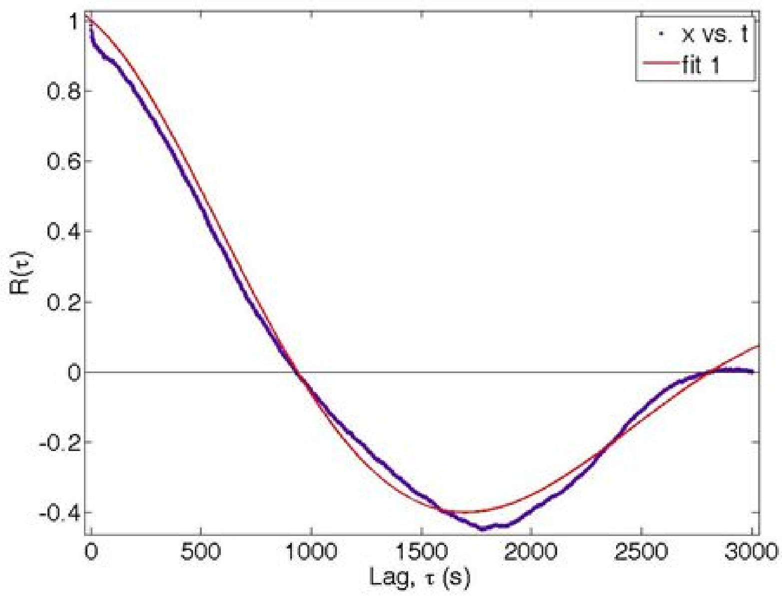

Figure 4.1 – The auto-correlogram for crosswind components of wind under low wind speed

Here p and q are hybrid parameters expressed in terms of T_3 (time scale for a fully developed turbulence) and m. Using Eqn. 4.3 the variance is written as

$$\sigma_y^2(t) = 2\sigma_v^2 \frac{T_m^2 T_n^2}{T_m^2 + T_n^2}\left[1 - exp\left(\frac{-\tau}{T_m}\right)\left(cos\left(\frac{t}{T_n}\right) + \frac{T_n}{T_m} sin\left(\frac{t}{T_n}\right)\right)\right] \tag{4.8}$$

And using Eqn. 4.4 it is

$$\sigma_y^2(t) = \frac{2\sigma_v^2\left\{pt(p^2+q^2) + (q^2-p^2) - exp(-pt)\left[(q^2-p^2)cos(qt) + 2pqsin(qt)\right]\right\}}{(p^2+q^2)^2} \tag{4.9}$$

Anfossi et al. [87] suggested that Frenkiel [106] or equivalently Murgatroyd [107] is the most preferable one. In this study, the expression by Frenkiel [106] in the form suggested by

Murgatroyd [107] (Eqn. 4.5) is used in the Gaussian plume model. For practical purposes, the values for the parameters m and T_3 are calculated by the empirical formulation suggested by Oettl and Anfossi [111] as given below:

$$m = \frac{8.5}{(1+U)^2} \tag{4.10}$$

and

$$T_3 = \frac{mT_*}{2\pi(m^2+1)} \tag{4.11}$$

$$T_* = 200m + 500 \tag{4.12}$$

Here T_* is the meandering period, and U is the average wind speed at the release height. It is to be noted that the value of m determines the deviation of crosswind spread and resulting crosswind concentration from the Gaussian plume model with standard PG dispersion parameters. Fig. 4.2 shows the deviation of normalized centerline concentration values from the Gaussian model with PG dispersion parameters, for different values of m.

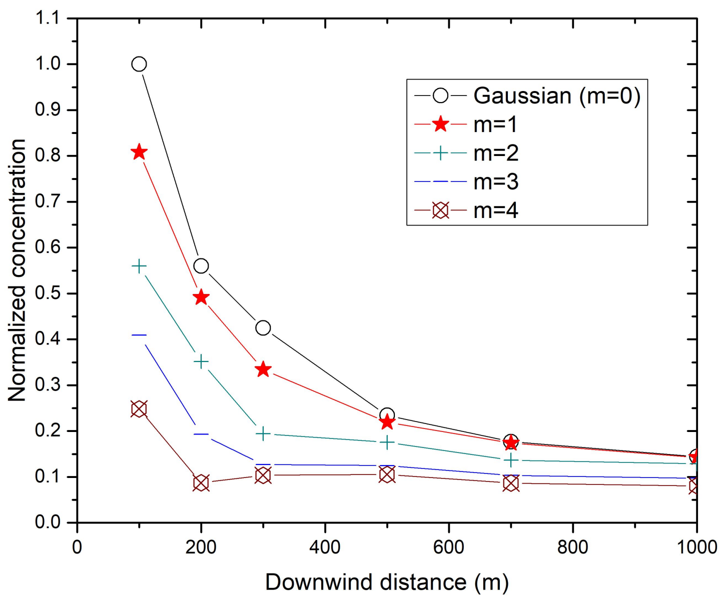

Figure 4.2 – The deviation of normalized concentration from the standard Gaussian model for different values of m

The PG dispersion parameters are computed based on Eimutis et al. [201]. The simulation with standard PG dispersion parameters shows relatively high centerline concentration due to the non-accounting of meandering conditions. Further, the normalized crosswind concentration with standard and modified Gaussian model for a release rate of 1 Bq/s from 30 m above ground level is shown in Fig. 4.3. In the above case of crosswind concentration comparison, the stability condition is selected to be Pasquill stability class "A".

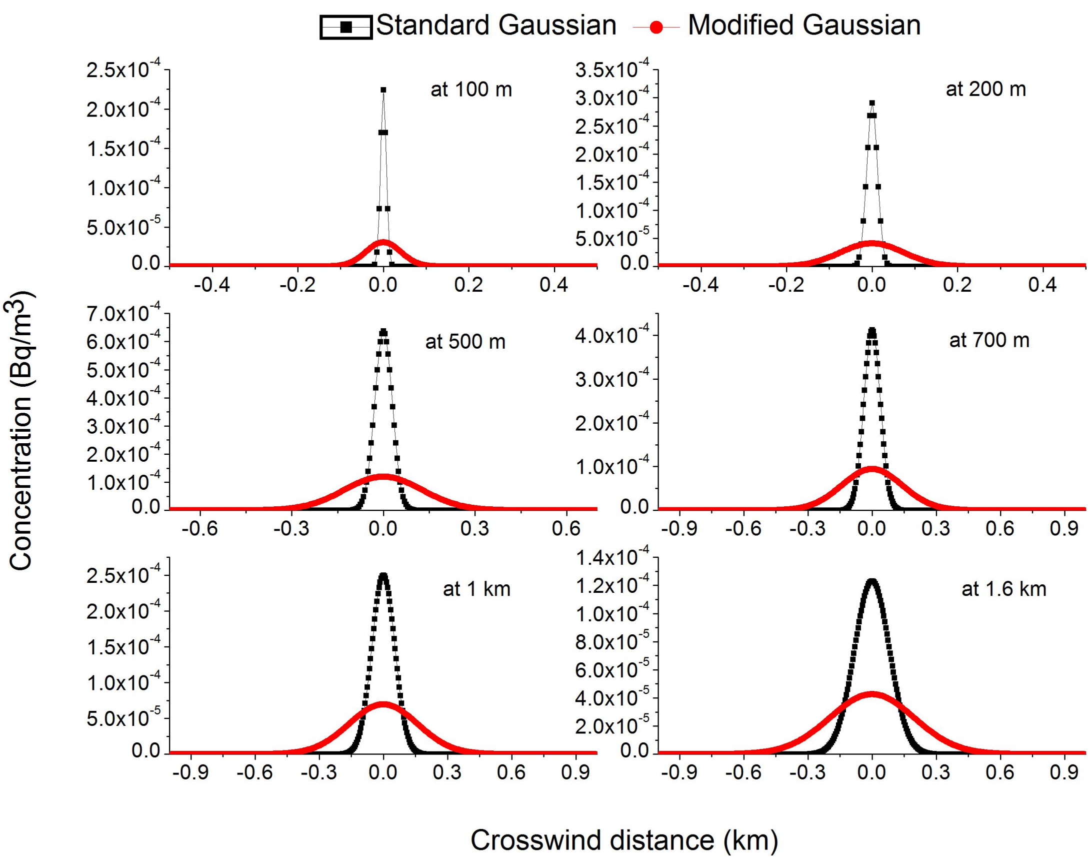

Figure 4.3 – The comparison of crosswind concentration profile between standard and modified Gaussian model for Pasquill category A

The wind speed (2 m/s) and wind direction standard deviation corresponding to this stability class, A [1, 202] is taken as a reference for calculation of dispersion parameters. It is to be noted that centerline concentration reduced by a factor of ≈ 5 compared to the standard Gaussian model when the meandering is accounted for in the Gaussian model. This factor is in agreement with the reduction reported by Kristensen et al. [90]. Though the centerline concentration is reduced, it is noted that the plume is spreading into a larger area than envisaged by the standard Gaussian model. The next section discusses the use of this modified Gaussian model with improved dispersion parameters and a coupled Lagrangian particle model to compare the simulated concentration with tracer dispersion data collected during the Hanford experiments.

4.2.2 Lagrangian model

The standard Langevin equation is given in Chapter 2. On the other hand, the improved Lagrangian Particle Dispersion model under low wind speed condition employs a coupled Langevin equation suggested by Anfossi et al. [115]. It has the following form

$$du' = (pu' + qv')dt + \sigma_u \sqrt{2pdt}\zeta_u \tag{4.13}$$

$$dv' = -(-qu' + pv')dt + \sigma_v \sqrt{2pdt}\zeta_v \tag{4.14}$$

Here, du' and dv' are incremental components of the turbulent component of the wind velocity. p and q are the same as that of Eqn. 4.6 and Eqn. 4.7. σ_u and σ_v are the standard deviations of wind velocity along-wind and crosswind directions, respectively. ξ_i is the Gaussian random number with zero mean and variance unity ($i = u, v$). The standard deviation of the crosswind component of the wind velocity is computed using the wind direction standard deviation (σ_θ) because of the lack of fast response measurements during the experiment considered in the study. The formulation is given by Cirillo et al. [12] as,

$$\sigma_v = U\sigma_\theta \tag{4.15}$$

where σ_θ is in radians.

The standard deviation of the along-wind component of the wind velocity under stable conditions is computed based on Hanna [1] as

$$\sigma_u = 1.54\sigma_v \tag{4.16}$$

This system of equations, together with conventional Langevin equation, is applied to sonic anemometer data collected over Kalpakkam in a year. The simulated dispersion pattern by two methods i) five minute averaged wind with Hanna scheme of estimating standard deviation (Eqn. 4.16) together with conventional Langevin equation and ii) with new coupled Langevin equations (Eqn. 4.13 and Eqn. 4.14) is shown in Fig. 4.4. it is seen from the study that the coupled Langevin equation shows more spread compared to the conventional Langevin equation. To further validate the performance of the coupled Langevin equation, tracer experiment data available during the Hanford experiment is used. The details of the experiments and further analysis are presented in the subsequent sections.

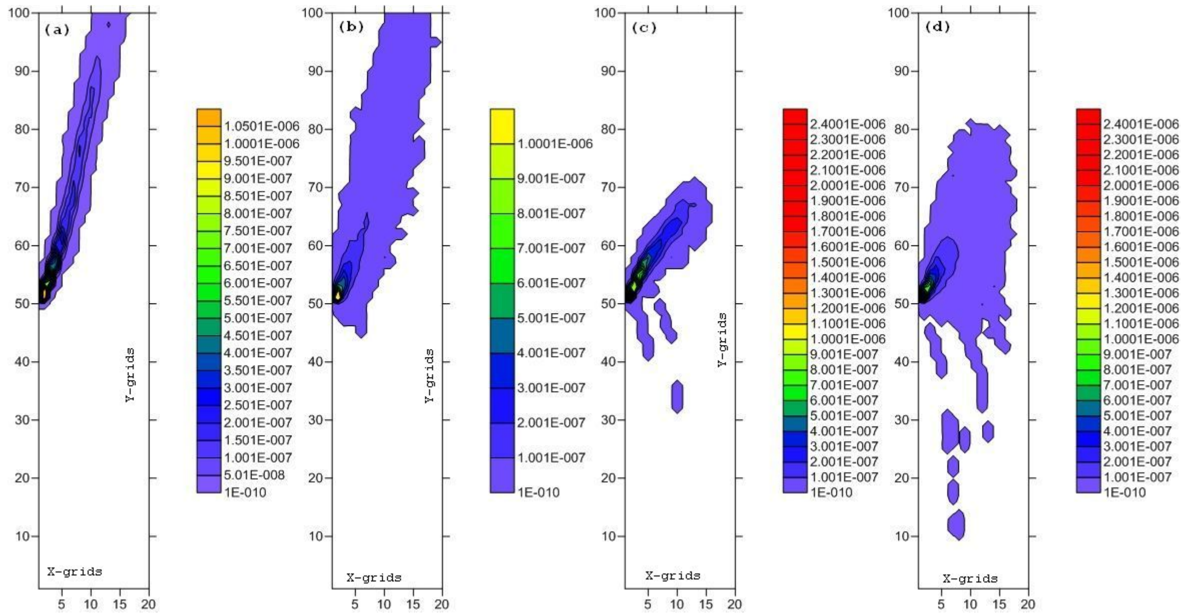

Figure 4.4 – The ground level concentration pattern with Hanna‘s method (a, c) and modified method (b,d). Each grid is 10 m in size.

4.3 Details of the experiment

A series of tracer experiments were conducted at the Hanford site (46.56667^{o}N, 119.6^{o}W) during the 1967-1968 periods. A detailed description of the Hanford experiment is provided by Nickola [199]. The site description and details of meteorological measurements can also be found in Sandeepan et al. [68]. Zinc sulfide (ZnS) was used as the tracer and was released continuously in a shallow broad valley under stable nighttime conditions from a height of 2 m above ground level for 30 min. The samples were collected on membrane filters mounted 1.5 m above the surface. We consider two cases where the low wind speed was observed for the present study. Filters were distributed in a few arcs downwind at distances of 200 m, 800 m, 1600 m, and 3200 m for the experiment D1 and 200 m and 800 m for experiment

C1. Each arc encompasses a sector of approximately 90 degrees. The comprehensive experimental data sets for various experiments are available online from https://www.harmo.org/jsirwin/H67Discussion.html. The present study uses the tracer data of experiments D1 (Case I) and C1 (Case II). The wind speed and wind direction standard deviation observed at the release height of 2 m above ground level during experiment D1 is 1.2 m/s and $\approx$ 15.9 degrees respectively. For C1, the corresponding values were 1.4 m/s and $\approx$ 8 degrees respectively. During both the experiments, the atmospheric stability parameter was estimated to be Pasquill class “E”.

4.4 Results

Subsequent subsections discuss the results of concentration simulation with the models and comparison with dispersion data from Hanford experiments.

4.4.1 Case-I (D1-experiment)

4.4.1.1 Using Gaussian model

In this case, the Gaussian model with standard Pasquill-Gifford (PG) dispersion parameters is initially used to compute the crosswind plume standard deviation. As already mentioned in section 4.3, the atmospheric stability class during Case-I is estimated as Pasquill class "E". Since horizontal homogeneity of wind field cannot be expected at far downwind distances, especially under meandering conditions, the study is limited to the first arc measurements at 200 m. The crosswind plume standard deviation is estimated by computing 2σ about the centerline concentration value where σ is the standard deviation of the plume spread. The analysis shows that at 200 m, the Gaussian model with standard PG dispersion parameters shows a crosswind standard deviation of 26 m. Whereas, the observed crosswind plume standard deviation is 76 m. It indicates that the Gaussian model with standard PG dispersion parameters for stability class ’E’ simulated less dispersion and underestimated the plume standard deviation by a factor of $\approx$ 3. Subsequently, the PG dispersion parameters are replaced by the hybrid parameters and other variables. These variables are computed based on Eqn. 4.6, Eqn. 4.7 and Eqn. 4.10 to Eqn. 4.12 and they are given in

Table.4.1

Table 4.1 – The list of values of the variables used to compute modified dispersion parameters in Case-I

Variable	Value
m	≈ 2
T_3	58
T_*	851
p	0.004
q	0.007

The crosswind plume standard deviation is now simulated using the modified dispersion parameter as input to the Gaussian model. The result of this simulation gives a value of 109 m as the plume standard deviation at 200 m against the observed standard deviation of 76 m. It indicates that the simulation with modified dispersion parameters overestimated the plume standard deviation by a factor of ≈ 1.4. However, it is better than a factor of 3 underestimations by the standard PG dispersion parameters. Fig. 4.5 shows the normalized concentration profiles at 200 m downwind by both methods together with observation.

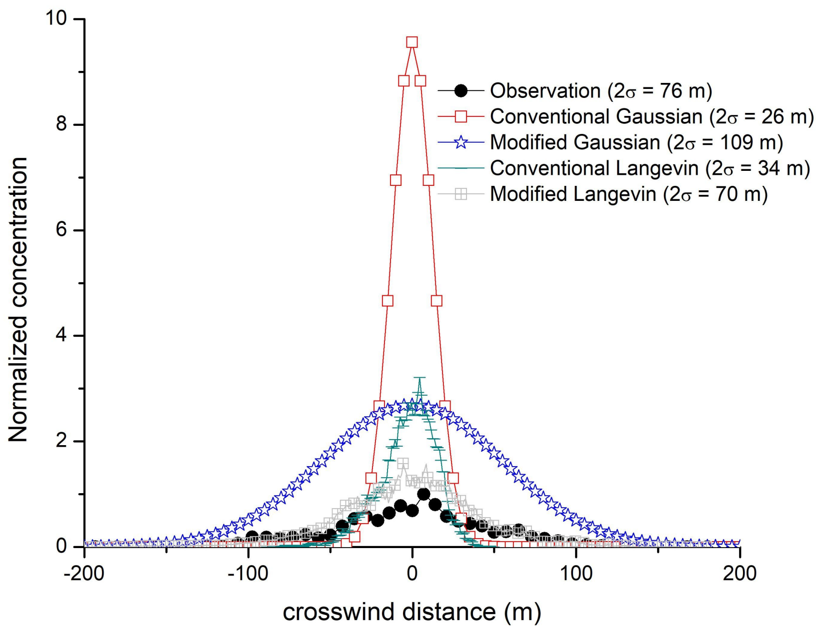

Figure 4.5 – The crosswind concentration profiles with various methods against observation for Case-I

Fig. 4.5 shows that the concentration normalized with peak observed concentration (hereafter normalized peak concentration) by the Gaussian model with standard PG dispersion parameter overestimated the normalized peak concentration by a factor of ≈ 9 compared to observed peak concentration. On the other hand, the Gaussian model with modified dispersion parameters overestimated the normalized peak concentration by a factor of 2.7 relative to the observed peak. Though the Gaussian model with modified dispersion parameters show a higher crosswind standard deviation, it overestimated the observed concentration. The overestimation may be due to the lesser vertical spread relative to the observed spread during the experiment.

4.4.1.2 Using LPDM

This simulation uses standard Langevin equation as well as coupled Langevin equation with LPDM for simulating the crosswind plume standard deviation. In this case, the crosswind and along-wind standard deviations are computed using Eqn. 4.15 and Eqn. 4.16 respectively. Since the atmospheric stability is "E" (stable conditions), based on Hanna [1], the vertical wind velocity standard deviation numerically equals to crosswind velocity standard deviation. It is to be noted that meandering has no influence on the auto-correlation in the vertical direction [105]. The estimated crosswind plume standard deviation at 200 m using LPDM with standard Langevin equation is 34 m, which is in close agreement with the prediction by the Gaussian model with standard PG dispersion parameters. However, both of them underestimated the crosswind plume standard deviation by a factor of ≈ 2.2. On the other hand, the LPDM with coupled Langevin equation simulated the plume standard deviation as 70 m, which is in close agreement with the observed standard deviation of 76 m. The crosswind normalized concentration profiles at 200 m downwind simulated with various methods against observation is shown in Fig. 4.5. The LPDM with standard Langevin equation overestimated the normalized peak concentration by a factor of 3.2 relative to the observed concentration. On the other hand, LPDM with coupled Langevin equation simulated the normalized peak concentration close to observation but still by a factor of 1.6.

4.4.2 Case-II (C1 experiment)

Similar to Case-I, numerical experiments are repeated for Case-II. The Pasquill stability conditions in Case-II is estimated to be "E". In Case-II also the comparison is restricted to

200 m to satisfy the homogenous assumption.

4.4.2.1 Using Gaussian model

The simulation with the Gaussian model with standard PG dispersion parameters gives an estimate of crosswind plume standard deviation similar to Case-I, which is 26 m because the atmospheric stability is the same as that of Case-I. The observed crosswind plume standard deviation is 48 m. This indicates that the standard Gaussian model underestimated the crosswind plume standard deviation by a factor of ≈ 1.8. It is also to be noted that this factor is less than that of Case-I, which is ≈ 3. This difference is because the wind direction standard deviation observed at release height in Case-II (8^0) is less than Case-I (15.9^0), and therefore, the meandering is not predominant in Case-II compared to Case-I. On the other hand, the Gaussian model with the modified dispersion parameter simulated the plume standard deviation as 63 m, which is an overestimate by a factor of ≈ 1.3. Table 4.2 shows the values of hybrid parameters and other variables required for the computation of the modified dispersion parameters. Fig. 4.6 shows the crosswind normalized concentration profiles using both the methods at 200 m downwind together with observation.

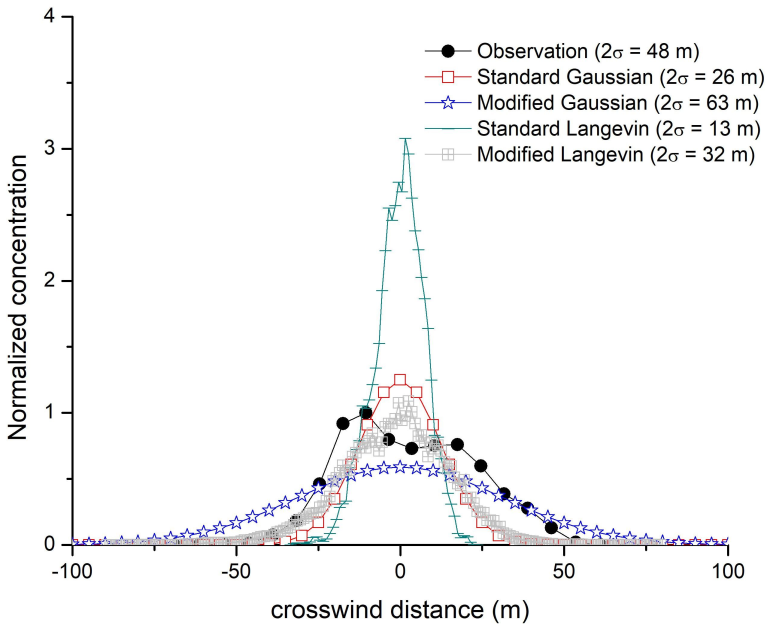

Figure 4.6 – The crosswind normalized concentration profiles with various methods against observation for Case-II

Fig. 4.6 shows that the normalized concentration simulated by the Gaussian model with standard PG dispersion parameters was overestimated by a factor of 1.9 with respect to the observed concentration. Similarly, the Gaussian model with improved dispersion parameters underestimated the concentration by a factor of 0.6 with respect to the observed concentration.

Table 4.2 – The list of values of the variables used to compute modified dispersion parameters in Case-II

Variable	Value
m	≈ 1
T_3	58
T_*	795
p	0.005
q	0.007

4.4.2.2 Using LPDM

Similar numerical experiments are performed using LPDM with standard and coupled Langevin equation for Case-II. The LPDM with standard Langevin equation estimated the crosswind plume standard deviation at 200 m to be 13 m, which is ≈ 3.7 times lesser than the observed value of 48 m. In this case, the Gaussian model with standard PG dispersion parameters predicted the plume standard deviation better than LPDM with standard Langevin equation. Similarly, the LPDM with coupled Langevin equation predicted the plume standard deviation to be 32 m, which is again ≈ 1.5 times lesser than the observed plume standard deviation (48 m) but better than that predicted by LPDM with standard Langevin equation. The crosswind normalized concentration profiles at 200 m downwind with various methods against observation is shown in Fig. 4.6. As already mentioned, meandering motions are not very active in the Case-II experiment, as it is evident from the wind direction standard deviation during the experiment period. Fig. 4.6 shows that the LPDM with standard Langevin equation overestimated the normalized peak concentration by a factor of ≈ 3.0 relative to observed peak concentration. On the other hand, the simulation using LPDM with coupled Langevin equation overestimated the simulated normalized peak concentration by a factor ≈ 1.1 with respect to the observed peak. Table 4.3 shows the measured and simulated crosswind plume standard deviation for both the cases.

Table 4.3 – Summary of simulated and observed plume standard deviation for Case-I and Case-II

Experiment	Observed $2\sigma_y$ at 200 m	Simulated $2\sigma_y$ using GPM	Simulated $2\sigma_y$ with improved dispersion parameter in the GPM	Simulated $2\sigma_y$with LPDM with standard Langevin equation	Simulated $2\sigma_y$ with LPDM with coupled Langevin equation
Case-I (D1)	76 m	26 m	109 m	34 m	70 m
Case-II (C1)	48 m	26 m	63 m	13 m	32 m

Thus the LPDM with coupled Langevin equation and Gaussian model with modified dispersion parameters are useful under low wind speed with meandering though latter overestimated the crosswind plume standard deviation for the cases analyzed.

4.5 Conclusion

Two cases of dispersion experiments from Hanford-67 have been analyzed by incorporating developments in dispersion parameters for low wind conditions. It is seen from the study that under low wind speed conditions, the standard Gaussian model with new dispersion factors or Lagrangian model with coupled Langevin equation can be used to simulate dispersion more realistically. Due to scarcity of dispersion experimental data under low wind speed conditions, a rigorous evaluation of the modified models could not be performed. However, this is a rare study of comparing the experimental data with the modified schemes of dispersion parameters for low wind speed. The overestimation by the standard Gaussian model is preferable in the case of accidents as it is conservative [203]. However, for estimating the impact of routine releases under the normal operating condition of a plant, a realistic approach, as described in this Chapter is preferable for estimating plant design parameters such as stack height, containment, etc.

Chapter 5

Dispersion under calm wind conditions

This Chapter describes the development of a LPDM for short range and transient release scenarios. The model uses different methods for estimating turbulence diffusion, such as similarity theory, from the Pasquill-Gifford stability curve and direct measurements using ultrasonic anemometer data. The Chapter also describes the dispersion under calm episodes that prevail at sites like Kalpakkam and the performance of different diffusion schemes in estimating dispersion and resultant plume gamma dose under calm conditions.

5.1 Introduction

The dispersion of activity in the atmosphere needs to be analyzed to evaluate the radiation dose to the public due to normal or accidental releases of radioactivity from nuclear power plants. For the estimation of radiological dose, it is important to have a dispersion model, source inventory and meteorological data as inputs to the model. When the wind speed is very low and dispersion is weak, it is difficult to assess the concentration spread unless the radiation detectors are densely installed around the facility. Since conditions such as calm wind speeds are rare, the number of radiation detectors are optimized. Under these circumstances, a suitable dispersion model is essential though it may have inherent uncertainties. The uncertainties arise from the assumption of the model equations and the accuracy of the inputs that are fed to the model. However, it can provide an overview of the radiation dose in the surrounding areas of nuclear facilities in case of an accidental release under calm wind speed conditions. The estimates of the atmospheric dilution factors calculated using the dispersion model are used to assess the radiation dose. Low wind speed and calm atmospheric conditions have a significant impact on the atmospheric dilution factors [84]. In literary terms, the calm condition refers to a state in which the wind speed is zero, but conventionally it is taken as the lower limit of the measurement sensor. In the atmospheric dispersion scenario, a calm condition is a state where the wind speed is below a 0.5 m/s [1, 85].

In this Chapter a wind speed less than 1 m/s is assumed as calm. Wind speed is one of the crucial parameters which decides the degree of dispersion and the dilution of the pollutant concentration and it is inversely related to it. Apart from calm conditions, low wind speeds are considered critical in dealing with turbulence and atmospheric dispersion [87] and it has been dealt with in Chapter 4. In this Chapter, dispersion and resultant radiation dose especially plume gamma dose under average wind speed less than 1 m/s are studied using an in house developed LPDM. The model uses inputs from sonic anemometer and a cup anemometer from a 50 m meteorological tower. The simulated plume gamma dose is compared against dose simulated using the conventional Gaussian model. The theory employed in the dispersion model is discussed in the next section.

5.2 Outline of the theory

The model follows the conventional transport equation for computing the particle position and it is given in Chapter 2. The standard deviation of the wind velocity vector is computed by three different methods. One is the diffusion derived from sonic anemometer data (hereafter DDS), second is based on Hanna‘s scheme [1] (hereafter HSS) based on similarity approach and third is based on PG stability curve based on Pasquill [2] . The Lagrangian time scale is computed based on the similarity method. The first method uses the wind velocity standard deviation computed directly from sonic anemometer. In this method, the wind velocity standard deviations are computed using the well known relation given below.

$$\sigma_i = \sqrt{\frac{\sum(u_i - \bar{u}_i)^2}{N}} \tag{5.1}$$

σ_i $(i = u, v, w)$ is the wind velocity standard deviation, u_i is the instantaneous wind velocity and $\bar{u}_i$ is the average wind velocity and N is the number of samples.

The second method based on similarity theory is given below.

Under unstable conditions:

$$\frac{\sigma_u}{u_*} = \frac{\sigma_v}{u_*} = \left(12 + \frac{h}{2.|L|}\right)^{1/3} \tag{5.2}$$

$$\tau_{Lu} = \tau_{Lv} = 0.15\frac{h}{\sigma_u} \tag{5.3}$$

$$\sigma_w = \left[1.2w_*^2\left(1 - \frac{0.9z}{h}\right)\left(\frac{z}{h}\right)^{\frac{2}{3}} + \left(1.8 - \frac{1.4z}{h}\right)u_*^2\right]^{\frac{1}{2}} \tag{5.4}$$

For $z - z_0 > -L$

$$\tau_{Lw} = \frac{0.1z}{\left[\sigma_w\left(0.55 - \frac{0.38(z-z_0)}{L}\right)\right]} \tag{5.5}$$

For $\frac{z}{L} < 0.1$

$$\tau_{Lw} = 0.59\frac{z}{\sigma_w} \tag{5.6}$$

For $\frac{z}{L} > 0.1$

$$\tau_{Lw} = 0.15\frac{h}{\sigma_w}\left[1 - exp\left(-\frac{5z}{h}\right)\right] \tag{5.7}$$

Under neutral conditions:

$$\frac{\sigma_u}{u_*} = 2.0exp\left(-\frac{3fz}{u_*}\right) \tag{5.8}$$

$$\frac{\sigma_v}{u_*} = \frac{\sigma_w}{u_*} = 1.3exp\left(-\frac{2fz}{u_*}\right) \tag{5.9}$$

$$\tau_{Lu} = \tau_{Lv} = \tau_{Lw} = \frac{5\frac{z}{\sigma_w}}{1 + 15\frac{fz}{u_*}} \tag{5.10}$$

Stable conditions:

$$\frac{\sigma_u}{u_*} = 2.0\left(1 - \frac{z}{h}\right) \tag{5.11}$$

$$\frac{\sigma_v}{u_*} = \frac{\sigma_w}{u_*} = 1.3\left(1 - \frac{z}{h}\right) \tag{5.12}$$

$$\tau_{Lu} = 0.15.\frac{h}{\sigma_u}\left(\frac{z}{h}\right)^{0.5} \tag{5.13}$$

$$\tau_{Lv} = 0.15.\frac{h}{\sigma_v}\left(\frac{z}{h}\right)^{0.5} \tag{5.14}$$

$$\tau_{Lw} = 0.15.\frac{h}{\sigma_w}\left(\frac{z}{h}\right)^{0.5} \tag{5.15}$$

Here h is the mixing height, u_* is the friction velocity, w_* is the convective velocity scale, f is the coriolis parameter, z is the height from the ground and z_0 is the roughness height. τ_{Li} $(i = u, v, w)$ is the Lagrangian time scale. The third method based on Pasquill stability category is discussed below [204]. The particle position after a time $t + \Delta t$ is computed as

$$X(t + \triangle t) = X(t) + \bar{u}\triangle t + R_x \tag{5.16}$$

$$Y(t + \triangle t) = Y(t) + \bar{v}\triangle t + R_y \tag{5.17}$$

$$Z(t + \triangle t) = Z(t) + \bar{w}\triangle t + R_z \tag{5.18}$$

The turbulence diffusion R_x and R_y are calculated as

$$R_x = R_y = \sqrt{24K_i\triangle t}.(0.5 - R(0)) \tag{5.19}$$

where K_i ($i = x,y,\ z$) is the diffusion constant and $R(0)$ is the uniform random number between 0 and 1. K_i is computed as

$$K_i = \frac{1}{2}\frac{d\sigma_i^2}{dt} \tag{5.20}$$

Here σ_i^2 is the mean square displacement due to diffusion and can be estimated from Gifford [205]. The vertical turbulence diffusion is given by

$$R_z = \frac{\partial K_i}{\partial z}\triangle t + \sqrt{24K_i\triangle t}(0.5 - R(0)) \tag{5.21}$$

Model used in the study uses the empirical form $\sigma_i = a_i X^{b_i}$ [11]. Here a_i,b_i are constants and x is the downwind distance from the source in meters. The value of a_i and b_i for different downwind distances and various stability classes are given in Table 5.1.

Table 5.1 – The coefficients from PG stability curve

Stability			$x < 0.1km$		$0.1km \leq x < 1km$		$x > 1km$	
	a_y	b_y	a_z	b_z	a_z	b_z	a_z	b_z
A	0.3658	0.9031	0.192	0.936	0.00066	1.941	0.00024	2.094
B	0.2751	0.9031	0.156	0.922	0.038	1.149	0.055	1.098
C	0.2089	0.9031	0.116	0.905	0.113	0.911	0.113	0.911
D	0.1471	0.9031	0.079	0.881	0.222	0.725	1.26	0.516
E	0.1046	0.9031	0.063	0.871	0.211	0.678	6.73	0.305
F	0.722	0.9031	0.053	0.814	0.086	0.74	18.05	0.180

In all the calculations, the dispersion parameters from the PG curve is corrected to the sampling time 60 min using the relation by Brun et. al. [206]. It is known that the extent of dispersion is proportional to the sampling time of the pollutant concentration. If T_a is the averaging time for the concentration/dose in minutes and T_s is the sampling period of the PG dispersion experiment, dispersion has to be enhanced by a factor of $\left(\frac{T_a}{T_s}\right)^{0.5}$ for $15min < T_a < 60min$ and $\left(\frac{T_a}{T_s}\right)^{0.4}$ for $60min < T_a < 240min$. Here T_s is 3 min, the sampling time in the PG dispersion experiments. The ratio is used to multiply the horizontal plume standard deviation computed using PG stability parameters. The study further investigates the effect of correction suggested in USNRC (https://www.nrc.gov/docs/ML1204/ML12045A197.pdf) for low wind speed. As per the United States Nuclear Regulatory Commission (USNRC) safety guide, the crosswind plume standard deviation under meandering conditions (note that the meandering predominant under low wind speed conditions) is given by $\sigma_{y800m} = M\sigma_{PG}$ for a distance up to 800 m. Since data used in USNRC is up to 800 m, it is suggested that the meandering correction should only be applied up to a downwind distance of 800 m and beyond 800 m, no correction is needed. Hence the total plume standard deviation beyond 800 m is given by

$$\sigma_y = (M-1)\sigma_{y800m} + \sigma_{PG}$$

Here σ_y is the horizontal plume standard deviation, including meandering effect, M is the meandering factor and σ_{PG} is the horizontal plume standard deviation estimated using PG stability parameters. For the validation of the LPDM in simulating the plume gamma dose rate, the plume gamma dose computed by the usual triple integration of the standard Gaussian plume model for ground and elevated release (in this case, 100 m) is used. The time step is kept as low as 1 s. The figures (Fig. 5.1a and Fig. 5.1b) show the comparison plot of the simulated plume gamma dose rate by LPDM and plume gamma dose simulated by triple integration of the Gaussian plume equation for unit wind speed and stability category "A" and "F" for ground and elevated release respectively.

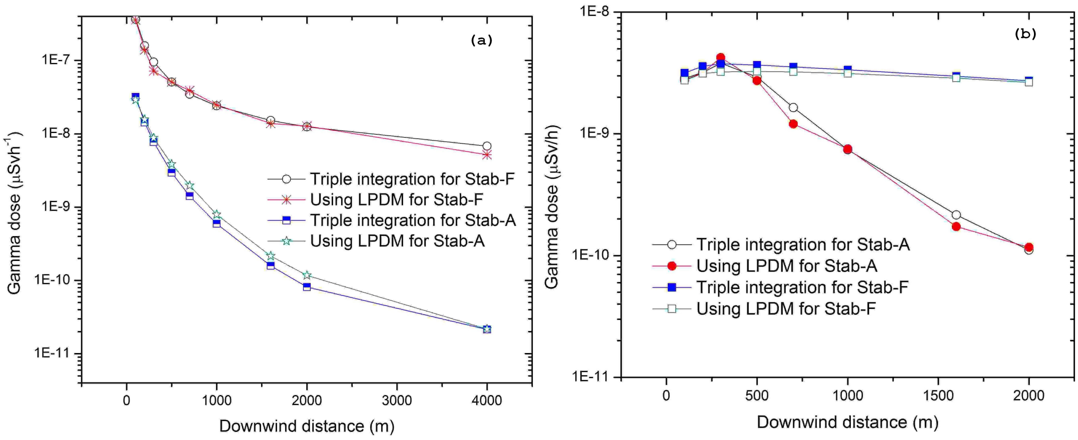

Figure 5.1 – Comparison of simulated dose by triple integration method and LPDM for stability class "A" and "F" for (a) ground release (b) elevated release from 100m

The plume gamma dose rate computation uses the point kernel method [79]. Fig. 5.1

indicates that the simulated gamma dose rate for ground and stack releases using LPDM is in good agreement with the gamma dose rate, simulated using the triple integration method. Further studies discussed in this Chapter use the LPDM with the configuration mentioned above. In all subsequent simulations, the release rate is 1 Bq/s and the release height is zero. The gamma energy of the radionuclide is assumed 1 MeV. The model uses 5 million pseudo particles for dispersion calculations.

5.3 Dispersion simulation under calm wind: Data and methods

At Kalpakkam, calm conditions persist during the stable night and early morning hours (Pasquill stability classes E and F conditions). The wind rose for the year 2018 (Fig. 5.2) shows that the calm periods persist $\approx 8\%$ of the time in the year. As already mentioned in the introduction, the study described in this Chapter considers a wind speed of less than 1 m/s as a calm condition. A sonic anemometer (R.M. Young Ltd) is installed at 10 m above ground level. The data sampling rate of the sonic anemometer is 10 Hz. Sonic anemometer data for the current study is collected such that calm conditions persist for more than one hour. The sonic anemometer data averaging time is 1 min for the computation of the standard deviation of the wind velocity components. The sampling rate of the sonic anemometer is 10 Hz; thus, there is a sufficient number of data points in the averaging window. The Langevin equation (Eqn. 2.4, refer Chapter 2) uses standard deviations computed from sonic anemometer or the HSS method. HSS method uses the scaling parameters such as u_*, L for the computation of wind velocity standard deviation and Lagrangian time scale. These parameters are computed from multi-level tower measurements of wind speed and temperature following flux-profile relationships. For short averaging times, there are flux sampling problems under stable conditions [61]. This problem is circumvented by computing the similarity parameters u_* and L using multi-level meteorological tower data averaged for 30 min intervals using the profile method [193].

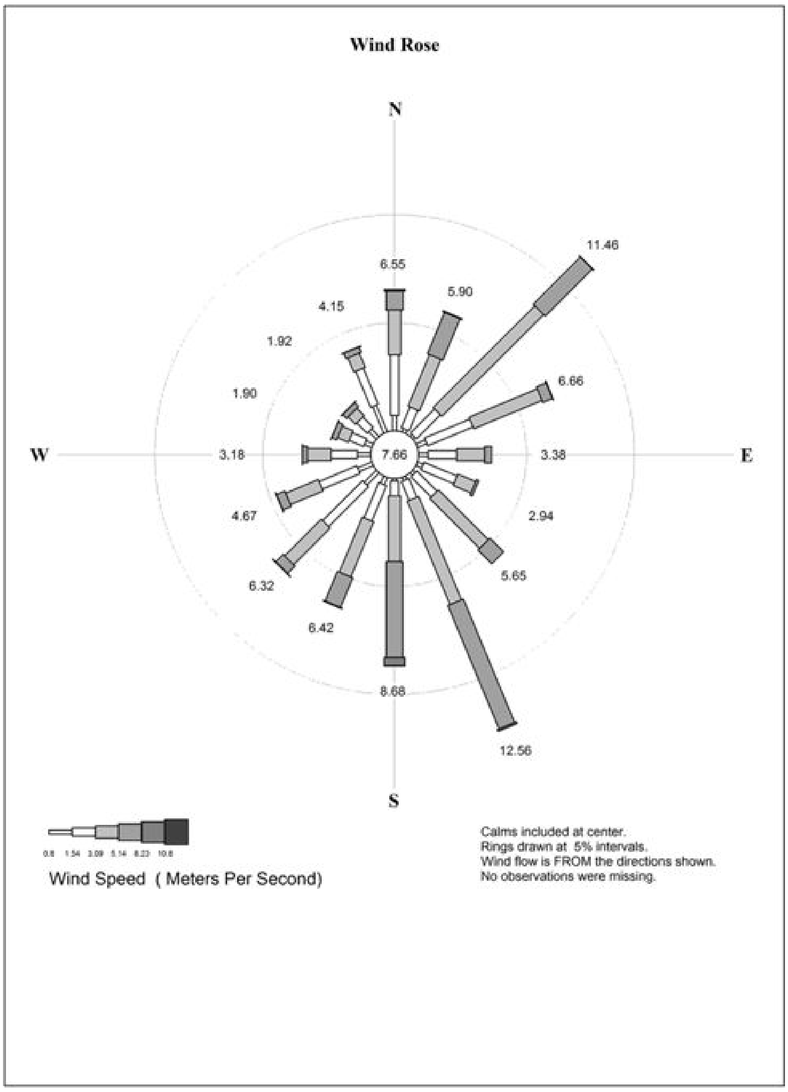

Figure 5.2 – Windrose for the year 2013

While using the DDS method, the Lagrangian time scale is calculated by feeding the wind velocity standard deviation computed using sonic anemometer data in to Eqn. 5.13-5.15. The next section discusses the simulated plume gamma dose using various methods for estimating diffusivity. As already mentioned, calm episodes persist in Kalpakkam during stable atmospheric conditions and therefore, the current study uses parameters and variables for stable conditions, especially in the case of similarity method. An average value of 300 m is taken for the boundary layer height h in Eqn. 5.11-5.15 based on Singh et al. [195]. A few cases of calm episodes during November 2013 are collected under fair weather and stable atmospheric conditions. The results of the dose simulation are discussed below.

5.4 Results and discussion

5.4.1 Case-I

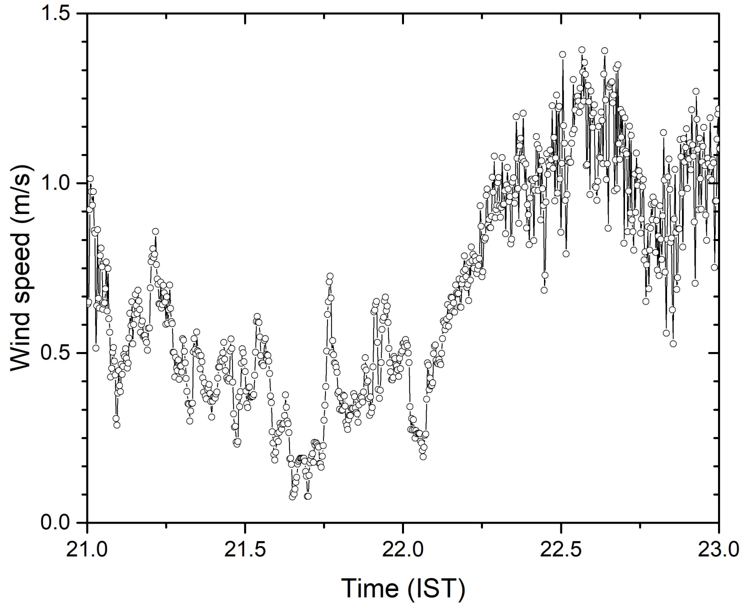

Figure 5.3 – The wind speed at 10 m AGL on 21st November 2013 for two hours starting from 2100 IST

This case refers to a calm episode on 21st November 2013. During the nighttime, calm conditions persisted for two hours after 2100 IST local time. The estimated Pasquill stability condition was “E” during these hours. Fig. 5.3 shows the variation in wind speed for two hours period considered in this study. The average wind speed during the first hour was 0.45 m/s. Fig. 5.4 shows the dose pattern for the first 3600 s using the DDS method. Analysis of results indicates that the dose of 7.12E-8 μSv is present at a distance of 50 m and 1.59E-8 μSv at 500 m away from the release point respectively. A reduction of a factor of five is noticed within a downwind distance of 400 m because during the first hour the average wind speed is as low as 0.5 m/s as already mentioned and therefore, the activity is not transported to larger distances. A Similar calculation using HSS method (not shown) shows a value of 4.42E-8 μSv at 50 m and 7.69E-9 μSv at 500 m,which is approximately a factor of two less than the DDS simulation. The subsequent simulation using the coefficients given in Table 5.1 based on the PG method (not shown) shows a value of 6.92E-8 μSv at 50 m away from the release point and 1.37E-8 μSv at 500 m. Thus the results with the

PG method are in good agreement with the plume gamma dose simulated using the DDS method. It is also to be noted that the activity is concentrated near the release point due to calm wind speed observed during this period.

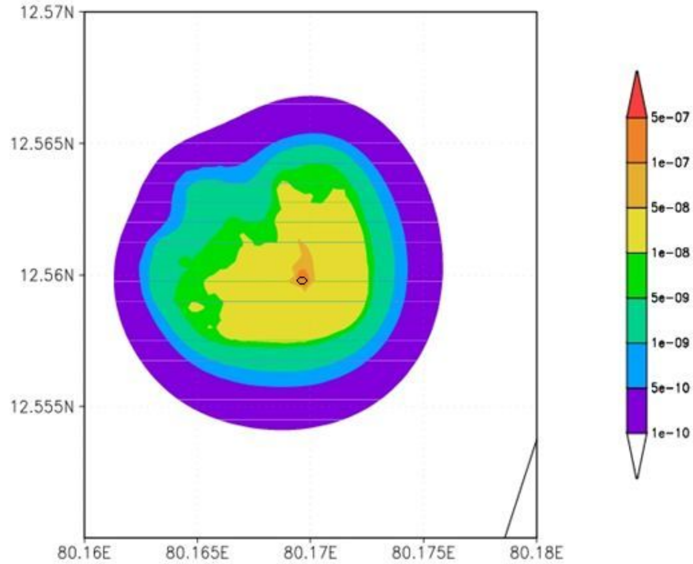

Figure 5.4 – Cumulative Gamma dose for the 1st hour using DDS method. The black circle indicates the release point.

As the simulation progresses, during the second hour, the average wind speed observed was 0.86 m/s, which slightly more than the first hour. The estimated stability condition during the second hour is Pasquill stability condition, "E". During this period the DDS method shows a cumulative dose value (at the end of second hour) of 8.04E-8 μSv, 2.43E-8 μSv and 1.42E-8 μSv at 50 m, 500 m, and 1.5 km respectively from the release point (Fig. 5.5). Similarly, the simulation using the HSS method (not shown) shows a value of 5.48E-8 μSv, 1.53E-8 μSv and 9.83E-9 μSv at 50 m, 500 m, and 1.5 km, respectively from the release point. The simulation shows that the dose computed by the HSS method is approximately 1.5 times smaller than the DDS method. The simulation using the PG method (not shown) and coefficients in Table 5.1 shows a value of 7.85E-8 μSv, 2.18E-8 μSv and 5.88E-9 μSv at 50 m, 500 m, and 1.5 km respectively from the release point. This case shows that dose estimates using the PG method is better than the HSS method, especially within 500 m. At 1.5 km, the dose estimated based on the PG method is less by a factor of 2.5 than the HSS method.

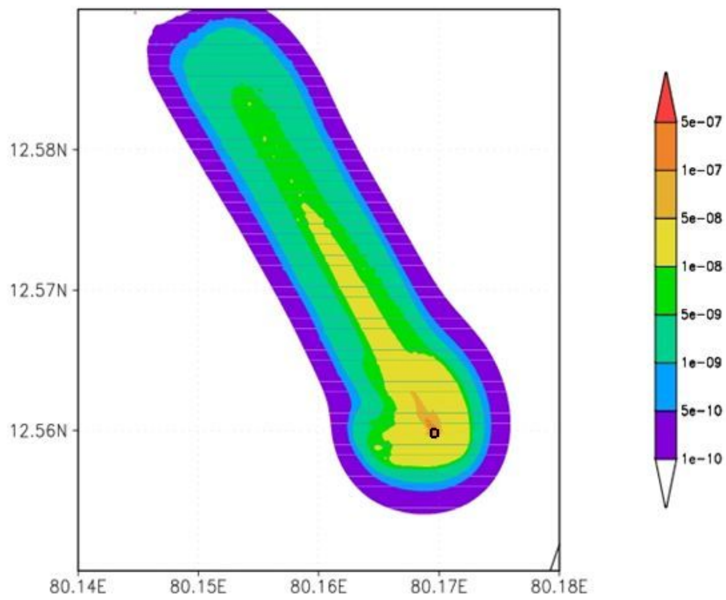

Figure 5.5 – Cumulative Gamma dose at the end of 2^{nd} hour using DDS method. The black circle indicates the release point.

For a better understanding, the factor variation of gamma dose at the end of 2^{nd} hour using the PG method and the HSS method relative to the DDS method is investigated. Fig. 5.6 shows the spatial plot of the factor variation.

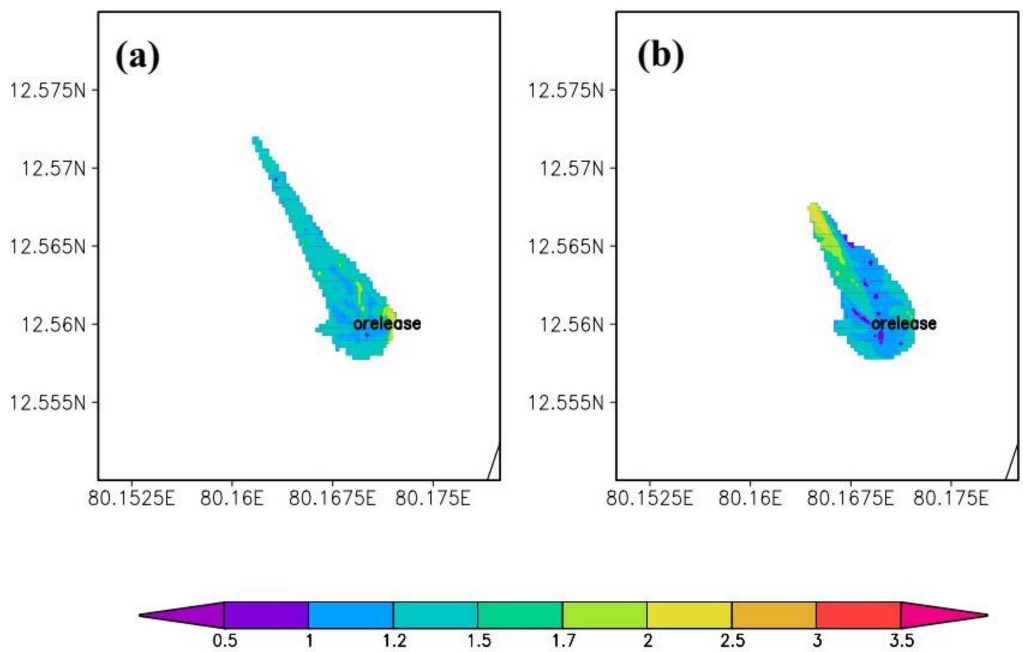

Figure 5.6 – The factor variation in plume gamma dose with PG and HSS method relative to DDS method (a) $Dose_{DDS/HSS}$ (b) $Dose_{DDS/PG}$

The figure indicates that the difference in dose is more with the PG method compared to the HSS method, especially at far downwind distances, though locations near to the release points show promising results with the PG based method. In the case of the HSS method, the difference is more near the release point, and it reduces at points away from the release point to a factor of 1.5. On the other hand, the dose computed based on PG coefficients shows an overestimate by a factor of 2 to 2.5, especially at 1 km downwind.

5.4.2 Case-II

In this case, average wind speed less than 1 m/s persisted for two hours on 20th November 2013 (Fig. 5.7).

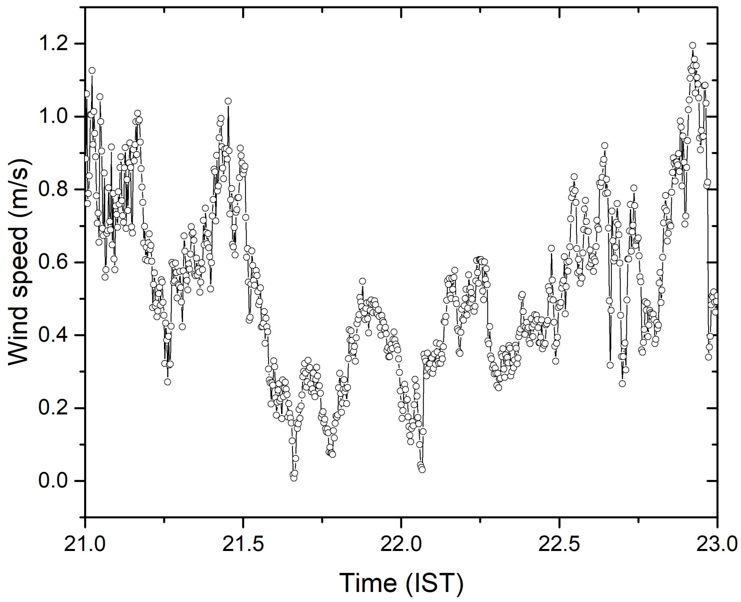

Figure 5.7 – The wind speed at 10 m AGL on 20th November 2013 for two hours starting from 2100 IST

Similar to Case-I, Pasquill stability condition “E” persisted during these hours. The average wind speed for the first hour was 0.53 m/s. Fig. 5.8 shows the plume gamma dose pattern during the first hours of the release. As in the case of earlier simulation unit release rate is assumed. The analysis shows dose contours with values of the order of 3.95E-7 μSv at 50 m near the release point and 1.51E-8 μSv at 500 m away from the release point. On the other hand, the HSS method shows a dose of 3.37E-7 μSv at 50 m from the release point and 1.81E-8 μSv at 500 m from the release point. In this case, the dose estimated using the HSS method (not shown) is in good agreement with the gamma dose simulated using the DDS method. Similarly, the simulation with the PG method (not shown) shows a dose rate of 2.92E-7 μSv at 50 m away from the release point and 1.49E-8 μSv at 500 m, respectively, away from the release point. Fig. 5.9 shows the dose pattern corresponding to the second hour.

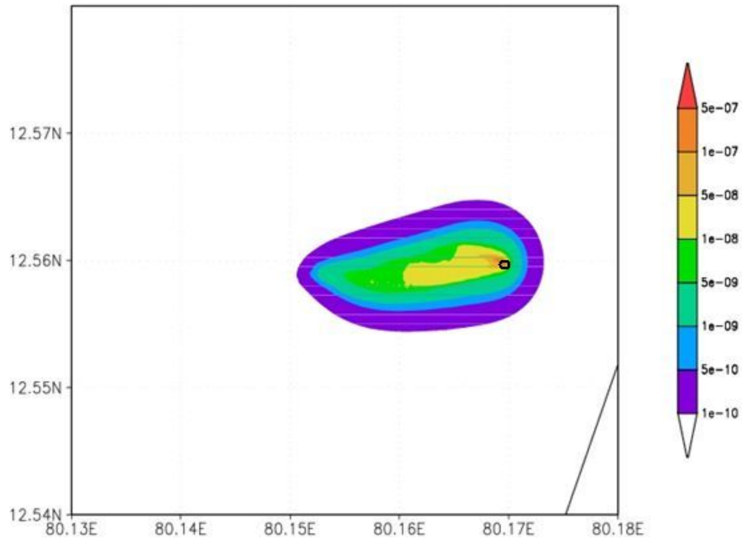

Figure 5.8 – Cumulative Gamma dose at the end of 1st hour with DDS method. The black circle indicates the release point.

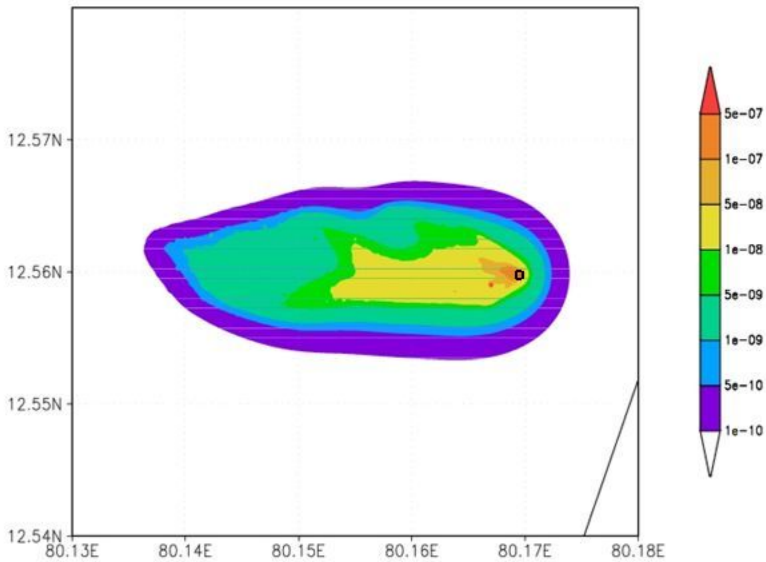

,

Figure 5.9 – Cumulative Gamma dose at the end of 2nd hour using DDS method. The black circle indicates the release point.

During the second hour, the average wind speed was 0.52 m/s and the stability condition remained "E". The first simulation uses the DDS method as a turbulence option. The figure shows the dose contours with values of 6.98E-7 μSv at 50 m away from the release point and 2.88E-8 µSv, 1.53E-8 µSv, respectively at 500 m, 1.5 km away from the release point. On the other hand, the HSS method (not shown) shows a value of 5.64E-7 µSv at 50 m away from the release point and 3.68E-8 µSv, 1.83E-8 µSv respectively at 500 m, 1.5 km away from the release point. It is to be noted that the dose simulated by the HSS method differs by a factor 1.5 compared to the DDS method, especially at 50 m from the release point. Similarly, the PG method (not shown) shows a dose of 2.92E-7 µSv at 50 m away from the release point and 2.88E-8 µSv, 1.11E-8 µSv respectively at 500 m, 1.5 km away from the release point. In this case, the PG method simulated gamma dose by a factor of ≈ 2 less than the DDS method at 50 m away from the release point. The factor variation in dose with various methods relative to the DDS method is shown in Fig. 5.10a and Fig. 5.10b respectively.

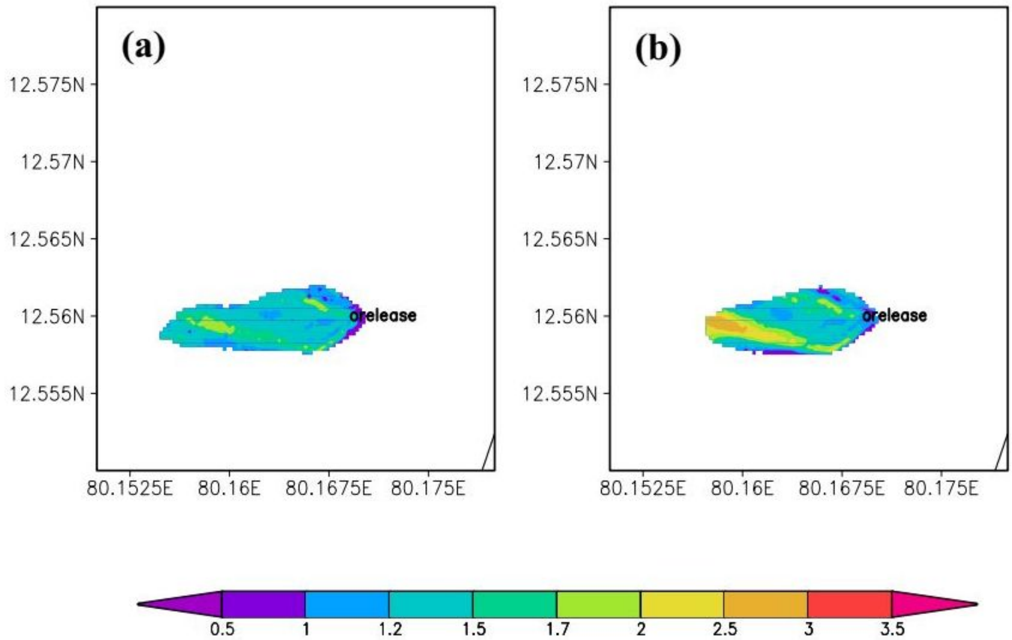

Figure 5.10 – The factor variation in simulated plume gamma dose with PG and HSS method relative to DDS method (a) $\text{Dose}_{\text{DDS/HSS}}$ (b) $\text{Dose}_{\text{DDS/PG}}$

Fig. 5.10a reveals that the difference in gamma dose using the HSS method is maximum up to 1 km, by a factor within 1.7 to 2 relative to the DDS method, and in the case of the PG method, the factor is between 2 to 3 relative to the DDS method. The above results show that the cumulative plume gamma dose simulated using the PG method and HSS method is less than the estimates by the DDS method, but the latter performed better relative to the PG method. Therefore, for the estimation of plume gamma dose under calm conditions, the LPDM with the PG method is less conservative than other methods such as the DDS method or the HSS method. The figure also indicates that the difference in dose is more with PG based method than with the HSS method, especially away from the release point. Further, Fig. 5.11a and Fig. 5.11b show the ground level centerline dose for Case-I and Case-II respectively.

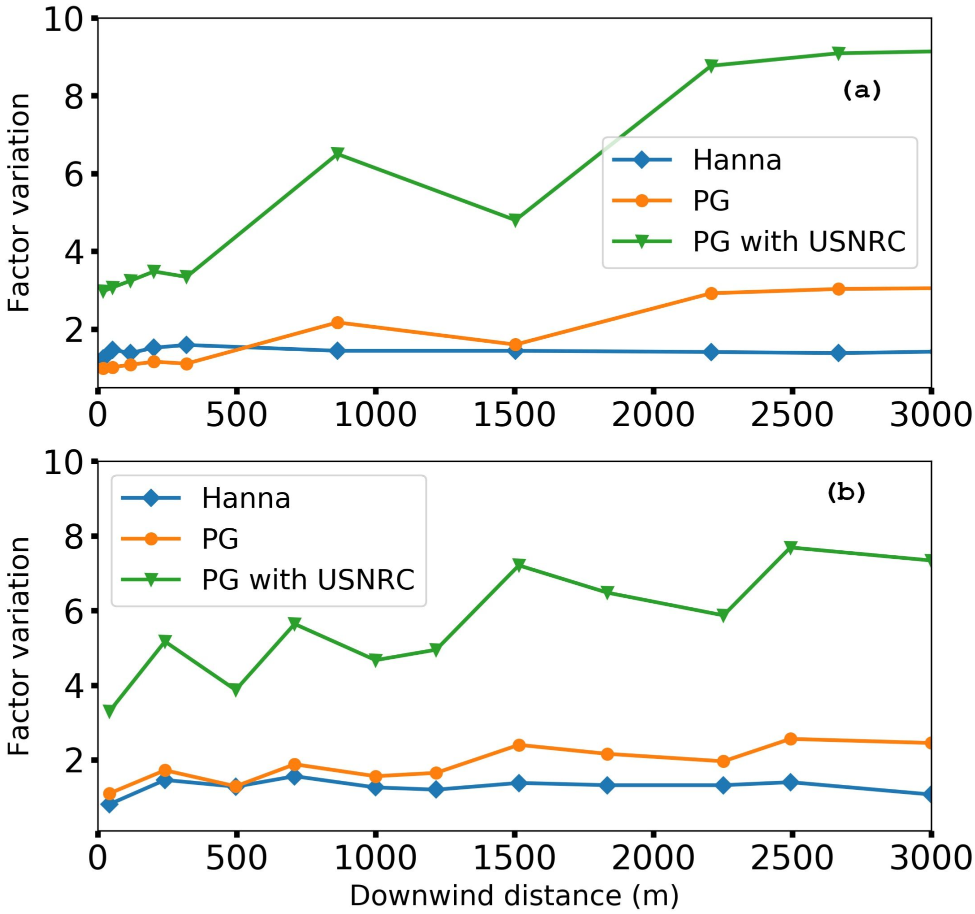

Figure 5.11 – The factor variation in simulated plume gamma dose relative to DDS method for a) Case-I and b) Case-II with various methods

The plot also shows the centerline plume gamma dose simulated using the method suggested by the USNRC. For the simulation with USNRC method, the meandering factors corresponding to the stability class "E," is used as it was the estimated stability condition for Case-I and Case-II. It is noticed from the figure (Fig. 5.11) that the dose estimated using correction suggested by the USNRC is lower by a factor of 4-8 compared to the DDS method. It implies that the PG dispersion parameters or the modified parameters suggested by the USNRC are not suitable for plume gamma dose estimate under calm conditions.

The results indicate that the LPDM or GPM that is generally used by the regulators with PG dispersion parameters cannot be used for plume gamma dose estimates under calm or under very low wind speed.

5.4.3 Case-III

To support the above conclusion, two more cases of calm wind speed conditions are taken. The case was observed on 1st and 5th November 2013. Both the days the average wind speed was below 1 m/s and the stability category was Pasquill condition, "E". The difference plot of simulated plume gamma dose during these days is shown in subsequent figures (Fig. 5.12).

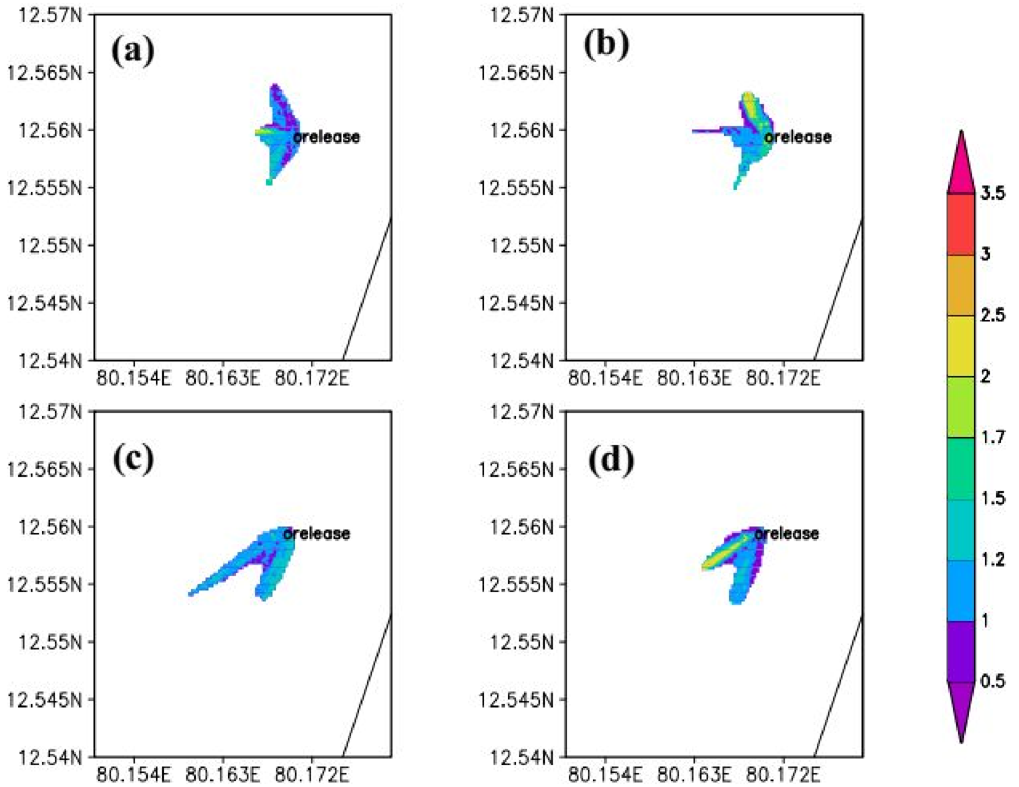

Figure 5.12 – The factor variation in simulated plume gamma dose (a) $Dose_{DDS/HSS}$ (b) $Dose_{DDS/PG}$ for 1st and (c) $Dose_{DDS/HSS}$ (d) $Dose_{DDS/PG}$ 5th of November 2013 respectively.

It is noticed in these cases that the meandering is predominant, and therefore, it is difficult to judge the centerline of the plume. Further, the results indicate that the difference is maximum for the PG method relative to the DDS method. On the other hand, the difference with the HSS method is less than that of the previous cases (Case-I and Case-II). It implies that the diffusion coefficients derived using the PG method is more than that is observed under calm wind conditions, though the atmospheric stability is within the Pasquill classes. Before making any conclusive statements regarding the performance of different schemes under calm conditions, it is required to confirm whether this difference is special to calm conditions alone. Therefore a dispersion case study is performed with days with moderate wind speed (wind speed greater than 3 m/s and the stability being 'E") by employing above diffusion schemes. Fig. 5.13 shows the difference plot of cloud gamma dose simulated using the PG method relative to the DDS method.

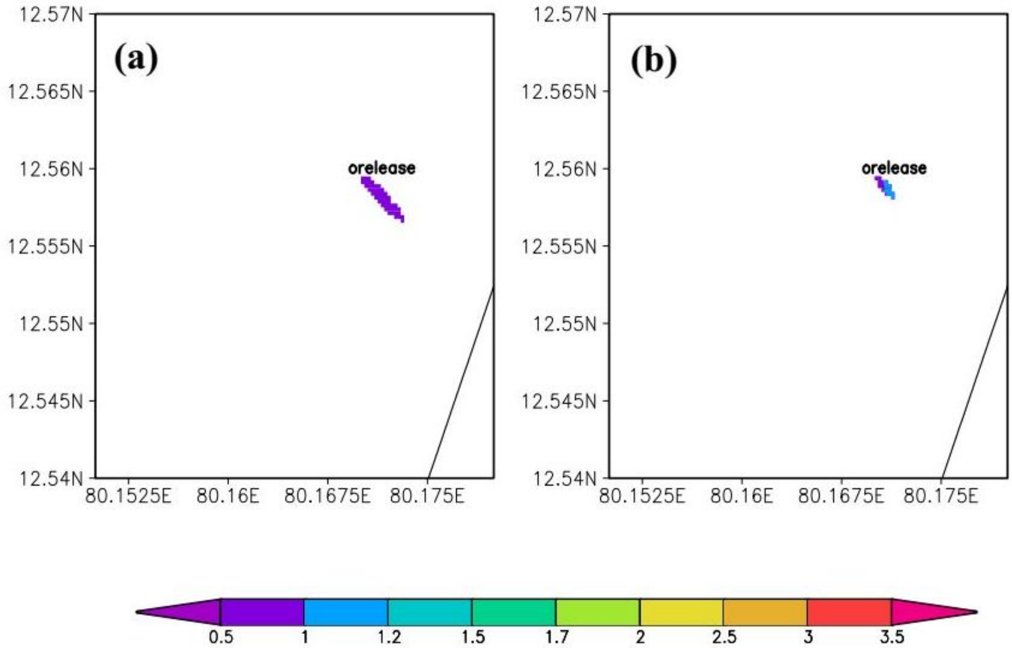

Figure 5.13 – The factor variation in simulated plume gamma dose (a) $Dose_{DDS}/Dose_{PG}$, (b) $Dose_{DDS}/Dose_{HSS}$method under moderate wind speed. The black circle indicates the release point.

The figure shows that the maximum difference is of the factor of 0.8 to 1.1. Further, the difference in centerline dose estimates by the PG based method and HSS method relative to the DDS method is shown in Fig. 5.14. It is noticed that the simulation of dispersion using the HSS method shows a higher dose compared to the DDS method. The difference in dose values is on an average factor of 0.7 and the difference of the PG method relative to the DDS method is on an average factor of 1.3. It is noted that under moderate wind speed, the difference in dose values among the methods under consideration is lesser than their difference noticed under calm episodes. Further, from the above simulation, it is noted that the dose value simulated using the DDS and the HSS method is in good agreement compared to the method using the PG method. Therefore, the PG method based calculations are not suitable under calm wind conditions though they produce better estimates under moderate wind speeds.

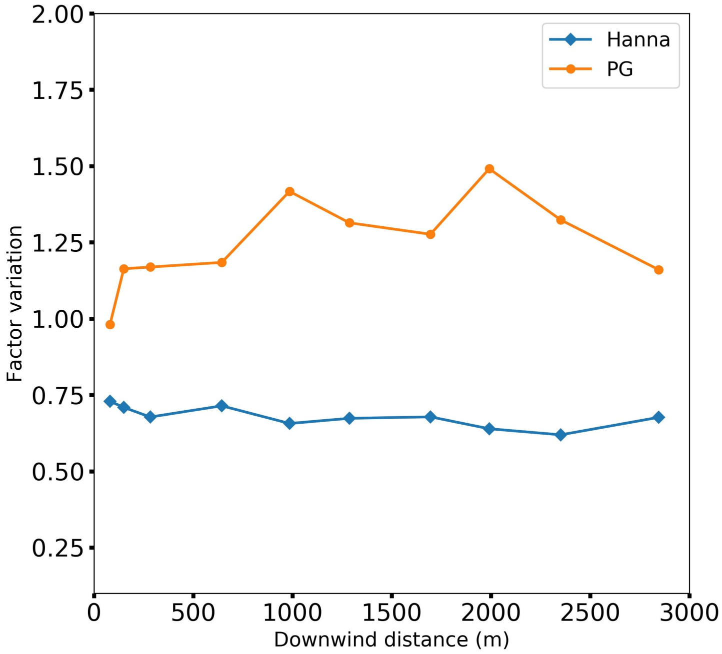

Figure 5.14 – The factor variation in simulated plume gamma with HSS and PG method relative to DDS method under moderate wind speed

5.5 Conclusion

The results of the study indicate that the dispersion of activity/pollutants under calm wind speeds is irregular. It is inferred that the viz-a-viz HSS method and the DDS method show higher plume gamma dose values than the method based on the PG method. Further, it is noticed that the method based on PG dispersion parameters is not conservative compared to the HSS method and DDS method under calm episodes. Therefore for regulatory calculations, under calm wind conditions method based on PG method cannot be used for cumulative dose computation, and methods like HSS method or the DDS method for the computation of turbulence velocity is recommended for conservative estimates.

Chapter 6

Conclusion and future studies

This Chapter lists the excerpts from the work that constitute the thesis. The future work required in gap areas is also outlined.

6.1 Summary and conclusions

The study constitutes this thesis addresses various phenomena affecting the dispersion of radioactive pollutants that can lead to severe radiological impact. The phenomena include submesoscale motions like HCRs, low wind speed meandering, calm episodes, and dispersion under stable conditions. The submesoscale motions such as HCRs are frequently observed over coastal areas like Kalpakkam during the sea breeze hours as well as non-sea breeze conditions, as mentioned in Chapter 2. These structures are observed during sea breeze days using Doppler SODAR and found that submesoscale motions with period 20-30 min are observed during sea breeze hours with varying intensity. The wave periods of these motions are quantitatively studied using FFT and wavelet techniques. Subsequently, these structures are simulated using WRF model in high spatial resolution and simulated dispersion of activity using the FLEXPART particle dispersion model. It is found that the presence of such motions increases the severity of the radiological impact as there will be higher dose at divergent zones that are occupied by downdrafts. The Chapter 2 concludes that high-resolution numerical simulation is essential for realistically predict the existence of such motions. This study, therefore, warrants high-resolution simulation using weather models to predict the radiological impact realistically.

Further, in Chapter 3, the dispersion under stable atmospheric conditions is investigated. The study shows that the dispersion under stable atmospheric conditions is crucial to determine the radiological impact realistically. The thesis investigated the dispersion coefficients under stable atmospheric conditions and proposed empirical relations that need to be used in dispersion models to use under stable conditions. The study used data from ultrasonic anemometer collected during the stable atmospheric condition over two topographically different sites, viz-a-viz, a coastal area at Kalpakkam, and complex hilly terrain in southern France, Cadarache. Further, these formulations are incorporated in the FLEXPART model, and the results show that the modified method shows higher dose/concentration than the conventional similarity method by Hanna. Moreover, the study shows that the modified method simulated the observed dose using AGDL better than the conventional method. It is generally known that dispersion under stable conditions increases the severity of the impact. However, the study shows that the conventional methods such as Hanna's scheme formulated under stable conditions also underestimate the dose under these conditions. Therefore, it is required to have site-specific relations for stable atmospheric conditions by properly filtering the submesoscale motions from the data.

The thesis further explored the dispersion under low wind speed as well as calm atmospheric conditions using in house developed Particle dispersion model. Observation shows that under low wind speed plume will meander over sectors, and concentration will be lower because of the enhanced diffusion. However, it is to be noted that large-angle meandering will affect nearby sectors, that one may miss if the low wind speed meandering is not considered. Though the centerline dose may reduce, the impact on the adjacent sectors depends upon the source term during the accident. Modified Lagrangian and Gaussian models are used to account for meandering, and simulated results are compared against data tracer dispersion data from the Hanford-67 tracer experiment. Further, studies are carried out under calm/low wind speed conditions. Results show that under calm episodes, there will be an accumulation of activity near the release point that leads to high dose/concentration near the release locations. It is also noted that the method based on the PG stability curve underestimates the dose due to the increased dispersion factor. Hence, the thesis addressed these phenomena affecting dispersion, leading to severe radiological impact. Though the thesis addressed the effect of HCRs during sea breeze hours, dispersion under stable conditions, low and calm wind conditions, it opens up areas for future research, which is outlined below.

6.2 Scope for future studies

- One of the crucial studies required is the sensitivity of HCRs to different PBL schemes in WRF. It is needed mainly because the different PBL schemes simulate different values for diffusivity coefficients, and this, in turn, can affect the shear and buoyancy fluxes of the scalar and momentum. Further, effect of HCRs on puff release and continous releases from ground as well as from stack need to be studied to get a complete picture of dispersion. Moroever, the effect HCRs may be completly different for point, area and line sources.

- The thesis concludes that the dispersion under stable conditions could be simulated with the dispersion model with the modified dispersion parameter in conjunction with high-resolution WRF or similar weather models to simulate the submesoscale motions. However, these diffusivity relationships need to be validated extensively by conducting tracer release experiments under highly stable conditions of the atmosphere for statistically robust conclusions. There are many motions like gravity waves, and drainage flows that fall under submesoscale motions. A few studies in the past show the successful simulation of these phenomena using WRF by introducing low diffusivity in the WRF model or by reducing the background turbulence kinetic energy set in the model. Therefore, one of the challenging problems is to have parametrization in weather models such as WRF so that these motions could be successfully simulated.

- Similarly, the thesis addressed the theoretical part of the dispersion under calm episodes. Further, extensive experiments need to be conducted under calm events and calm followed by gusting winds for validation and to establish new formulation for dispersion under these conditions. Moreover, weather model like WRF needs to be configured to simulate similar conditions and provide inputs to dispersion models.

List of Abbreviations

ABL Atmospheric Boundary Layer

AERMOD American Meteorological Society/Environmental Protection Agency Regulatory Model

AEROPOL The AERO-POLlution model

AGDL Autonomous Gamma Dose Loggers

AGL Above Ground Level

ALOHA Areal Locations of Hazardous Atmospheres

BLP Buoyant Line and Point source

CALINE3 California Department of Transportation

CALPUFF CALifornia PUFF

CPB Canyon Plume Box

CV Cadarache Valley

DDS Diffusion Derived from Sonic anemometer

DF Dilution Factors

DV Durance Valley

EAF Eulerian Auto-correlation Function

FAC2 Factor of two

FB Fractional Bias

FBR Fast Breeder Reactor

GFS Global Forecast System

GMT Greewich Mean Time

GPM Gaussian Plume Model

HCRs Horizontal Convective Rolls

HSS Hanna Similarity Scheme

HYSPLIT Hybrid Single Particle Lagrangian Integrated Trajectory

IGCAR Indira Gandhi Center for Atomic Research

IOP Intensive Obervation Period

ISC Industrial Source Complex

IST Indian Standard Time

KASCADE KAtabatic winds and Stability over Cadarache for the Dispersion of Effluents

LPDM Lagrangian Particle Dispersion Model

LWS Low Wind Speed

MAPS Madras Atomic Power Station

MG Geometric Mean

MODIS Moderate Resolution Imaging Spectroradiometer

MOST Monin-Obukhov Similarity theory

MRD Multi-Resolution Decomposition

MSL Mean Sea Level

MST Mesosphere-Stratosphere-Troposphere

MYJ Mellor-Yamada-Janjic

NAME Numerical Atmospheric-dispersion Modeling Environment

NCEP National Center for Environmental Prediction

NMSE Normalized Mean Square Error

NWP Numerical Weather Prediction

OCD Offshore and Coastal Dispersion

ONERS Online Nuclear Emergency Response System

PBL Planetary Boundary Layer

PG Pasquill-Gifford

PHWR Pressurized Heavy Water Reactor

RAPTAD Random Puff Transport and Diffusion

RIMPUFF RIsø-Mesoscale-PUFF

RMSE Root Mean Square Error

RODOS Real-time Online Decision Support

RRTM Rapid Radiative Transfer Model

SAMEER Society for Applied Microwave Electronics Engineering & Research

SBL Stable Boundary Layer

SCIPUFF Second-order Closure Integrated PUFF

SODAR Sonic Detection And Ranging

SPEEDI System for Prediction of Environmental Emergency Dose Information

TIBL Thermal Internal Boundary Layer

TKE Turbulence Kinetic Energy

TS Tether Sonde

UK-ADMS UK Atmospheric Dispersion Modelling System

USGS United States Geological Survey

USNRC United States Nuclear Regulatory Commission

VG Geometric Mean Variance

WRF Weather Research Forecast

Annexure-1

Table 6.1 – List of instruments used.

Site	Instruments	Co-ordinates	Elevation (m MSL)	Measu. height (m)	Variable	Acquisition frequency
Kalpakkam	SODAR (SAMEER Make)	12.5838°N, 80.1734°E	6	20-500	U, V, W $\sigma_u, \sigma_v, \sigma_w$	-
	Young 81000 Sonic anemometer	12.5838°N, 80.1734°E	6	10	U, V, W $w'T'$	10 Hz
	NRG 40C cup anemometer NRG 200P Wind vane	12.5639°N, 80.127°E	6	2 , 8 , 16 , 32 , 50	Wind speed, Wind direction	-
	Rotronic Temperature and Humidity sensor	12.5639°N, 80.127°E	6	2 , 16 , 50	T, RH	-
Cadarache	Young 81000 sonic anemomete	43.68550°N 5.76169°E	286	10.5	U, V, W $w'T'$	10 Hz
	Vaisala TTS111 tethersondes	43.68511°N 5.76233°E	287	2-300	RH, P T, Wind direction, Wind speed	0.25 Hz
Hanford	Cup anemometer (Beckman and Whitley V)	46.56667°N, -119.60°W	224	0.8, 1.5, 3.0, 6.1, 12.2, 24.4	Wind speed	Not Known
	Aerowane (Beckman and Whitley V)	46.56667°N, -119.60°W	224	0.8, 1.5, 3.0, 6.1, 12.2, 24.4	Wind direction	Not Known
	Temperature sensor	46.56667°N, -119.60°W	224	0.91, 6.1, 15.2, 30.5, 45.7, 61.0, 76.2, 91.4, 122	T	Not Known